Eindhoven University of Technology

Eindhoven University of Technology

MASTER

Tuning magnetic multilayers for skyrmion nucleation

van Liempt, A.P.

Award date:
2019

Link to publication

Eindhoven University of Technology
Department of Applied Physics
Physics of Nanostructures

Tuning magnetic multilayers for skyrmion nucleation

A.P. van Liempt

Supervisors:
ir. J. Lucassen
prof. dr. ir. H.J.M. Swagten

Eindhoven, February 2019

Abstract

Current hard disk drives are reaching their storage density limit but a new technique called skyrmion racetrack memory (SRM) is a promising candidate for future application in magnetic data storage. SRM uses skyrmions which are whirling spin textures which are stable up to a very small scale and can be used as bit carriers in magnetic data storage. However, the stabilization of skyrmions at room temperature remains problematic which is why this thesis focuses on characterizing the micromagnetic interactions in magnetic multilayers that are able to stabilize skyrmions. Specifically, we characterize the magnetic anisotropy (K) and Dzyaloshinskii-Moriya Interaction (DMI, or D) as a function of Co-thickness and Ga^+-irradiation using a domain spacing model in combination with several magnetization measurement setups and the magnetic force microscope (MFM). However, the MFM required optimization before it was usable which is also part of this thesis.

First, the MFM is optimized by us producing our own tips. The commercially available MFM tips altered the domain structure of the samples so by depositing an ultrathin layer of Co on commercially available AFM tips, we could produce tips ourselves which only probed the domains. Quantitatively verifying that the samples remain unperturbed was not possible but qualitatively it is confirmed that we can produce tips that only probe the magnetic domains.

Secondly, how K and D behave as a function of the Co-thickness, t_{Co}, is characterized. K shows an increasing trend which is attributed to the interfaces in the multilayer, which contribute to K, still being under development. D, another interface interaction, shows a decreasing trend whereas an increase is expected since K also increases in this region. The cause of this is not known but probably results from an interplay between interface development and our samples not meeting the assumptions for the used models.

Lastly, it is investigated how K and D are altered for a certain dose range of Ga^+. Only a small decrease is found and from simulating Ga^+ irradiation of our sample it is found that only the upper part of the multilayer is affected, leaving the effect on the majority of the sample negligible.

Utilizing other domain spacing models which take domain wall interactions less crude into account is expected to result in more reliable results for D. Also, by lowering the amount of layers in our stack, a bigger effect of Ga^+-irradiation on K and D is expected to be observed.

Contents

Chapter 1

Introduction

Magnetism has a rich history in the application of data storage with the floppy disk the first device to reach a broad audience. Being introduced in 1971 by IBM, it followed the magnetic tape drives and finally offered consumers a possibility to handy portable data. It is the 3.5-inch, 1.44 MB floppy disk, pioneered by Sony in the 80's, that would be best remembered since it was introduced at a time the personal computer made it to the masses and its iconic appearance has since then been used to symbolize saving data. The floppy disk eventually lost its popularity in the 90s after the introduction of the CD-ROM which offered higher data storage capacity and better reliability [1].

Today, the most commonly used device for storing data magnetically is the hard disk drive (HDD) of which an example is shown in figure 1.1a. Disks consisting of ferromagnetic material are positioned on top of each other and the read/write-arm can move in between the rotating disks across its full radius.

The way data is stored on an HDD is actually quite similar to that of a floppy disk. A magnetically active disk —which is present in both a floppy and an HDD— can be divided in small areas which contain a magnetization in a certain direction as is shown schematically in figure 1.1b. These magnetic domains either point to the left or the right which can be interpreted as the binary '0' and '1'. The read/write-head can —as the name already suggest— read or write these domains so that data can be stored or accessed on the device. With the growing size of computer applications, a higher data capacity and faster access to data on these disks is necessary. One of the steps to accessing this is by changing the magnetization direction from being parallel to the disk's surface to perpendicular. Current-day HDDs are devices of which the disks have this out-of-plane (OOP) magnetization as is shown in figure 1.1c. The cross section of such a disk can be seen with the magnetization pointing either up or down. The lines seperating the different domains symbolize the domain walls which serve as a transition region between two directions of magnetization. In this picture, they are assumed to be infinitely thin but further on in this thesis will be discussed what determines their width.
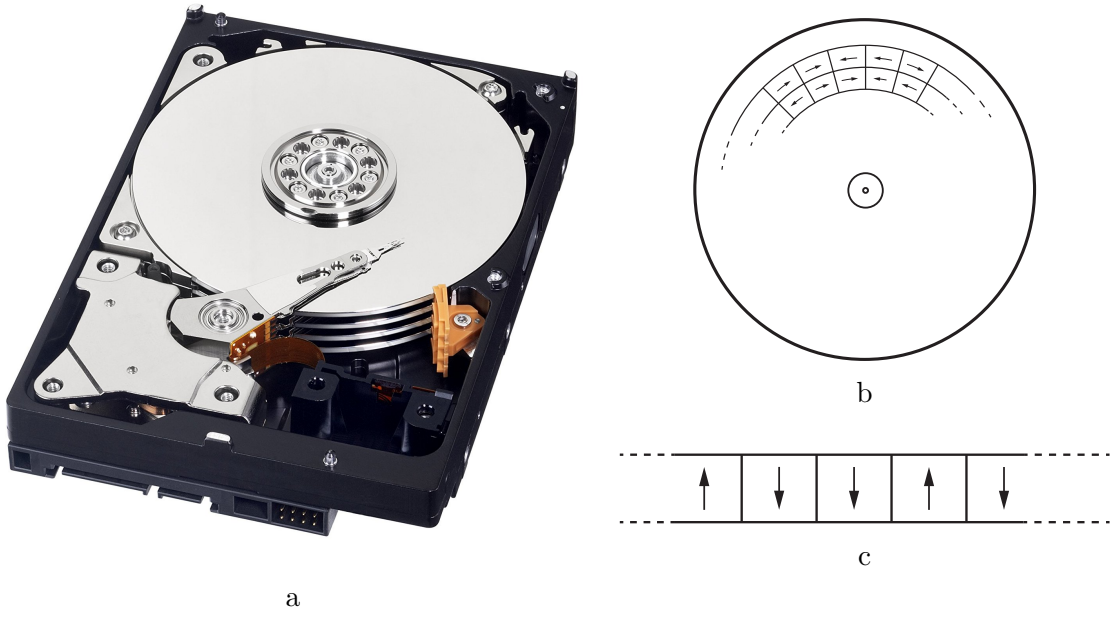
Figure 1.1: a: An HDD seen from inside. Four disks that contain the data are stacked on top of eachother and the read/write-arm hovers over the disks' surfaces. Picture from [2]. b: Schematic top-view of a magnetic disk on which date can be stored. The magnetization of the domains in which the disk is divided either points to the left or right serving as binary '0' or '1'. c: Schematic cross-section of a magnetic disk with the magnetization pointing out of the plane.
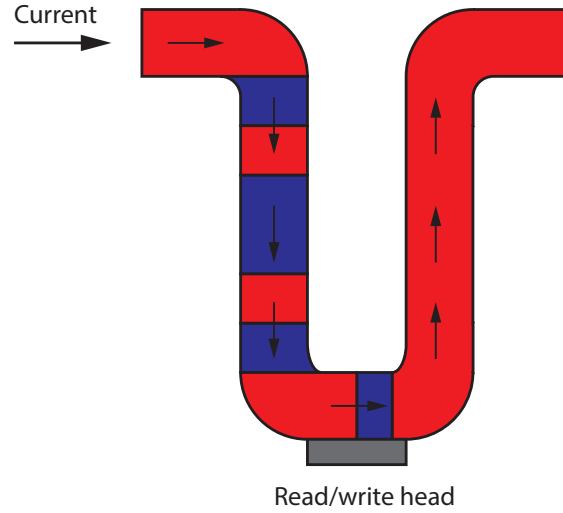
Figure 1.2: Racetrack memory as proposed by Stuart Parkin. The track is bent upwards so it can occupy three dimensions. In the track, domains pointing up (blue) or down (red) are read/written in the read/write head. By sending a current (indicated with the arrows) through the wire, the domain walls (and thus the domains) can be moved through the wire.

Since the demand for higher data capacity and faster operating speed is still growing, the HDD needs to be improved if it wants to remain relevant. Problematic, however, is that domains sizes cannot keep on shrinking. The smaller a domain gets, the more susceptible it is to switching magnetization randomly due to thermal fluctuations [3]. This is unwanted since it would mean data loss for the consumer. Another drawback of the HDD is that rotating the disks and moving the read/write-arm means physical motion which is energetically inefficient. Moving to random-access memory (RAM), which is faster, seems tempting but this technique remains expensive in production and has the drawback that the stored date is volatile: meaning that it's gone as soon as the power is shut off from the device.

A solution to achieving the higher data capacity and faster operating times is proposed by Staurt Parkin in 2008 [4]. The racetrack memory (RM), as he calls it, would combine the best of both worlds: low in production cost, high in data density, fast in operating time and non-volatile storage. RM, as shown in figure 1.2, consists of a magnetically active nanowire in which OOP domains are located. Here, the domains are read and written at an immobile read/write-head located on the bottom of the wire. In contrast to the HDD, the domains move through the medium along the read/write-head during operation. By sending current pulses through the wire, domain walls can be moved along the current. Domain wall velocities of up to $750 \, \text{m} \, \text{s}^{-1}$ have already been reported by Yang et al. [5].

One of the perks of RM is the possibility to construct the wire upwards, so that the wire occupies three dimensions instead of the regular two dimensions by, for example, the HDD. This would then greatly increase the storage density of the data storage device.

1.1 Skyrmions

A way of further increasing the storage capacity is by replacing the domains with magnetic skyrmions. These are magnetic spin textures that can be stable up to very small scale [6]. An example of two types of skyrmions can be seen in figure 1.3 where both a Bloch type (left) as Néel type (right) skyrmion are shown with their accompanying cross-sections below. In both images, the magnetization is pointing upwards outside of the skyrmion and downwards in the middle. The way the spins rotate from up to down, as seen in the cross-sections, is what determines whether they are Bloch or Néel type: for Bloch type, the magnetization rotates perpendicular to the skyrmion radius whereas in the Néel type, it rotates along the radial direction. The defining property of the skyrmion is that it has a spherical topology which can be envisioned as having a defect free transition from up to down magnetization [7].
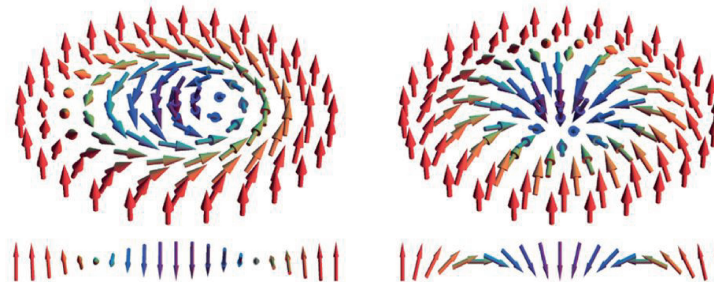
Figure 1.3: Spin structure of a Bloch type skyrmion (left) and Néel type skyrmion (right). Figure from [8].

The spherical topology is what makes skyrmions stable up to very small radii (sub-100 nm skyrmions have been reported by Legrand et al. in [9]), and moving them with velocities up to $100\,\mathrm{m\,s^{-1}}$ has been reported by Woo et al. in [10]. Also, a low driving current (compared to domain walls) that is necessary to move the skyrmions is reported by Song et al. in [11]. These properties make skyrmions an interesting candidate for application in RM.

Skyrmions have been stabilized by, for example, [12] and [13] but these were only stable at low temperatures in thin films grown by molecular beam epitaxy, which makes it unattractive for application in industry. Stabilizing skyrmions in thin magnetic films at room temperature would be commercially more interesting but this remains challenging. Jiang et al. show that 'blowing' skyrmion bubbles by sending an inhomogeneous spin-current through a geometrical constriction is a possibility [14] whereas Buettner et al. suggest

sending an inhomogeneous spin-current along a site with lowered anisotropy [7]. However, with these methods it is hard to control the size or amount of skyrmions that form, leaving the magnetic thin films unusable by industry.

To stabilize skyrmions in magnetic multilayers, it is believed that the Dzyaloshinskii-Moriya interaction (DMI) is essential [15] which lead to Balk et al. [16] investigating whether it is possible to tune the DMI with Ar^+ irradiation. They found that it is possible to alter the DMI in a Pt/Co/Pt system whereas other parameters (the magnetic anisotropy of the system) remained stable. Part of this thesis focuses on the effect of Ga^+-irradiation on the DMI in magnetic systems with multiple thin magnetic layers since this remains uninvestigated.

1.2 This thesis

It remains challenging to investigate the link between skyrmions and the DMI since there is no universal technique to easily measure the DMI. This thesis focuses on determining the DMI in samples with multiple magnetic thin layers and find the conditions under which skyrmions form. This is investigated as a function of the thickness of the magnetic layers but it is also investigated what the influence of Ga^+-irradiation on the DMI is.

In chapter 2, the theoretical background for this thesis will be given. The magnetic interactions that are of importance for the creation of skyrmions will be discussed as well as two models to determine the strength of these interactions from the measurements. Chapter 3 will explain what tools are used for this thesis as well as the theoretical background that is necessary to understand how the data from these tools is related to the parameters that they determine. In chapter 4 is discussed how one of experimental setups is optimized so it can be used throughout this thesis. This is the magnetic force microscope (MFM). Chapter 5 is about relating the system parameters, like DMI and magnetic anisotropy, to the thickness of the magnetic material in the system. Chapter 6 discusses the effect of Ga^+-irradiation on the samples its parameters and chapter 7 will contain the conclusion of the results and also give an outlook on what further research would be interesting to perform after this thesis.

Chapter 2

Theory

As is discussed in the introduction, thin film systems will be tuned in order to realize skyrmion stabilization. One of the key parameters is the DMI but there are other interactions that play an important role. In this chapter it is treated what interactions are present in the investigated magnetic systems and what they depend on. After this, two theoretical models are discussed that are used to determine the interaction strengths from the measurements. In order to understand what complications could arise when applying these models, hysteresis will also be discussed.

2.1   Domain walls and their energy

To understand skyrmion stabilization, it is first important to understand what domain walls are and what determines their properties. Domain walls (DW) have already been mentioned in the introduction as being the transition region of going from one direction of magnetization to the other. This is shown in figure 2.1 where a magnetic material with an 'up' magnetization on the left and a 'down' magnetization on the right can be seen with a DW in between. Two types of domain walls are displayed which are called the Bloch (left) and Néel (right) DW. The difference between the two lies in the way the spins rotate from one orientation to the other. In Bloch DWs, the spins rotate out of the plane whereas in Néel DWs they rotate in the plane. The typical DW size in our systems is $\approx 10\,\mathrm{nm}$.

The two domain wall types can also be identified in skyrmions. In figure 2.2 the two types of skyrmions, Bloch and Néel, are shown with their cross-sections below. Here, we see that these cross-sections contain two Néel/Bloch DWs. In other word, creating a skyrmion inevitably means creating domain walls, making it important to understand what physics underlie these domain walls.

To describe the formation of domain walls, an energy penalty for making a DW is given by [18]

$$\sigma = 4\sqrt{AK} - \pi|D|. \tag{2.1}$$
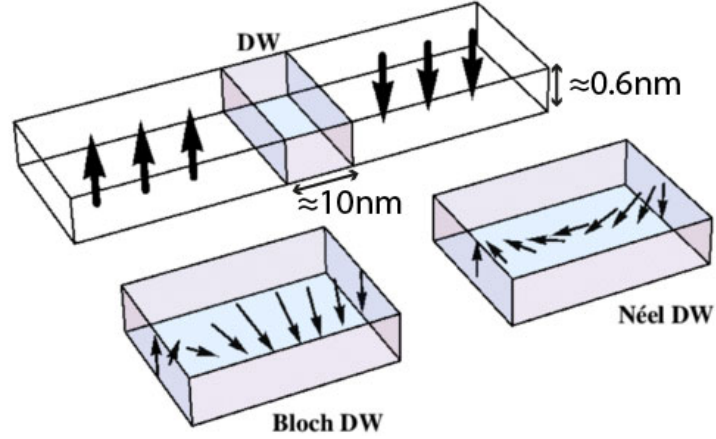
Figure 2.1: An out-of-plane magnetized layer is shown with its magnetization pointing up on the left and down on the right. The domain wall (DW) in between is shown and two types of domain walls are drawn. The way the spins rotate in the DW determines whether they are Bloch (left) or Néel-type (right) domain walls. Figure adapted from [17].
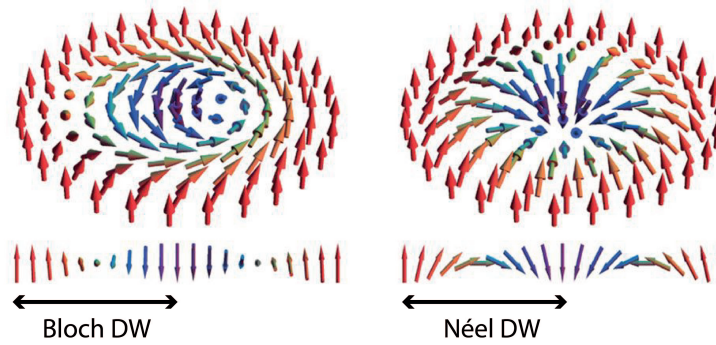
Figure 2.2: A Bloch (left) and Néel (right) skyrmion with their cross-sections shown below. Skyrmions contain DW which are indicated. Figure adapted from [8].

The earlier discussed DMI is present in this energy equation as D but also two other interactions play a role: the exchange interaction A and anisotropy energy K. These three interactions are going to be discussed in this chapter. Equation 2.1 also provides a way of determining the DMI in a magnetic system. In this thesis, E_{DW} and K are measured and A is assumed from literature so D can be calculated. How the parameters are measured will also be discussed in this chapter.

2.1.1 Exchange interaction

The exchange interaction is a quantum mechanical effect resulting from the Heisenberg exchange interaction of which the Hamiltonian is given by [19]

$$\mathcal{H} = -2J\vec{S}_i \cdot \vec{S}_j, \tag{2.2}$$

where J is the exchange constant and $\vec{S}_i$ and $\vec{S}_j$ are two neighboring spins. An extensive treatment of this interaction can be found in [19] but for ferromagnetic materials J is defined as positive meaning that the adjacent spins want to be parallel. Extending this interaction to multiple spins (continuum limit) results in [20]:

$$E_{\mathrm{exc}} = A(\nabla \frac{\vec{M}}{M_{\mathrm{s}}})^2. \tag{2.3}$$

The exchange energy, E_{exc}, increases if there is a gradient in the magnetization, $\vec{M}$. Creating domain walls therefore costs energy because of the intrinsic spin rotation. In 2.1, this shows up as a square root dependence of the DW energy on A.

2.1.2 Anisotropy energy

So far in this thesis, it is assumed that the magnetization can be along two directions: in the plane of the disk as in figure 1.1b or perpendicularly to the disk as in figure 1.1c. A preference of the magnetization to be aligned along a certain direction is called magnetic anisotropy and this preferential direction is also known as the easy axis, perpendicular to the easy-axis lies the hard-axis. What determines whether the easy axis lays in-plane (IP) or out-of-plane (OOP) will be discussed further on in this section.

All the systems under consideration for this thesis have an OOP easy eaxis (or perpendicular magnetic anisotropy, PMA). What this means for the domain wall energy can be understood with the help of the following equation [20]:

$$E_K = K \sin^2 \theta. \tag{2.4}$$

The anisotropy energy E_{K} in magnetic film depends on the anisotropy constant K, which is positive for systems with PMA and negative for an in-plane anisotropy, as well as the angle between the magnetization and the easy axis θ. Pulling the magnetization away from

its anisotropy axis thus costs energy. A higher K will increase the energy that is needed to pull the magnetization away from the easy axis and, because spins inside the domain wall are at an angle with respect to the easy axis, will therefore increase the domain wall energy in equation 2.1.

The anisotropy constant is one of the parameters that will be tuned and has various contributions of which several will be discussed next.

Magnetocrystalline anisotropy The magnetocrystalline anisotropy K_N (named after Néel who developed a model to describe it in [21]) is a result of the spin-orbit coupling (SOC) between electrons and the lattice [22]. For the systems in this thesis, the magneto-crystalline anisotropy mainly contributes due to the interfaces of the magnetic films. A break in symmetry is present at these interfaces altering the orbitals of the electrons at these interfaces. For the systems in this thesis, the interfaces are chosen such that the magnetic moment will align perpendicular to the interface and thus promote PMA [23]. It will therefore increase the K in equations 2.4 and 2.1.

Shape anisotropy The shape anisotropy, K_{shape}, relates the anisotropy axis to the shape of the specimen and lowers K in the case of magnetic thin films. For this thesis it is instructive to use the magnetic charge method [24] to explain the shape anisotropy.

Consider an infinitely long thin film with an OOP magnetization, $\vec{M}$, as pictured in figure 2.3. Magnetic charges can be introduced on the faces of the film according to [20]:

$$\sigma_m = -\vec{M} \cdot \vec{e}_n, \tag{2.5}$$

with σ_m the surface charge density and $\vec{e}_n$ the film surface's normal. The magnetic field inside the film resulting from these charges is antiparallel to the magnetization and called the demagnetizing field $\vec{H}_d$. For thin films with an OOP anisotropy, this demagnetizing field equals [20]

$$\vec{H}_d = -M_z \hat{z}. \tag{2.6}$$

The demagnetization energy resulting from $\vec{H}_d$ interacting with $\vec{M}$, equals [20]:

$$E_{demag} = -\frac{1}{2}\mu_0 \vec{M} \cdot \vec{H}_d = \frac{1}{2}\mu_0 M_z^2. \tag{2.7}$$

Since $\vec{M}$ is always antiparralel to $\vec{H}_d$, E_{demag} will always be positive. However, when the magnetization is in-plane, the surface charges will be too far apart for $\vec{H}_d$ to still be relevant and thus no E_{demag} will be present making PMA energetically unfavorable. The shape anisotropy is therefore, in the case for the thin films used in this thesis, a contribution that will lower K in equation 2.4 as

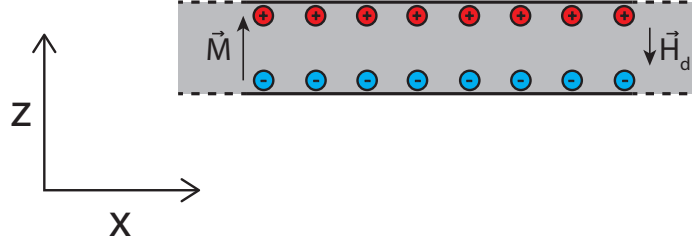$$K_{demag} = -E_{demag} = -\frac{1}{2}\mu_0 M_z^2 \tag{2.8}$$

.

Figure 2.3: An infinitely long film with an OOP magnetization . Surface charges can be introduced which cause a demagnetizing field $\vec{H}_\mathrm{d}$ interacting with $\vec{M}$.

Magneto-elastic anisotropy By introducing stress in a magnetic layer, the crystal structure can be altered which, because of the SOC between electrons and the lattice, alters the anisotropy of the system. This contribution is called the magneto-elastic anisotropy K_me. K_me in a system can originate from a lattice mismatch between adjacent layers in the multilayers. Up to a certain thickness t_c, the mismatch can be compensated for by inducing a strain in the magnetic layer which makes K_me a volume contribution. This is called the coherent region but beyond t_c, it becomes energetically more favorable to introduce misfit dislocations in the crystal structure making it incoherent. This is called the incoherent region and K_me contributes to K as a surface contribution here.

Anisotropy as a function of thickness The three discussed contributions to K are either surface or volume contributions, with K_me changing from volume to surface above t_c. A theoretical plot of Kt_Co as a function of t_Co for the samples used in this thesis is shown in figure 2.4. An increase in Kt_Co can be seen up to $t_\mathrm{Co} = t_\mathrm{c}$, after which Kt_Co starts decreasing. To describe this behavior, we define K for the coherent and incoherent region, since it differs which contributions result from the interface or from the volume in these regions. For the coherent region, this results in

$$Kt_\mathrm{Co} = (K_\mathrm{shape} + K_\mathrm{me}^\mathrm{coh})t_\mathrm{Co} + K_\mathrm{N}, \qquad (2.9)$$

and in

$$Kt_\mathrm{Co} = K_\mathrm{shape}t_\mathrm{Co} + K_\mathrm{N} + K_\mathrm{me}^\mathrm{incoh} \qquad (2.10)$$

for the incoherent region. From equation 2.9 it can be seen that K_N can be found at the intercept in figure 2.4 and $K_\mathrm{S} = K_\mathrm{N} + K_\mathrm{me}^\mathrm{inchoh}$ from the intercept at the intercept of equation 2.10. Also, because K_v (which is the sum of all surface contributions in either region) is positive in the coherent region, $K_\mathrm{me}^\mathrm{coh}$ is bigger than K_shape in our samples. For $t_\mathrm{Co} > t_\mathrm{c}$, the only volume contribution is K_shape so K_v is negative here. At $t_\mathrm{Co} = t_\mathrm{crit}$, also called the critical thickness, K changes from positive to negative (and the anisotropy thus changes from OOP to IP).
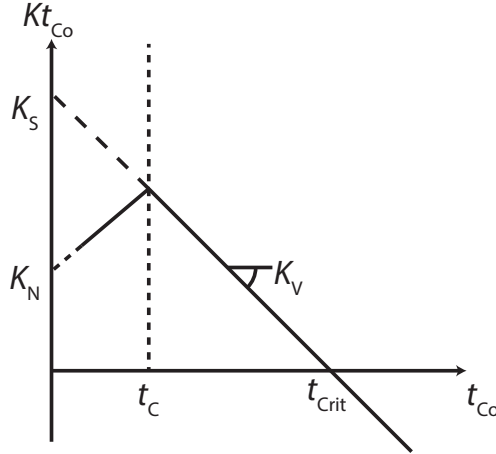
Figure 2.4: Kt_{Co} as a function of t_{Co}. A transition from the coherent to the incoherent region is observed at $t_{\text{Co}} = t_{\text{c}}$. The intercept in the coherent region gives K_{N} and the intercept in the incoherent region gives $K_{\text{S}} = K_{\text{N}} + K_{\text{me}}^{\text{inchoh}}$. In both regions the slope indicates K_{v} which is the sum of all surface contributions. The Co thickness at which the anisotropy switches from OOP to IP is indicated with t_{crit}.

The discussed contributions to K can be tuned with several parameters: the magnetic material that is used, the adjacent non-magnetic materials and the thickness of the magnetic materials. It is therefore important that the right parameters are chosen in order to obtain the desired K.

2.1.3 Dzyaloshinskii-Moriya interaction

Two interactions have been explained so far and both of them suppress the formation of domain walls. However, there is another interaction present which promotes the formation: the DMI, or D in equation 2.1. The DMI is an interaction which in our samples results from the interface between a magnetic and non-magnetic layer and can be derived by calculating the spin-orbit scattering of electrons due to a non-magnetic potential, see [25] for the full derivation. Since a higher SOC would mean more scattering and thus a stronger DMI, a non-magnetic material with a high SOC is preferred. That is why a heavy metal is used as the neigboring material for the magnetic layer.

The energy, E_{DMI}, resulting from the DMI is as follows [26]

$$E_{\text{DMI}} = \vec{D}_{12} \cdot (\vec{S}_1 \times \vec{S}_2), \tag{2.11}$$

with $\vec{D}_{12}$ the DMI and $\vec{S}_1$ and $\vec{S}_2$ two neighboring spins. This equation is most easily explained with the help of figure 2.5a. The neighboring spins $\vec{S}_1$ and $\vec{S}_2$ in the grey, magnetic layer are drawn together with the DMI-vector $\vec{D}_{12}$, resulting from the large SOC in the blue, adjacent layer. According to equation 2.11, E_{DMI} is the lowest when $\vec{S}_1$ and $\vec{S}_2$
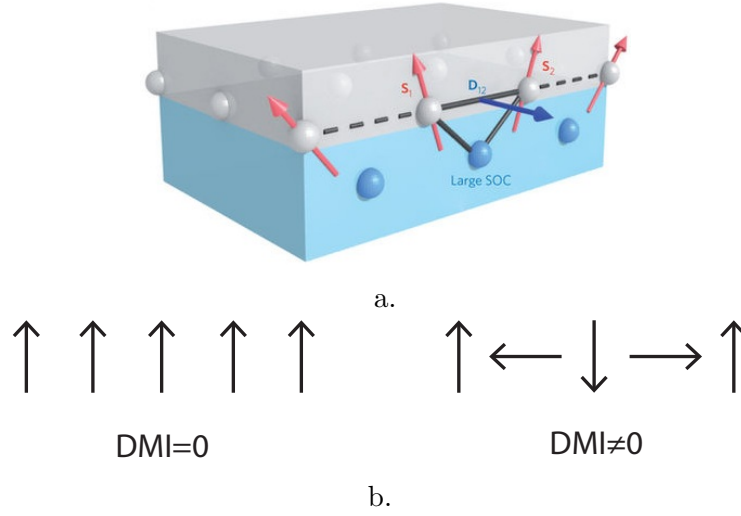
Figure 2.5: a.: DMI in a magnetic layer that is in contact with a heavy metal. The DMI gets larger for heavier metals which makes the neighboring spins ($\vec{S}_1$ and $\vec{S}_2$) want to allign at an angle. Figure from [27]. b.: Introducing DMI in a spin lattice makes the neighboring want to allign at a 90° degree angle.

are at a 90° angle with respect to each other. Exchanging these two spins will change the energy in the system since the cross product changes. Because of this asymmetry which the Heisenberg interaction (equation 2.2) does not have, the DMI is called an antisymmetric exchange interaction. Also the direction of $\vec{D}_{12}$ is important. Changing the sign of D_{12} will change the way the spins want to rotate (also called chirality). Extending D_{12} to the continuum limit results in D which is present in equation 2.1.

DMI wants neighboring spins to rotate which is pictured in figure 2.5b. A row of spins is illustrated for the cases in which DMI is absent and present. Introducing DMI makes the neighboring spins want to be at a 90° angle. DMI thus helps in forming domain walls in thin magnetic layers which is also observed in equation 2.1, where a stronger DMI coefficient $|D|$, reduces the domain wall energy.

A consideration for introducing DMI in a magnetic system is symmetry. When a magnetic layer is brought in contact with a heavy metal material, the introduced DMI is indicated with a vector in the plane of the surface as was already seen in figure 2.5a. However, Pt on both sides of a magnetic Co layer —as shown in figure 2.6a— will result in zero net DMI [25]. Because of symmetry considerations, $\vec{D}_{\text{Pt/Co}}$ in the Pt/Co-system points the exact other way as the $\vec{D}_{\text{Co/Pt}}$ in the Co/Pt-system, canceling each other in the Pt/Co/Pt-
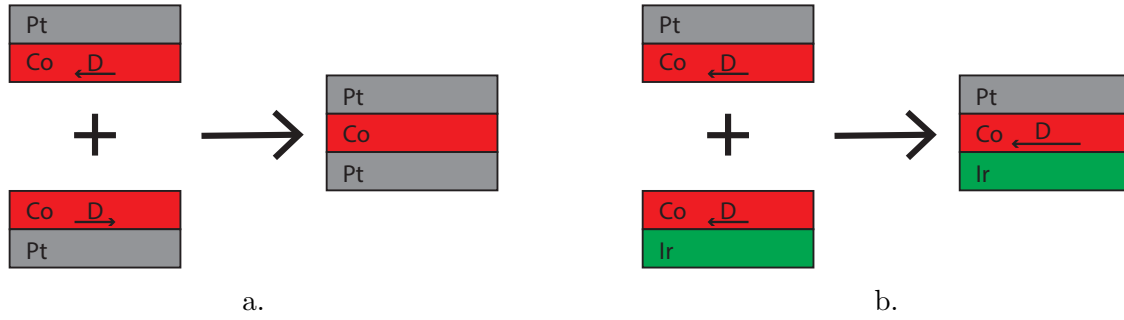
Figure 2.6: a. Pt on Co (top) and Co on Pt (bottom) will reverse the $\vec{D}$ vector. This means that these contributions will result in no DMI at all in a stack of Pt/Co/Pt. b. Since the interface of Ir and Co results in a $\vec{D}$ antiparallel to the DMI resulting from Pt/Co, the Ir/Co/Pt stack will have a net DMI.

system. Chen et al. [28] have found that combining Ir with Co will lead to an antiparallel orientation of $\vec{D}_{\text{Ir/Co}}$ with respect to the $\vec{D}_{\text{Pt/Co}}$ resulting from a Pt and Co combination, as can be seen in figure 2.6b. This is why Ir/Co/Pt is used in the multilayers for this thesis. Because these two DMI vectors are parallel, this will be referred to as additive DMI.

2.1.4 Creating skyrmions with DMI

Let's now consider the situation in which the DMI is large enough to obtain $\sigma < 0$. Because the domain wall energy is negative, it is now energetically favorable to introduce domain walls resulting in a continuous rotation of the spins in the film. This rotation in the spins is called a spin-spiral and a single repeat of a Néel spin-spiral is pictured in 2.7a. Below the spin-spiral, in figure 2.7b, is shown what the domain structure looks like for negative E_{DW}: stripe-domains consisting of Bloch spin-spirals form throughout the film. This picture is a Lorentz transmission electron microscopy (LTEM) image of a $\text{Fe}_{0.5}\text{Co}_{0.5}\text{Si}$ film at $\approx 40\,\text{K}$, adapted from [13], with the white arrows indicating the local magnetization.

The spin-spiral in figure 2.7a already looks like the 1D cross-section of a Néel skyrmion but stripe domains form instead of skyrmions. This can be solved by applying a magnetic field: a magnetic moment wants to align along the magnetic field direction to gain Zeeman energy $(E_z = -\mu_0 \vec{M} \cdot \vec{H})$. Applying the OOP magnetic field results in the Bloch spin-spiral changing to the configuration shown in figure 2.7c. The stripe domain lattice changes under the application of the magnetic field of $50\,\text{mT}$ to a skyrmion lattice. In figure 2.7d, a zoom of a skyrmion is shown from which it can be seen that a Bloch skyrmion has formed.

2.1.5 Dipole-dipole interaction

Because very often the DMI is not strong enough to overcome the anisotropy and exchange energy, another interaction is necessary to gain an effective negative σ. This is the mag-
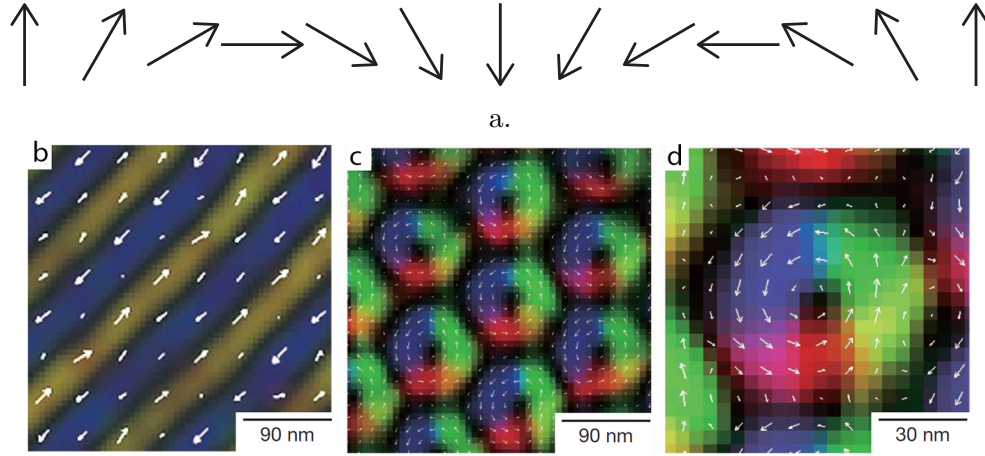
Figure 2.7: a.: If the domain wall energy is negative, it is energetically favorable to form spin-spirals like pictured here. b-d: Lorentz transmission electron microscopy (LTEM) images of a $Fe_{0.5}Co_{0.5}Si$ film at $\approx 40\,K$, all adapted from [13]. The white arrows indicate the local direction of the magnetization with the colors corresponding to a specific direction. b: The Bloch spin-spirals repeat continuously throughout the film which results in the stripe domains that are shown. c: Under the application of a field of $50\,mT$, a skyrmion lattice forms in the film. d: Zoom of one of the skyrmions in the lattice.
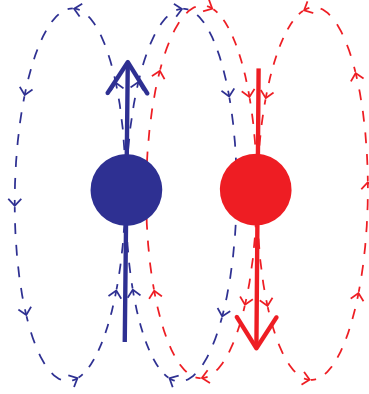
Figure 2.8: Two magnetic moments and their accompanying stray fields. Due to the Zeeman interaction, the moments want to align with the stray field of the other moment.

netic dipole-dipole, or dipolar, interaction. Consider two magnetic moments as in figure 2.8 with their accompanying stray fields. The moments want to align with the stray field caused by the other moment. This causes the antiparallel configuration of the moments to be favorable and promotes the formation of domains, and thus domain walls.

Because the dipole-dipole interaction scales with the volume of the magnetic material, it is not relevant for the nanometer thick layers which we use to gain PMA and high DMI. A solution to introducing the dipolar interaction in the investigated samples is by creating multilayer system as is discussed next.

2.2 Magnetic multilayers and the models to describe them

If a high dipolar interaction is required in our samples, the film thickness has to increase. However, increasing the thickness of the magnetic material reduces the anisotropy coefficient K according to equation 2.10 and will result in an in-plane anisotropy. This is unwanted since, as is discussed in the introduction, PMA is necessary for small domains, like skyrmions, to be stable. Also, since the DMI is an interface interaction, its relevance will shrink to be negligible when volume effects get bigger. That is why simply increasing the thickness of the magnetic layer is not an option.

A solution is sought in using magnetic multilayers, of which a schematic is shown in figure 2.9. An Ir/Co/Pt-system is stacked N times which from here on will be denoted as $[\mathrm{Ir}(t_{\mathrm{Ir}})\mathrm{Co}(t_{\mathrm{Co}})\mathrm{Pt}(t_{\mathrm{Pt}})]_{\times \mathrm{N}}$, with t_{Ir}, t_{Co} and t_{Pt} indicating the thickness of the layers in nanometers. The combination of Ir an Pt is chosen, as is explained in subsection 2.1.3, for the additive DMI they introduce in the system. The Ir/Co/Pt is repeated N times to increase the magnetic volume in the system and make the dipolar interaction stronger
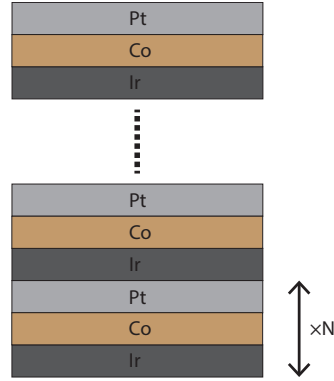
Figure 2.9: Magnetic multilayer system with N repeats of Ir/Co/Pt.

while introducing enough interfaces to retain a large K and D.

However, by using multilayers instead of single layers of Co, the system becomes more complex to describe. For this thesis, the model proposed by Draaisma and de Jonge in [29] is used to find σ in order to calculate D with equation 2.1. The next section is dedicated to explaining this model and the way it is applied in this thesis. Johansen et al. investigated the model by Draaisma and De Jonge in the high field regime [23]. The model they developed will also be used in this thesis to determine which of the two works better for our systems.

2.2.1 Draaisma and De Jonge

Draaisma and De Jonge consider a multilayer system in a multidomain state as shown in figure 2.10, with d_1 and d_2 the widths of the up and down domains respectively and d ($= d_1 + d_2$) the repetition length of the domains in a single layer. The magnetic layers have a thickness t and are separated by a non-magnetic layer of thickness s. The domain walls are assumed to be infinitely thin and freely mobile. Throughout the multilayer, the domains are parallel in the vertical direction and the domain walls are located at the same place in every layer.

In the model, three energy contributions are taken into account to determine the total magnetostatic energy density E_{tot} in the system: the demagnetization energy E_{d}, the domain wall energy E_{DW} and the Zeeman energy E_{h}. These contributions are normalized to the maximum magnetostatic energy $\frac{1}{2}\mu_0 M_{\text{s}}^2$, with M_{s} the saturation magnetization, which results in the dimensionless contributions e_{d}, e_{w} and e_{h}. The total energy in the system is then given by

$$e_{\text{tot}} = e_{\text{d}} + e_{\text{w}} + e_{\text{h}}. \tag{2.12}$$

Draaisma and De Jonge derived an expression for e_{d} by first calculating the potential energy in a single layer as a result of forming a multidomain state. They find that this potential energy is low for small d and high for large d, in line with the earlier discussed
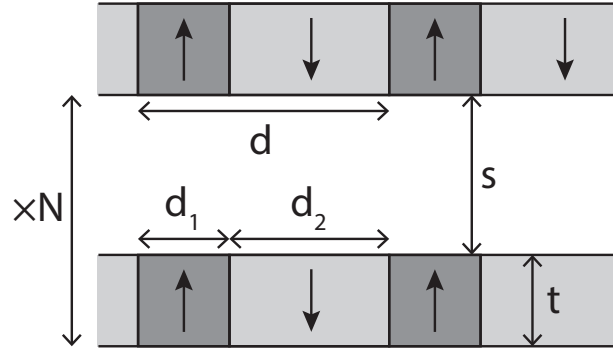
Figure 2.10: Schematic drawing of a magnetic multilayer. The repeats consist of a magnetic film with a thickness t and are separated by a non-magnetic layer of thickness s and are repeated N times. The up and down domains have a width of d_1 and d_2 respectively. The domain repition width is indicated by $d = d_1 + d_2$.

magnetic pole model. Next, they introduce the other layers and find the potential energy of a single layer in a multilayer system. This energy is then normalized to the volume and $\frac{1}{2}\mu_0 M_s$ to yield e_d.

Consider the situation where no magnetic field is applied, so $e_h = 0$. The magnetostatic energy e_{tot} is plotted in figure 2.11 with its two contributions e_d and e_w, all as a function of d. A qualitative analysis will be given about these three energies.

Domain wall energy e_w is the energy of the domain walls in the multilayer. Having few domain walls will mean that e_w goes down which can be seen in figure 2.11. By increasing d, so making the domains bigger, the amount of domain walls in the system is reduced and therefore e_w.

Demagnetizing energy   The demagnetizing energy in a thin film is discussed in 2.1.2 as being a result of magnetic charges on the faces of the film, interacting with the magnetization $\vec{M}$. Just like electric charges, equal magnetic charges repel. With this it can be understood why e_d increases when d increases. If M is saturated, the film will be one big domain and only charges of the same sign will reside on one side of the film. Low d, however, means lots of alternating domains and lots of surface charges of opposite sign on the film its face and thus a lower e_d.

Magnetostatic energy   Adding e_w and e_d results in the magnetostatic energy. The two contributions are in competition: e_w wants large d whereas e_d wants small d. This results in an optimum for d which can also be seen in figure 2.11, a minimum in e_{tot} is reached for $d \approx 0.3\,\mu m$.
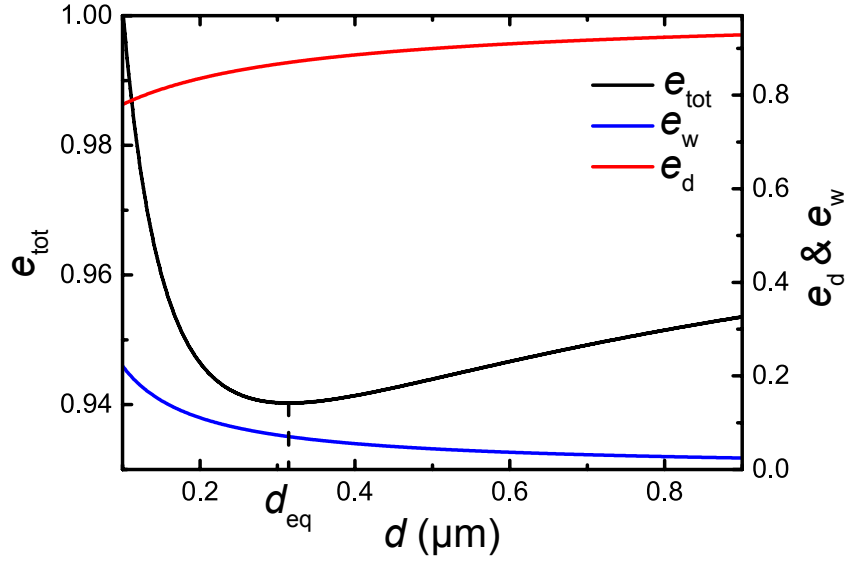
Figure 2.11: e_{tot} is plotted for the situation where $\vec{H} = 0$ with the two contributions e_d and e_w as a function of d. The left y-axis is for e_{tot} and the right y-axis for e_w and e_d. An equilibrium repetition width in e_{tot} is obtained at d_{eq}.

At the energy minimum that was found in figure 2.11, $\frac{\partial e_{tot}}{\partial d} = 0$ applies which can be used to derive e_w when d and e_d are known. In this thesis, d will be determined from the measurements and e_d can be calculated from the models with d, resulting in e_w which can be used in equation 2.1 to determine D.

An example has been discussed in which no external magnetic field is applied. Applying a magnetic field adds Zeeman energy to the system which will increase d: by increasing d the magnetization parallel to the external field increases which minimizes e_h. The d as shown in the example will therefore get bigger if $\vec{H} \neq 0$.

2.2.2 Terminal domain width

Another method of determining the domain wall energy e_w from the magnetic domain widths is the analysis by Johansen et al. [23], which can be considered an extension of the model by Draaisma and De Jonge, and will also be referred to as the terminal domain width model. They consider a single layer of magnetic material which is in a multidomain state as shown in figure 2.12a. It might seem problematic that an analysis for a single layer system is used whereas our system is a multilayer but following the analysis by Buettner et al. in [7], it is possible to scale from multilayer to single layer. A magnetic film with thickness t is shown under an applied field $\mu_0 \vec{H}$ with the domains d_1 antiparallel and d_2 parallel to the field. $\mu_0 \vec{H}$ is increased which eventually saturates the magnetization. This means that d_1 decreases to $d_1 = 0$ but this is not a gradual process: as d_1 decreases it

will gradually reach a critical width, d_c, after which all domains will align with the applied field. How d, d_1 and d_2 respond to the applied field is shown in figure 2.12b. The applied field H is normalized to M_s and d, d_1, d_2 and d_c are normalized to the film thickness t. As the field is increased d and d_2 increase. d_1 asymptotically reaches $\frac{d_c}{t} = r_c$ before the sample is fully saturated at $h_c = \frac{H_c}{M_s}$.

a.

b.
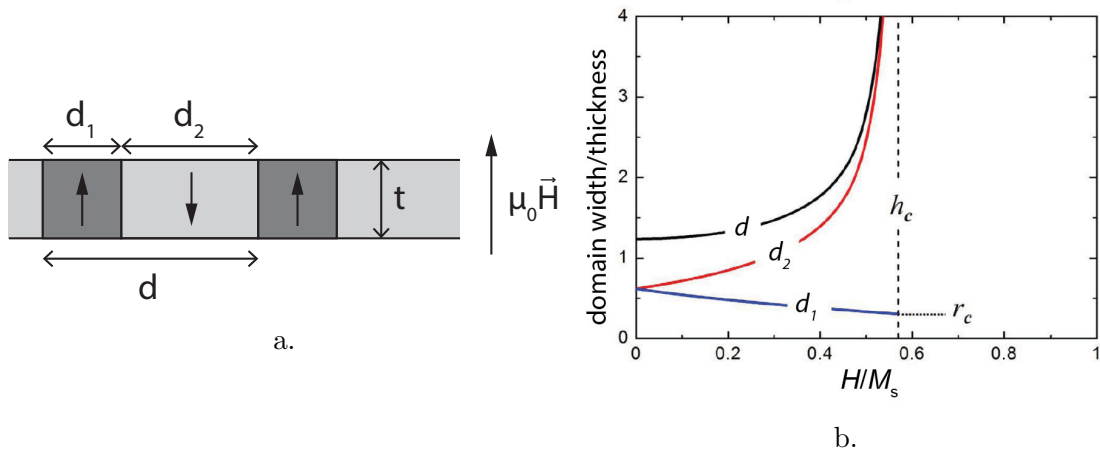
Figure 2.12: a.: A magnetic film with thickness t under the application of external field $\mu_0\vec{H}$ and domain widths d_1, d_2 and $d_1 + d_2 = d$. The arrows indicate the magnetization of the domains. b.: As the field strength is increased d_1 reaches the critical width $r_c = \frac{d_1}{t}$ at $\frac{H}{M_s} = h_c$. Figure adapted from [23].

Johansen et al. derived this functional behavior with equation 2.12, the same three energy contributions as Draaisma and De Jonge used. By minimizing e_{tot} with respect to d and regarding the limit of small $r = \frac{d_1}{t}$ they find that

$$\frac{2\pi}{\mu_0 M_s^2} \frac{\sigma}{t} = \ln\left[1 + r_c^2\right] + r_c^2 \ln\left[1 + r_c^{-2}\right]. \tag{2.13}$$

Here, σ is the energy per unit wall area which is also present in equation 2.1. By measuring r_c, σ can be calculated.

2.3 Measuring the parameters

Two models have been discussed from which σ can be determined. With equation 2.1, the domain wall energy can then be related to the anisotropy and DMI — parameters necessary for characterization of the samples. A direct measurement for D is not used in this thesis so by measuring K and assuming A from literature, D can be calculated when σ is known. K is determined with two methods: from two SQUID-VSM measurements and by fitting the Stoner-Wohlfarth model to anomalous hall effect measurements. These two methods are explained in this section.

2.3.1 Anisotropy from SQUID-VSM

To determine K with the SQUID-VSM, two measurements have to be performed: an out-of-plane (OOP) and an in-plane (IP) measurement. An example of the former is shown in the curve in figure 2.13, where the OOP magnetization (normalized to M_s) is measured of a sample which consists of $[\text{Ir}(1)/\text{Co}(0.6)/\text{Pt}(1)]_{15\times}$, as a function of an OOP magnetic field. Since the field is applied along the anisotropy axis, the OOP measurement is an easy-axis measurement. The measurement starts at large negative field where the system's magnetization is saturated. Next, the field is increased until it reaches large positive field and the system is saturated again in the opposite, positive, direction. Finally, the field is brought back to the field strength from which the measurement started.

What the reversal of magnetization looks like on a microscopic scale is shown in the images below the curve which are obtained with the magnetic force microscope (MFM). The MFM can map the magnetic domains that are present in a sample (more information on the MFM will follow in chapter 3). In this figure, a top view of the sample is provided with the location of the up and down domains indicated in the dark and bright colors, respectively. As the field is increased to be more positive, the dark (up) domains grow larger until they eventually occupy the whole sample at positive saturation.

It is observed in figure 2.13 that the system shows hysteretic behavior. This means that the state of the system depends on its history or specifically, the magnetization of the sample depends on the magnetic fields that have been applied before. At, for example, the field strength of $50\,\text{mT}$, the $\frac{M}{M_s}$ that is measured at B is ≈ 0.5 whereas another datapoint at ≈ 1.0 is present too. Therefore, there is no telling what magnetization the system will have at a certain field strength without knowing the fields that have been applied before. More about the implications of hysteresis will be discussed in chapter 3.

Next, the IP component of M is measured as a function of an applied IP field for a sample with PMA (as shown in figure 2.14), so the field is applied along the hard-axis. Again, the measurement starts at large negative fields, increases to large positive field and moves back to negative. Slight hysteresis is observed in this measurement. The points A, B and C correspond to the schematics below in which it is indicated what the magnetization looks like from a cross-sectional point of view of the film. The spins are gradually pulled away from the easy-axis untill they are all oriented along the magnetic field and saturation is reached.

Both an IP and OOP measurement are shown in figure 2.15. The difference in these two measurements originates from the PMA in the system: in the OOP measurement, the magnetization remains perpendicular to the system since it is an OOP field that is varied. In the IP measurement, the magnetization is pulled away from the easy axis until it is along the hard axis. This means that in the OOP measurement no anisotropy energy has to be overcome to saturate the sample along the field whereas in the IP measurement it is maximal, as can be seen from equation 2.4. By calculating the difference in energy
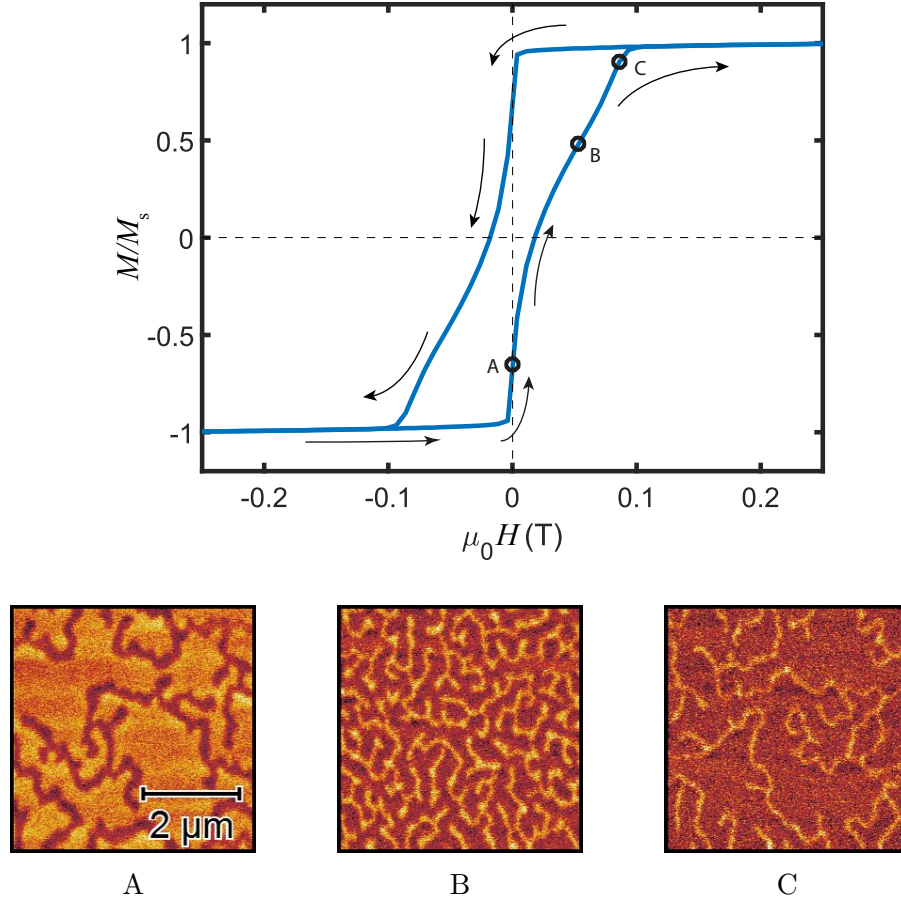
Figure 2.13: OOP hysteresis loop measured with the SQUID-VSM. The measurement starts at large negative field and moves towards large positive field after which it makes its way back to negative field. Points A, B and C label the accompanying MFM-measurements that are shown below. The light area shows the down domains and the dark areas the up domains. The scans at A, B and C are made at an OOP external field $\mu_0 H$ of $0\,\text{mT}$, $50\,\text{mT}$ and $90\,\text{mT}$ respectively.
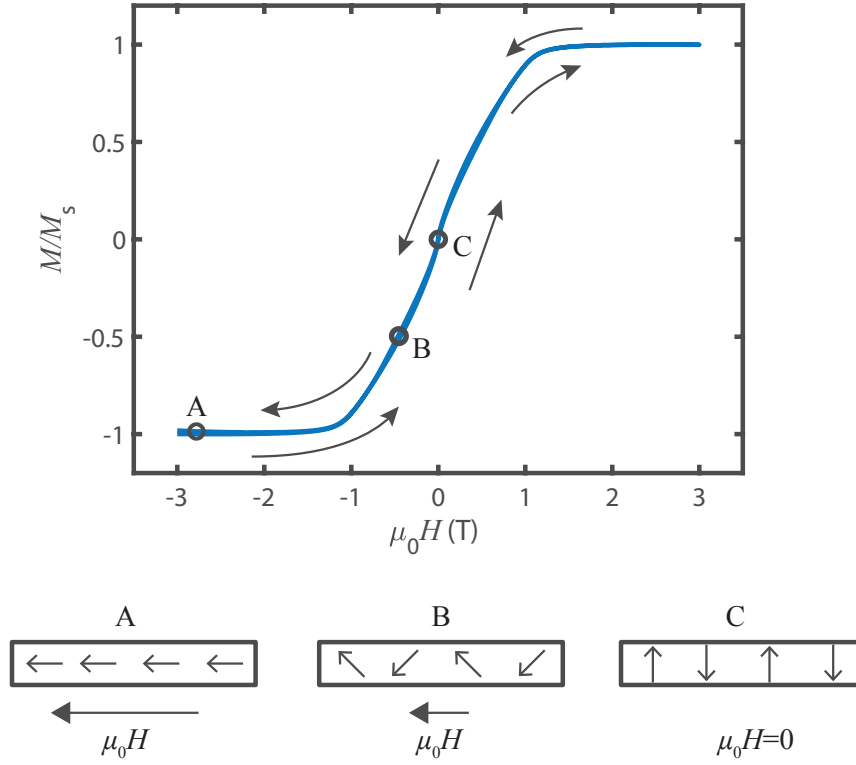
Figure 2.14: Measurement of the IP component of M as a function of an IP field on a sample with PMA. The measurement starts at negative field which is then increased to positive field. After this, the field is returned to be negative. The points A, B and C indicate what the spin lattice looks like at these field strengths from a cross-sectional point of view of the film.
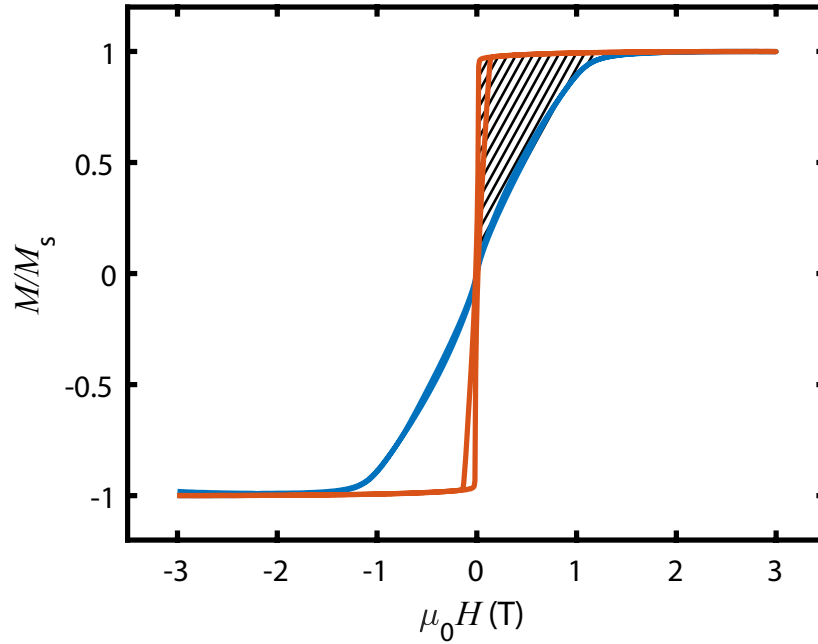
Figure 2.15: An easy (orange) and hard (blue) axis measurement. The shaded area between the curves is calculated to determine K.

needed to saturate the sample IP and OOP, K can be determined. The energy needed to change the sample magnetization by an amount $d\vec{M}$ in an applied field $\mu_0\vec{H}$ is given by the Zeeman energy:

$$dE = \mu_0\vec{H} \cdot d\vec{M}. \tag{2.14}$$

For the curves in figure 2.15, the energy needed to go from $\frac{M}{M_s} = 0$ to 1 is determined by calculating the area below the curve, as shown in equation 2.14. Subtracting these two areas then results in the anisotropy energy (shaded area in the figure between the curves).

2.3.2 Anisotropy from Stoner-Wohlfarth

Another method to determine K is by fitting the Stoner-Wohlfarth model to anomalous Hall effect (AHE) measurements. The Stoner-Wohlfarth model will be explained here as well as a short introduction to the AHE. More about the AHE will be treated in chapter 3.

The Stoner-Wohlfarth model describes how the magnetization in a thin film changes under the application of a magnetic field, a situation as is shown in figure 2.16. A magnetic sample with PMA has its magnetization $\vec{M}$ pulled away from its anisotropy axis by an external magnetic field $\vec{H}$. The angle between $\vec{M}$ and the easy axis is indicated with θ and the angle between $\vec{H}$ and the easy axis as α.

Figure 2.16: Magnetic sample with its OOP magnetization. The external magnetic field $\vec{H}$ pulls the magnetization $\vec{M}$ away from the anisotropy axis. θ indicates the angle between $\vec{M}$ and the easy axis, α the angle between $\vec{H}$ and the easy axis.
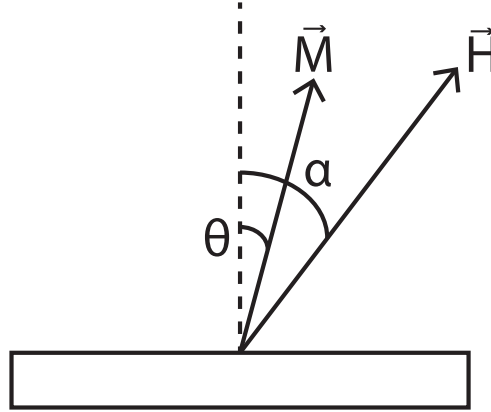
The Stoner-Wohlfarth model calculates the energy in this system as

$$E_{\text{tot}} = K \sin^2 \theta - \mu_0 M H \cos(\alpha - \theta). \tag{2.15}$$

On one hand, there is the energy resulting from pulling the magnetization away from the easy-axis which is the first term in equation 2.15, this is the same as the anisotropy energy from equation 2.4. Increasing θ increases the anisotropy energy in the system. The second term describes the Zeeman energy in the system which is minimalized when $\vec{M}$ is parallel to $\vec{H}$.

With the AHE, we are able to vary α and measure the OOP component of $\vec{M}$ (M_z) as a function of H as is shown in figure 2.17. For various α, M_z is measured as a function of $\vec{H}$. For $\alpha = 0°$, a hysteresis loop like shown in figure 2.15 is obtained. However, for large α, M_z at saturation decreases up until the point where it's almost zero at $\alpha = 90°$.

To fit the Stoner-Wohlfarth model to the AHE, equation 2.15 is used in combination with the assumption that throughout a measurement, the system is in an energy minimum, so $\frac{\partial E}{\partial \theta} = 0$. Applying this to equation 2.15 results in

$$K = \frac{\mu_0 M H \sin(\alpha - \theta)}{2 \sin \theta \cos \theta}. \tag{2.16}$$

An iterative process is used in which first a starting value for K is assumed. Next, since M, H and α are known throughout all the measurements, a minimum is numerically determined in equation 2.15 to find θ. This θ is then used in equation 2.16 to find K. With the newly determined K, the process is repeated until K converges.
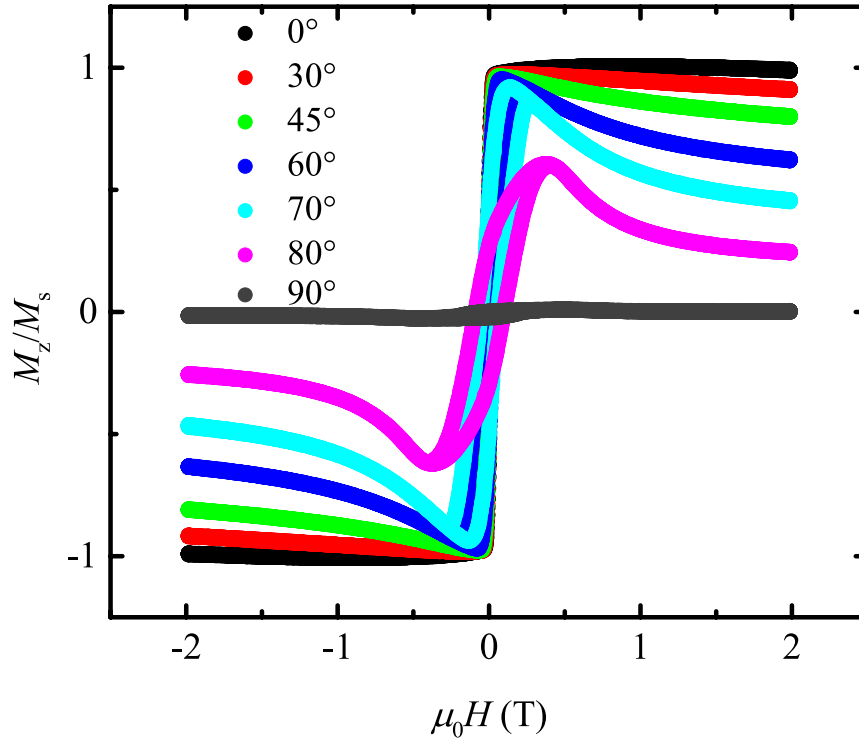
Figure 2.17: AHE measurements of M_z as a function of H for various α.

To summarize this chapter, it is first explained which interactions play a role in the formation of domain walls in a single magnetic film. However, A, D and K are not sufficient if small magnetic domains, like skyrmions, are wanted. The dipolar interaction is necessary too which is introduced by using multiple repeats of a magnetic film. This has the benefit that the magnetic volume can be increased while at the same time also increasing the amount of surfaces from which D and K_N originate. Next, the model by Draaisma and De Jonge [29] is discussed which is used in this thesis to determine σ. Also the analysis by Johansen et al. [23], which is the high-field limit of the model by Draaisma and De Jonge, is discussed since both will be used in this thesis to find out which applies best to our samples. Finally, it is discussed how K is determined with the SQUID-VSM and by fitting the Stoner-Wohlfarth model to a series of AHE measurements.

In the next chapter, it will be explained what methods are used to create and characterize our samples. Also, some practical considerations of the models as well as fitting the Stoner-Wohlfarth model will be discussed.

Chapter 3

Experimental Methods

The relevant physics for this thesis has been discussed but it is not yet treated how the samples are produced. This section will treat sputter deposition and electron beam lithography (EBL) which is used to produce samples and devices. Next, Ga^+-irradiation is discussed which is used to tune the systems. After sample production, the setups used to characterize the systems will be treated. These are the already mentioned SQUID-VSM, AHE-setup and MFM. We use the first two to measure the response of the sample's magnetization as a function of an external field and the MFM to map the magnetic domains of a sample, with the possibility to apply an OOP field.

3.1   Sample fabrication

3.1.1   Sputter deposition

The method we use to produce our samples is sputter deposition with which nanometer-thick layers can be grown on top of each other. It is a relatively cheap deposition technique with a thickness homogeneity of several cm [22]. This makes it an attractive method for industry. However, a disadvantage of this method is that the materials deposited on top of each other intermix, causing diffuse interfaces. This lowers the strength of the surface interactions D and K_s. Nonetheless, we use sputter deposition due to its low cost and its wide application in industry.

The sputtering process is schematically pictured in figure 3.1. Here, a sputter chamber is shown in which the substrate ($100\,nm$ SiO_2 on Si) is placed, together with the to be deposited material (also called the target). The chamber is maintained at a high vacuum ($\approx 10^{-9}\,mbar$) when no process is running but is increased to $1 \times 10^{-2}\,mbar$ by allowing an Ar-flow in the system if a material has to be deposited. Next, the target is negatively charged with respect to the chamber (ΔV) which creates an argon plasma above the target. The Ar^+-ions are accelerated towards the target (using ΔV) and upon collision add energy to the target. This energy can cause the release of an atom which moves towards
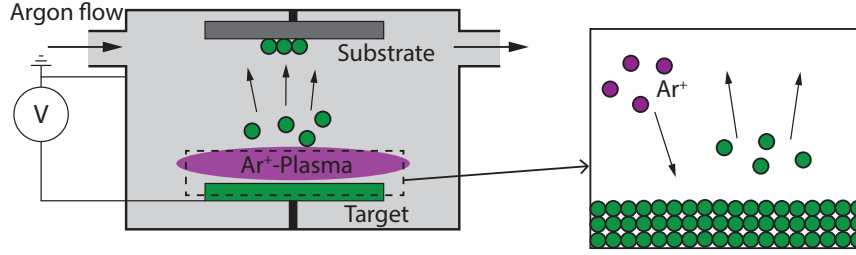
Figure 3.1: Sputter chamber in operation. By applying a negative voltage over the target with respect to the sputter chamber, an Ar^+-plasma is created above the target. The Ar^+-ions are accelerated towards the target due to the negative voltage and collisions of Ar with the target causes atoms to be released from the target which are then deposited on the substrate. The zoom on the right shows collision of the Ar^+-ions with the target upon which target atoms are released.

the substrate and adheres there so the material can be grown per layer. A homogeneous layer of the sputtered material will grow on the substrate over time. The deposition rates that we use range from $0.33\,\text{Å}\,\text{s}^{-1}$ to $1\,\text{Å}\,\text{s}^{-1}$.

3.1.2 Electron beam lithography

For the production of devices, micrometer-scale structures, extra processing steps are necessary. These structures are made using electron beam lithography (EBL) and the process is schematically depicted in figure 3.2. In the first step a layer of resist is deposited on the substrate. This layer contains the polymer polymethyl-methacrylate (PMMA). In step 2, a pattern is 'written' in the layer of resist with the electron beam. The polymers that are exposed to the beam break after which they dissolve when they are bathed in a mixture of isopropanol (IPA) and methyl isobutyl ketone (MIBK), which is step 3. Next, the material is sputtered as is shown in step 4. Finally, acetone is used to wash away the remaining resist and the material on top of it. This is the lift-off step and only the structure is left. The procedure that is described here is based on research done by Casper Schippers and more information can be found in his thesis [30].

3.1.3 Gallium irradiation

The last processing step that we use is Ga^+-irradiation. This is used to induce intermixing of the multilayers which means altering the surface interactions K_s and D. The irradiation process is pictured in figure 3.3a: Ga-ions are accelerated from a source to the sample where they collide with the atoms in the lattice. The most widely accepted model that describes this collision is the collision cascade model [31]. When a Ga-ion collides with an atom in the solid, the atom is displaced when an energy larger than the displacement energy is transferred. This is the energy needed to move the atom away from its original location creating a vacancy. The displaced atom might have enough energy to displace
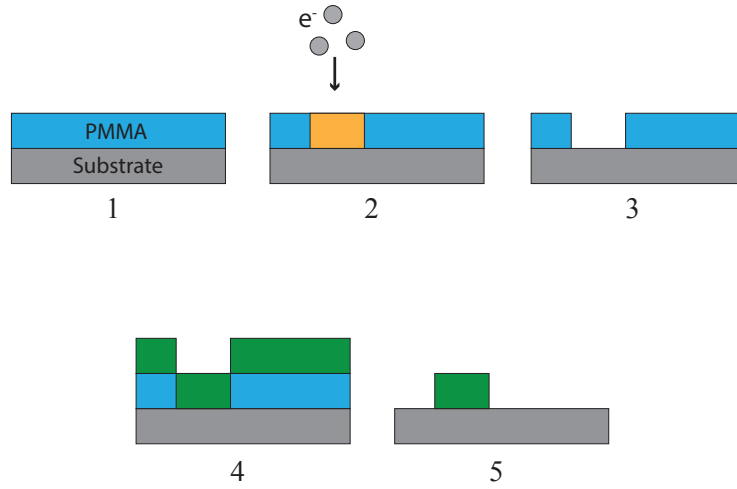
Figure 3.2: Production steps for creating structures with EBL. 1) A layer of resist (PMMA) is applied on the substrate. 2) The resist is irradiated with an electron beam. 3) The irradiated area is disolved in a mixture of IPA and MIBK, also called development. 4) Material is sputtered on top of the sample, indicated as the green layer. 5) The resist that is left on the unirradiated areas is disolved with acetone (also called lift-off) and only the irradiated pattern is left.

other atoms in the lattice too. Also, the Ga-ion might not have lost all its energy upon the first collision which means it could displace other atoms further on in its interaction with the solid. This process continues until the Ga-ion and the displaced atoms have lost their energies and what is left is a multilayer with enhanced intermixing of the different layers.

Intermixing is more explicitly pictured in figure 3.3b. An Ir/Co/Pt stack is shown with K_s and D resulting from the interfaces between Ir, Co and Pt. Before the irradiation, so the situation on the left, the interfaces between the different materials are sharply defined. However, after irradiation, intermixing between the materials is obtained which reduces how sharp the interfaces are defined and with that the strength of K_s and D.

Acceleration voltage and dose (Ga$^+$-ions/cm^2) are among the parameters that can be tuned when irradiating the systems. In this thesis, an acceleration voltage of $30\,\text{keV}$ and an ion current of $1.6\,\text{pA}$ is used. The current is kept low since this allows for subtle tuning of the sample and higher currents or higher voltages can result in sputtering of the sample. It is the gallium dose that is varied in this thesis: increasing the dose means increasing intermixing of the multilayers. In other studies, a dose between $0.1\,\mu\text{C}\,\text{cm}^{-2}$ and $1\,\mu\text{C}\,\text{cm}^{-2}$ is typically used [32, 33].

The effect of Ga$^+$-irradiation on K in single repeats has been studied by, for example, Jeroen Franken whose result is shown in figure 3.4 [32]. A decrease in K_{eff} (or K) is observed as the Ga$^+$-dose is increased which is ascribed to stress relieve in the Co-layer and

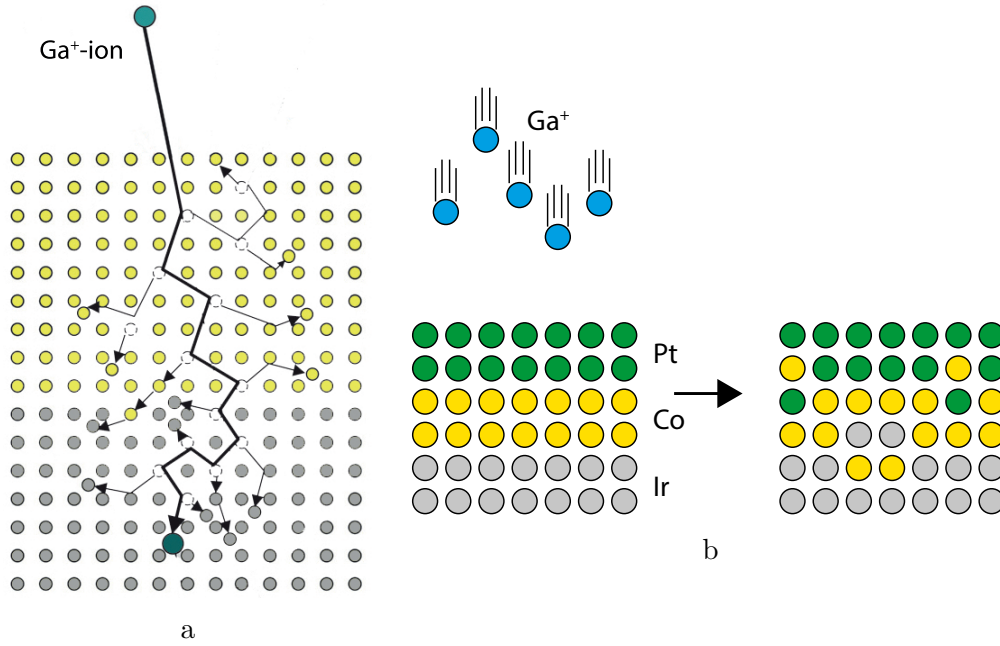Figure 3.3: a: A multilayer (the different materials indicated with yellow and grey) is irradiated with Ga^+-ions. Impact of the Ga^+ can displace the atoms. The displaced atoms can gain enough energy to displace others. Also, the Ga^+-ion might still have enough energy to displace more atoms. Picture adapted from [31]. b: Schematic depiction of an Ir/Co/Pt layer before and after Ga^+-irradiation..
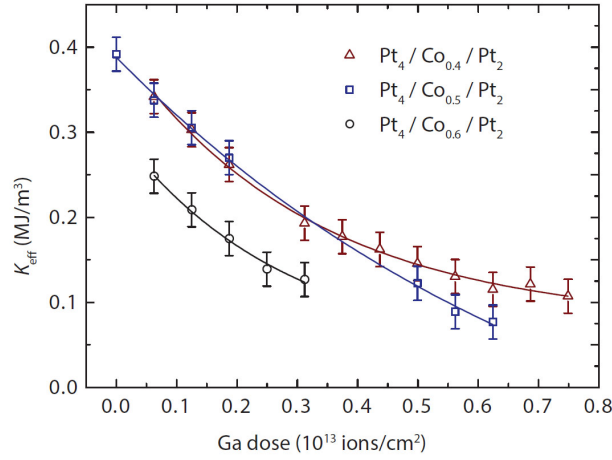
Figure 3.4: K_{eff} (in this thesis indicated as K) as a function of Ga$^+$-dose in a Pt(4)/Co(0.4/0.5/0.6)/Pt(2) system. Figure from [32].

intermixing at the Co/Pt interfaces which lowers K_{s}. For M_{s}, however, Franken observes no trend. Balk et al. [16] found that with Ar$^+$-irradiation, D in a Pt/Co/Pt-system could be tuned without altering K. No information is found on how D in Ir/Co/Pt multilayers can be tuned with Ga$^+$-irradiation.

3.2 Measuring hysteresis

After a sample is produced, one of the steps of characterizing them is measuring their hysteretic behavior as was already explained in chapter 2. The SQUID-VSM has already been mentioned as a tool to measure the response of the magnetization to an externally applied field just like the AHE-setup. These two methods will be explained in more detail in this section.

3.2.1 SQUID-VSM

SQUID-VSM stands for superconducting quantum interference device-vibrating sample magnetometer and is schematically pictured in figure 3.5. A sample is mounted on a sample holder which is positioned in an electromagnet and next to the pickup components. In the SQUID-VSM, the SQUID serves as a pickup component but the exact working mechanisms of the SQUID are not relevant for this thesis so they will not be discussed. As the sample is vibrated up and down (indicated by the double arrow), the magnetic flux detected by the pickup component changes, which can be related to the magnetization of the sample. With the electromagnets, a magnetic field can be applied so the hysteresis curve ($\vec{M}$ as a function of $\mu_0\vec{H}$) of the sample can be measured. A down side of the SQUID-VSM is that it is a relatively slow tool and can only measure the complete magnetization of the sample (or bulk magnetization) and not local changes in the magnetization.
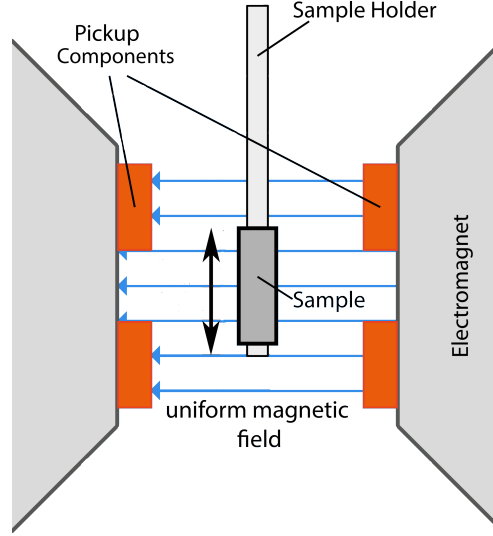
Figure 3.5: Shematic of the SQUID-VSM. A sample is vibrated which induces a signal in the pick-up components (consisting of the SQUID), proportional to the sample's $\vec{M}$. A magnetic field can be applied using the electromagnet which allows for the measurement of $\vec{M}$ as a function of $\mu_0 \vec{H}$.

3.2.2   Anomalous Hall effect

In some measurements the anomalous Hall effect (AHE) is used to determine a sample's hysteretic behavior. With the AHE, hysteresis of small areas can be measured (in this thesis $5\,\mu m \times 5\,\mu m$) which is not possible with the SQUID-VSM. These measurement exploit the AHE which at first sight looks a lot like the ordinary Hall effect (OHE): a current sent through a conductor is deflected when a magnetic field is applied. However, in the case of the AHE it is the magnetization of the conductor that deflects the current in contrast to the OHE where it is the interaction of the current with the external field.

In figure 3.6, the AHE is demonstrated. A top view of a magnetized metal is shown through which an electron flow is sent. The electrons (e^-) interact with the OOP magnetization and are deflected, resulting in a charge accumulation on the sides, indicated with ΔV. Deflection of the electrons results from spin-orbit interaction between the electrons and the atoms but for more information about this process, the reader is referred to [34]. By sweeping the magnetic field, the magnetization of the strip changes and with that ΔV, resulting in a hysteresis measurement of the magnetization of the strip. Note that only the OOP component of $\vec{M}$ is determined since this induces the potential difference over the sides of the conductor. An IP component of the magnetization would cause a charge accumlation at the top and bottom of the conductor.

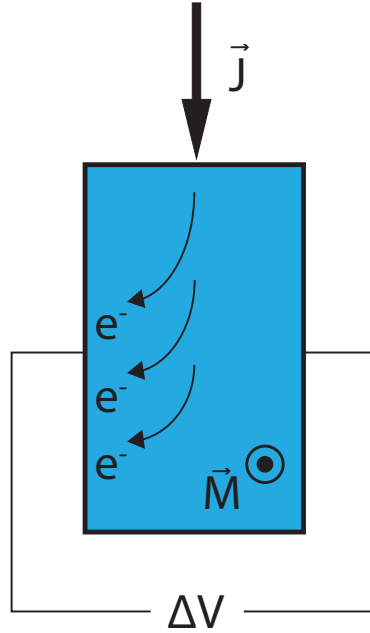In figure 3.7, the structure is shown that is used to measure the AHE. A current is sent

Figure 3.6: Top view of a magnetized conduct through which an electron flow $\vec{J}$ is sent. The magnetization of the conductor, $\vec{M}$, deflects the electrons (e^-) due to the AHE which accumulate on the side of the conductor. This results in a potential difference over the sides of the conductor.

through the structure which is made out of the magnetic multilayer described in section 2.2.1. The magnetization deflects the current and the charge accumulation can be measured as ΔV over the irradiated area by probing the upper and lower rows of contacts. A magnetic field is applied perpendicular to the structure to perform a hysteresis measurement. The areas indicated with the red, dashed squares are irradiated with gallium as described in section 3.1.3. This makes it possible to relate irradiation dose to the effective anisotropy with the help of the Stoner-Wohlfarth model, as described in section 2.3.2. With Ga^+-irradiation, it's only possible to irradiate areas in the micrometer range which is why it is necessary to use the AHE. Loading an irradiated sample, being only a few square micron in size, in the SQUID-VSM is not realistic and would result in an immeasurable signal.

3.2.3 The effect of hysteresis on the models

Two methods have been discussed which can measure the response of $\vec{M}$ to $\mu_0\vec{H}$. However, as is already discussed in section 3.2.3, the samples show hysteretic behavior which can be problematic for the analysis of the data. The models by Draaisma and de Jonge and Johansen are used to determine e_w from the parameters d and r_c. Because the investigated samples show hysteretic behavior, it is important to follow one single methodology when measuring d or r_c in different samples. This means that every characterized sample

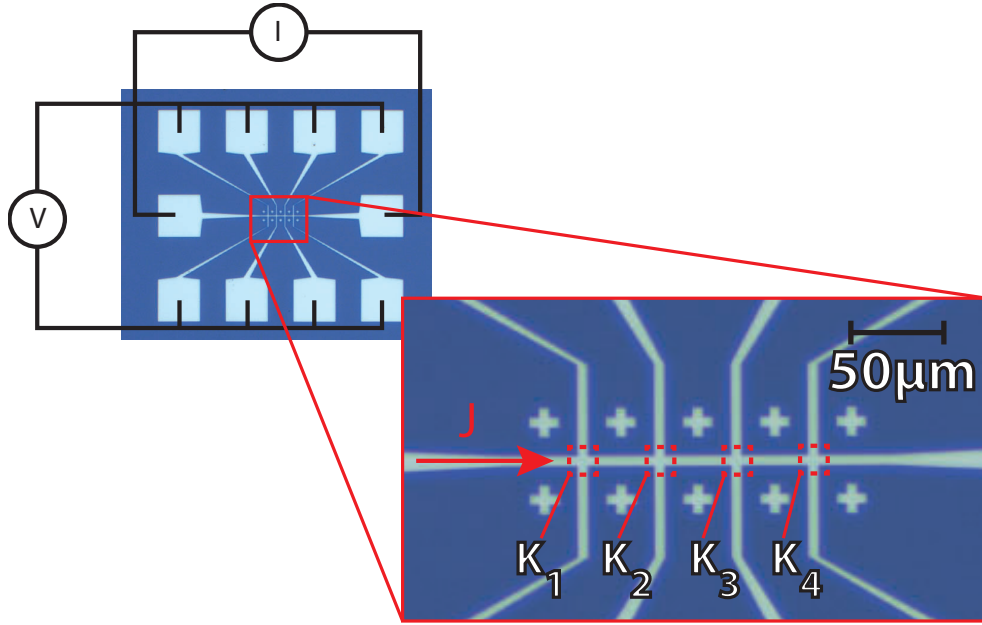Figure 3.7: Structure used to measure the AHE. A current is sent along the path which is deflected due to the magnetization of the multilayer structure. Each pad in the top and bottom row serves for probing the voltage difference over the irradiated area which is a measure for OOP magnetization. The red, dashed squares indicate the irradiated areas which anisotropy K_1, K_2, K_3 or K_4 can be determined separately.
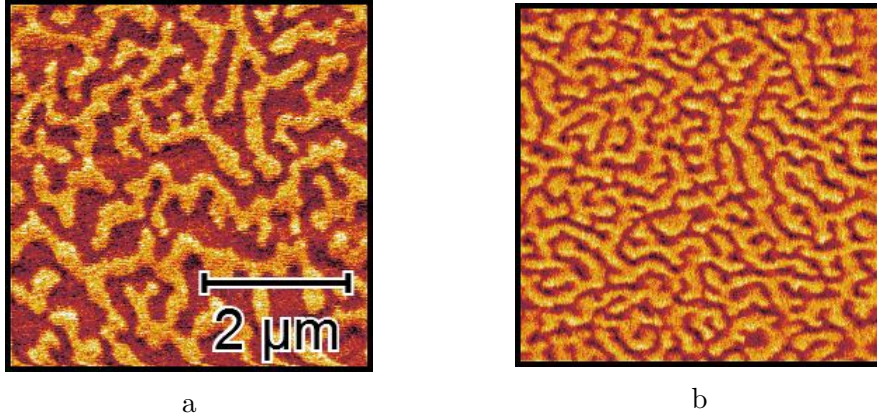
Figure 3.8: a: Magnetic force microscopy image of an as-grown multilayer. The different colors indicate different directions of the magnetization (either up or down). A single periodicity in the domain repetition length is absent. b: MFM scan of a multilayer system under the application of $\mu_0 H = 24\,\text{mT}$ after being saturated at negative field. The repetition width is more constant in this scan compared to a.

should have the same history of magnetic fields that have been applied in order to rule out hysteresis as a factor for varying results.

A second problematic aspect of the model by Draaisma and De Jonge is that it is not trivial to reach a multidomain state which has a constant d throughout the sample. An example of the domain structure of a sample right after production (also called its as-grown state) is shown in the MFM-scan in figure 3.8a. The width of the domains varies a lot in this scan which is not to be expected from the discussed model, which predicts a constant d. That the sample ends up in this domain configuration is a result of the system containing imperfections which alter the energetic landscape of the magnetization while the models assume the system to be in a global energetic minimum. It is not trivial to reach the energetic ground state and no consensus is reached yet on which method should be applied to reach it. Hellwig et al. [35] propose applying an IP field which cycles down in successive loops while decreasing the amplitude by 0.1% in each step. They indicate that this should help the system in finding its lower energy state, but this cannot be verified.

To circumvent the problems caused by hysteresis and the system not reaching its energetic ground state, a fixed procedure is followed when a measurement is performed for determining d. It is tried to reach an energy minimum by following the sample its hysteresis curve, like shown in figure 2.13. Saturating the sample at large negative field and then increasing the field to $\approx 20\,\text{mT}$ results in $\frac{M}{M_\text{s}} = 0$ which means that d_1 and d_2 are equal in size. At this field strength a scan as in figure 3.8b is obtained. Here, d_1 and d_2 are not equal in size but vary less throughout the scan and a constant d seems present.
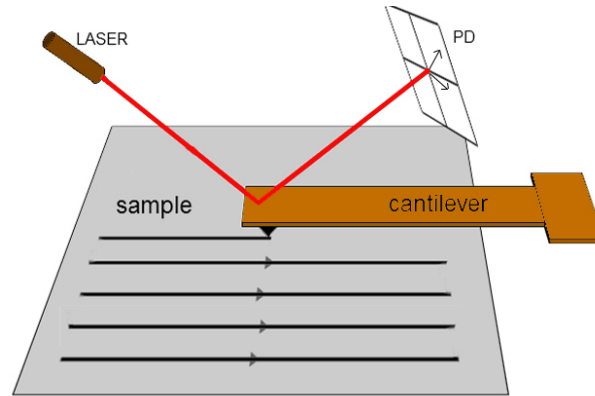
Figure 3.9: In AFM, the tip on a cantilever is brought close to a sample's surface. A laser is focused on the back of the cantilever and reflected on a photo-detector (PD) which is used to measure the deflection of the cantilever. The tip is then scanned along the lines indicated on the surface. In a tapping mode scan, the amplitude of the tip's oscillation is measured with the PD to map the surface. Picture adapted from [36].

3.3 Atomic and magnetic force microscopy

The last tool that is used to characterize magnetic samples is the magnetic force microscope (MFM). It has been mentioned a few times already as a way of imaging magnetic domains in the samples and is used extensively in this thesis. This section discusses the working principle of the MFM. MFM is part of the scanning probe microscopy family and can be seen as an extension of atomic force microscopy (AFM) which will therefore be explained first.

3.3.1 Atomic force microscopy

In AFM, a tip is held in a vibrating mode, at its resonance frequency (typically 45 kHz to 115 kHz), and brought close to the samples surface. The distance between tip and sample is such that the tip touches the surface at its lowest point in the oscillation.

When the tip is rastered across the surface, as shown in figure 3.9, it will encounter variations in surface height. The differences in height will alter the amplitude of the oscillation: if there is a depression in the surface, the tip has more room to oscillate whereas an elevation in the surface reduces the amplitude. A laser is focused on the cantilever which reflects the light on a photo detector (PD). During oscillation, the reflection on the cantilever changes and with that the position of the spot on the PD. It is the amplitude of the reflection that is used to determine the topography of the sample.

The scanning mode that is discussed above is called the semi-contact or tapping mode scan. There are other modes available, like the contact mode, but these are not used in

this thesis and will therefore not be discussed. More information on the AFM can be found in [37].

3.3.2 Magnetic force microscopy

To map magnetic domains with the MFM, an AFM-tip coated with magnetic material is necessary. Two steps, or passes, are needed to make an MFM scan. In the first pass, the topography of the sample is mapped, which is done as described previously with a tapping mode scan. When the topography is known, a second scan is made. In this second pass, the tip is again held in a vibrating mode at resonance but retracted further from the surface. No contact is made with the sample as the tip oscillates which is why this mode is called the non-contact mode. In this thesis, a commercially available tip is used which has a CoCr layer of 15 nm, a the typical thickness for the magnetic coating on the tip.

Again, the tip is rastered along the surface but this time at a constant distance between tip and sample (30nm in this thesis), which is possible as the topography has been mapped in the first step. It is important to maintain a constant separation so the van der Waals force between tip and sample remains constant. Because the tip is coated with a magnetic material, it interacts with the magnetic stray fields coming from the sample.

The non-contact mode scan is schematically depicted in figure 3.10. An MFM tip is shown which is driven at its resonance frequency. A zoom-in of the tip is present where the magnetic coating of the tip can be seen with its magnetization direction. Note that the magnetization of the tip is not solely along the vertical direction but also has a horizontal component. Since the vertical component of the magnetization is the biggest, the magnetization of the tip will be indicated by this component from here on, i.e. if the tip has an 'up' magnetization, this means that the vertical component is pointing upwards.

Below, the magnetic sample is shown with both an up and a down domain. As the tip scans these domains, its oscillation frequency changes, resulting from the interaction between the magnetic tip and the magnetic sample. If the tip scans a domain which magnetization is anti-parallel to the tip's magnetization, the oscillation frequency reduces whereas it increases when it scans a domain which is parallel to the tip its magnetization. Note that in the figure is indicated how the resonance frequency of the tip changes (so lower frequency for anti parallel and higher frequency for parallel alignment between tip and sample) but not the actual oscillation of the tip. The tip is still driven at the resonance frequency determined without any external interactions. Throughout the measurement, the tip is held at a distance Δh from the sample's surface.

The tip's oscillation frequency changes which introduces a phase difference between the
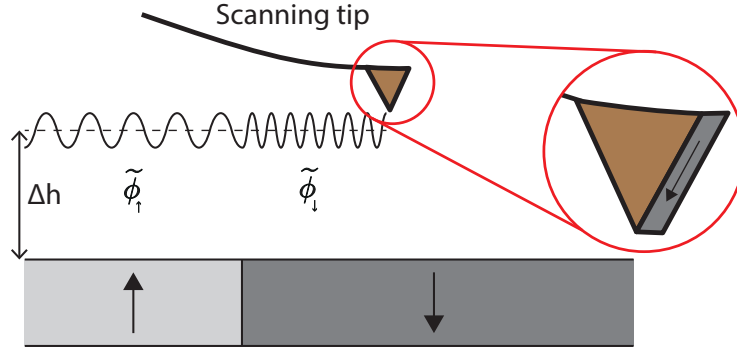
Figure 3.10: Schematic depiction of the non-contact mode pass. The scanning tip is driven at its resonance frequency at a distance Δh from the sample's surface. A zoom-in of the tip shows the magnetic coating with the magnetization of that coating. As the tip scans domains with a magnetization (anti-)parallel to the vertical component of the tip's magnetization, the resonance frequency changes which results in a phase shift $\widetilde{\phi}_\uparrow$ or $\widetilde{\phi}_\downarrow$. Note that it's not the actual oscillation of the tip that is pictured but how its resonance frequency changes, so a lower frequency for anti parallel and higher frequency for parallel alignment between the tip and sample's magnetization.

driving force and the tip's oscillation. This is described by

$$\widetilde{\phi} = \arctan \frac{k}{Q\frac{\partial F}{\partial z}} \tag{3.1}$$

which, for small $\frac{\partial F}{\partial z}$, can be approximated as

$$\widetilde{\phi} \approx \frac{\pi}{2} - \frac{Q}{k}\frac{\partial F}{\partial z}, \tag{3.2}$$

with $\widetilde{\phi}$ the phase difference, k the spring constant for a cantilever without force gradient, $\frac{\partial F}{\partial z}$ the gradient in the magnetic force on the tip and Q the tip's quality factor [36]. The quality factor is a parameter which indicates how fast a resonator loses the stored energy: a high quality factor means that oscillations die out slowly. For the tips in this thesis, a high Q and low k is preferred. The tips have to be sensitive to small domain which means they have to be deflected easily (hence the low k). By increasing the thickness of magnetic coating, $\frac{\partial F}{\partial z}$ increases due to which the deflection of the tip increases as it scans the magnetic domains. A low Q means that oscillations are damped fast and thus that the influence of small domains on the tip becomes harder to detect. $\widetilde{\phi}$ bigger than 90° $(= \frac{\pi}{2})$ results from the tip scanning a domain parallel to its magnetization, whereas a phase difference below 90° results from scanning an anti-parallel domain. It is $\widetilde{\phi}$ that is measured by the MFM setup to map the domains in the sample.

It should be noted that the magnetic tip probes the magnetic stray fields coming from
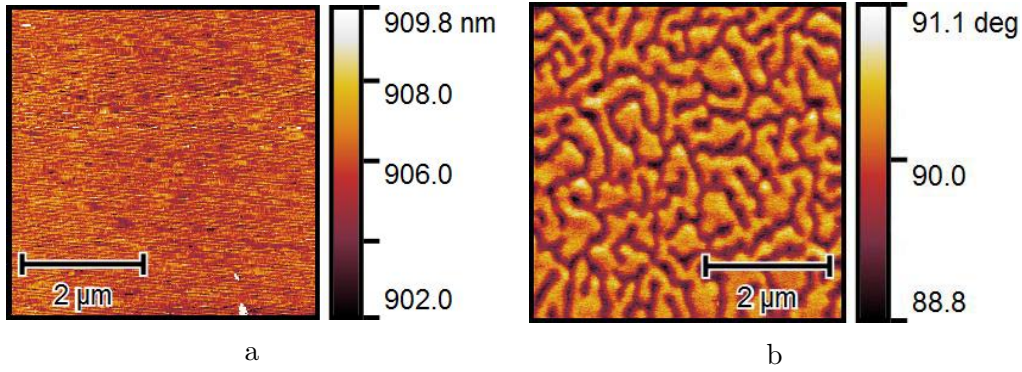
Figure 3.11: a: Example of a topography scan. There is an offset in measured height (≈ 906 nm but the relative height differences are important for the MFM scan. b: Example of an MFM scan. The measured $\widetilde{\phi}$ is approximately 90° as predicted by equation 3.2. Bright domains in the scan correspond to an up domain (so pointing towards the reader) and dark domains to a down domain.

the sample and not the magnetization. This means that an MFM scan does not necessarily depict the exact magnetic domain structure but merely what $\widetilde{\phi}$ is measured at a certain location. Moreover, the magnetization of the tip is not completely along the vertical direction but also has a horizontal component. This means that it is also influenced by magnetic stray fields in the horizontal direction. Care must be taken by what conclusions are drawn from a scan.

In figure 3.11, an example of a topography (a) and the corresponding MFM (b) scan are shown. An offset of ≈ 906 nm is measured in the topography scan which is arbitrary, since only the height difference with respect to this offset is important. White spots can be observed in the topography scan which is attributed to small dirt particles on the surface. Up (bright colored) and down (dark colored) magnetic domains are found in the sample. $\widetilde{\phi}$ that is measured is approximately 90° as predicted by equation 3.2. Most of the time, no valuable data is extracted from the topography scan which is why they will not be shown in this thesis.

The MFM is one of the few techniques which can measure magnetic domains up to a small scale (domains of 80 nm have been measured by us). A big advantage of the MFM compared to other techniques like Lorentz microscopy or the Scanning Electron Miscrope with Polarization Analysis (SEMPA) is that an MFM measurement can be done under ambient conditions without complex sample preparations [36]. Besides that, an external magnetic field can be applied during MFM measurements which is also done in this thesis. The combination of the small scale magnetic domains it can detect, the ease of using it and the possibility to apply an external magnetic field is the motivation to use it in this thesis. However, as is already mentioned, the MFM maps the phase difference between the driving force of the cantilever and the oscillation of the tip, not the actual domains. This

means that care should be taken when interpreting MFM data.

To summarize this chapter, it is explained how the samples are prepared and characterized. Sputter deposition is used to deposit the materials, EBL to create micrometer scale structures and Ga^+-irradiation to alter the atomic structure. SQUID-VSM is discussed as a tool to measure hysteretic behavior of a magnetic sample as well as how the AHE can be used to do so. Finally the MFM is discussed. This setup is used to map the magnetic domains in a sample and its benefits and drawbacks are discussed.

Chapter 4

Optimizing the magnetic force microscope

The MFM is used extensively for this thesis but it turned out to need optimization before it was workable. Problem with the MFM was that the magnetic tip seemed to change the sample's magnetization, which is unwanted since it should only probe the magnetization: when a tip perturbs the magnetic domain state of a sample, no reliable conclusions can be drawn from the scans. No commercially available tip was found which did not show switching behavior in the sample which is why we fabricated them ourselves. This chapter focuses on how we fabricated and characterized them. How the thickness of the Co affects the performance is first investigated qualitatively but also a quantitative analysis is tried to confirm the usability of the tips.

4.1   Tip induced switching of domains

As was already shown in figure 3.10, the tip is either repelled or attracted by the magnetic domains in the sample. This makes it seem as if the magnetization of the tip and the domains is static whereas in reality it is possible that these change. If the tip's magnetization is too large, it will align the domains along its magnetization, thus inducing a switch if a domain is in an antiparallel configuration.

In figure 4.1 is schematically shown what the induced switching is believed to look like. In figure 4.1a, the tip is scanning the sample as shown on the right: in this top view can be seen that it scans the width of the sample step wise. Dark gray is used to depict a down domain and the circle shows an up domain. As the tip scans the up domain, it is possible for the dipolar interaction between tip and sample, shown on the left, to be large enough to switch the magnetization of the domain and result in the situation shown on the left in figure 4.1b. However, part of the up domain has already been scanned, which is shown as the light gray half of the circle in figure 4.1a whereas the red half will not be detected as an up domain anymore since the full domain has switched due to tip-sample interaction.
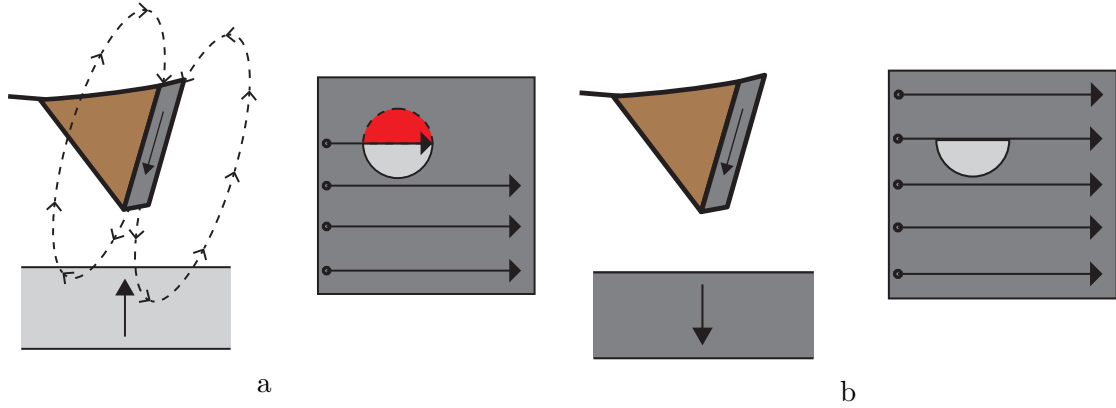
Figure 4.1: Schematic depiction of tip induced switching of a magnetic domain. A sample's magnetization is mapped by stepwise scanning the width with a down domain (shown in dark gray in a) and the circle representing an up domain. As the tip scans the up domain, it is possible for the dipolar interaction between tip and sample (shown on the left in a) to induce a switch in the domain, resulting in the situation shown on the left in b. This means that only the lower, light gray, half of the circle in figure a is scanned whereas the red half won't be scanned since the full domain switched. This results in the scan shown in b which has an abrupt cut-off along the scan direction of the circle whereas a full circle should have been scanned.

The finished scan will then look as the right of figure 4.1b: only the bottom half of the up domain has been interpreted as an up domain whereas to top half could not be scanned as the domain switched. This shows up as a domain that is abruptly cut off. The cut off is also horizontal, along the scan path of the tip.

In figure 4.2 is shown how induced switching is believed to show up in our scans. Three scans are performed on a sample of $[\mathrm{Ir}(1)/\mathrm{Co}(0.6)/\mathrm{Pt}(1)]_{15\mathrm{x}}$. The three successive scans are made under the exact same conditions on the exact same area, under the application of an OOP field of $\mu_0 H = 45\,\mathrm{mT}$. In figure 4.2a, inside the blue encircled area a domain is shown which is believed to be erased during the scanning of the sample. It is believed that switching of the domain happens in the first, tapping-mode, scan where the tip is the closest to the sample and the dipole interaction is therefore the strongest. A few more domains with this abrupt cut off can be identified in figure 4.2a. Two other domains are indicated with the black lines. These are domains that remain stable throughout the three measurements. Comparing the three measurements shows that a lot of domains are erased after three scans and that a tip with a lower interaction with the sample is necessary in order to obtain reliable results. Since it was not possible to buy tips that met the required conditions, it was decided to fabricate them ourselves.
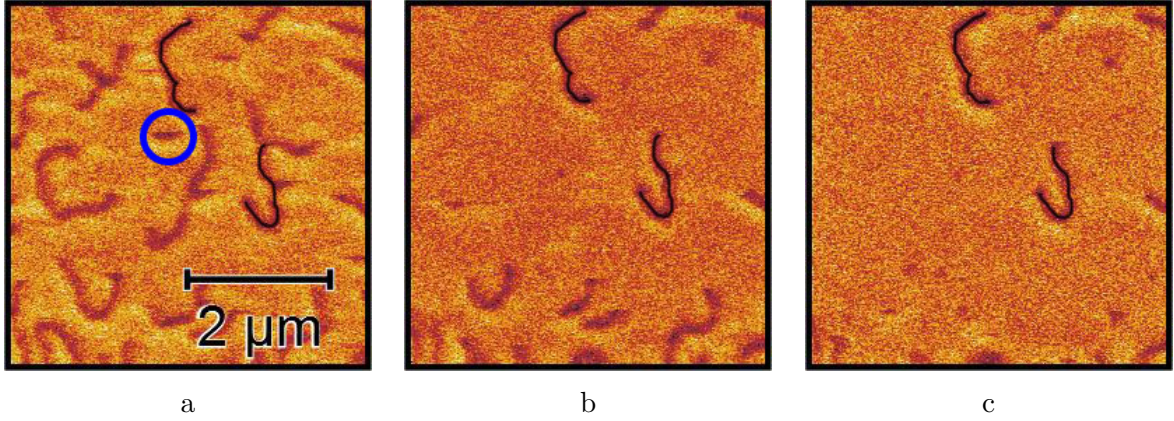
Figure 4.2: Three successive MFM measurements with the commercially available tips under the application of an OOP field $\mu_0 H = 45\,\text{mT}$. Because the tip is magnetically too strong it is able to erase domains through dipolar interactions. The domains that remain throughout the three measurements are marked in black. The blue circle indicates one of many domains which is partly scanned but disappears during the scan.

4.2 Tip quality as a function cobalt thickness

MFM tips are fabricated by coating AFM tips with different thicknesses of Co. The AFM tips that are used are of the type PPP-FMR-20 from the company NanoSensors. Co is not sputtered directly on the tip but on top of a seed layer of Ta which is 2 nm thick, to promote adhesion of Co to the tip. Our fabrication procedure of the tips is based on the technique described by Iglesias-Freire et al. [38]. Three thicknesses of Co have been deposited: 10 nm, 20 nm and 40 nm. In fabricating these tips, a trade-off can be identified: the coating should not be too thick since the interaction between tip and sample will be present but when the coating is too thin, $\frac{\partial F}{\partial z}$ will decrease (as explained in section 3.3.2), lowering the signal-to-noise ratio.

In figure 4.3a is shown what an MFM-tip looks like in the electron microscope, the end of the cantilever with the tip is shown. Figure 4.3b shows where the magnetic material is deposited, with the deposited layers colored green.

Characterizing the tips is done by, again, making three successive scans of the same area of the $[\text{Ir}(1)/\text{Co}(0.6)/\text{Pt}(1)]_{15\text{x}}$ sample. These scans are then compared and checked for domains that have been erased. The result of this procedure is shown in figure 4.4: every row contains three successive scans made with the same tip. The top row is made with the 10 nm tip, the second and third row with the 20 nm and 40 nm tip respectively.

The three scans that are made with the 10 nm tip show no interaction between tip and sample: no domains disappear in these three scans from which it is concluded that the tip's magnetic moment is not too strong. The signal-to-noise ratio of these tips is good

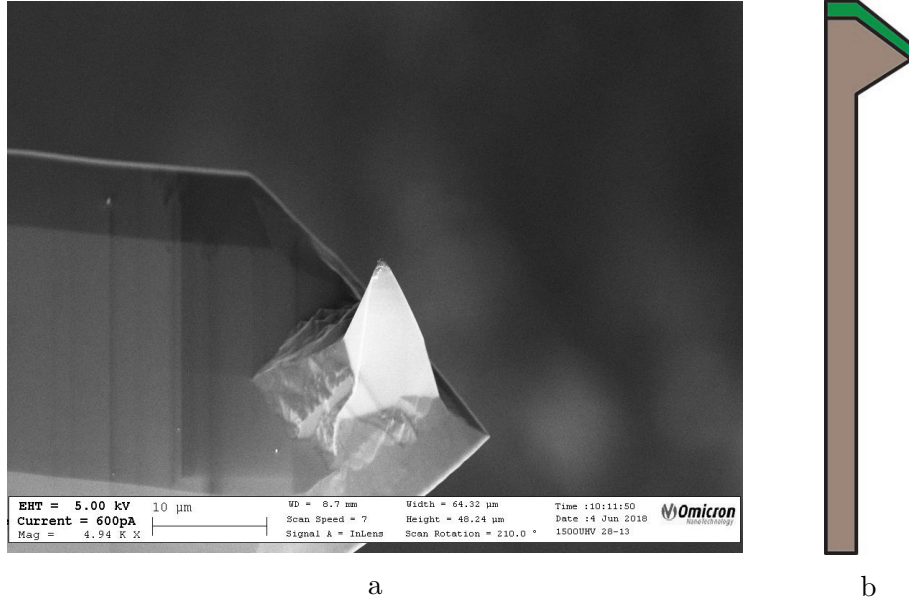a   b

Figure 4.3: a: Electron microscope image of an AFM-tip. The end of the cantilever with the tip can be seen. b: Schematic picture of the AFM-tip with the deposited Co in green.

too, as the domains can clearly be distinguished.

Increasing the thickness to 20 nm, as shown in figures 4.4d-f, results in tip-sample interaction. In figure 4.4d, four domains are marked with green. These domains are not present in the scans shown in figures 4.4e-f anymore which is attributed to the tip-sample interaction. What also clearly indicates the tip-sample interactions in these scans is that there are notably less domains present compared to scans in figures 4.4a-c. Despite the interaction between tip and sample, skyrmions can be observed in the measurements, which remain stable throughout the measurement. The skyrmions are tip induced and it's hard to predict where they will form but it's concluded that this sample is able to contain skyrmions.

Increasing the thickness to 40 nm results in the scans shown in the bottom row. It can be seen that the domains have become more vague in these scans but why this happens is not clear. Interaction between tip and sample could have increased in such a large amount that it disturbs the oscillation which lowers the scan quality. Besides a lower signal-to-noise ratio, the amount of domains that are visible has decreased even more. This makes sense since the amount of magnetic material has increased. An abrupt cut off of the domains seems absent in these scans which would mean that the switching takes place before the domains are scanned, namely in the tapping-mode scan.
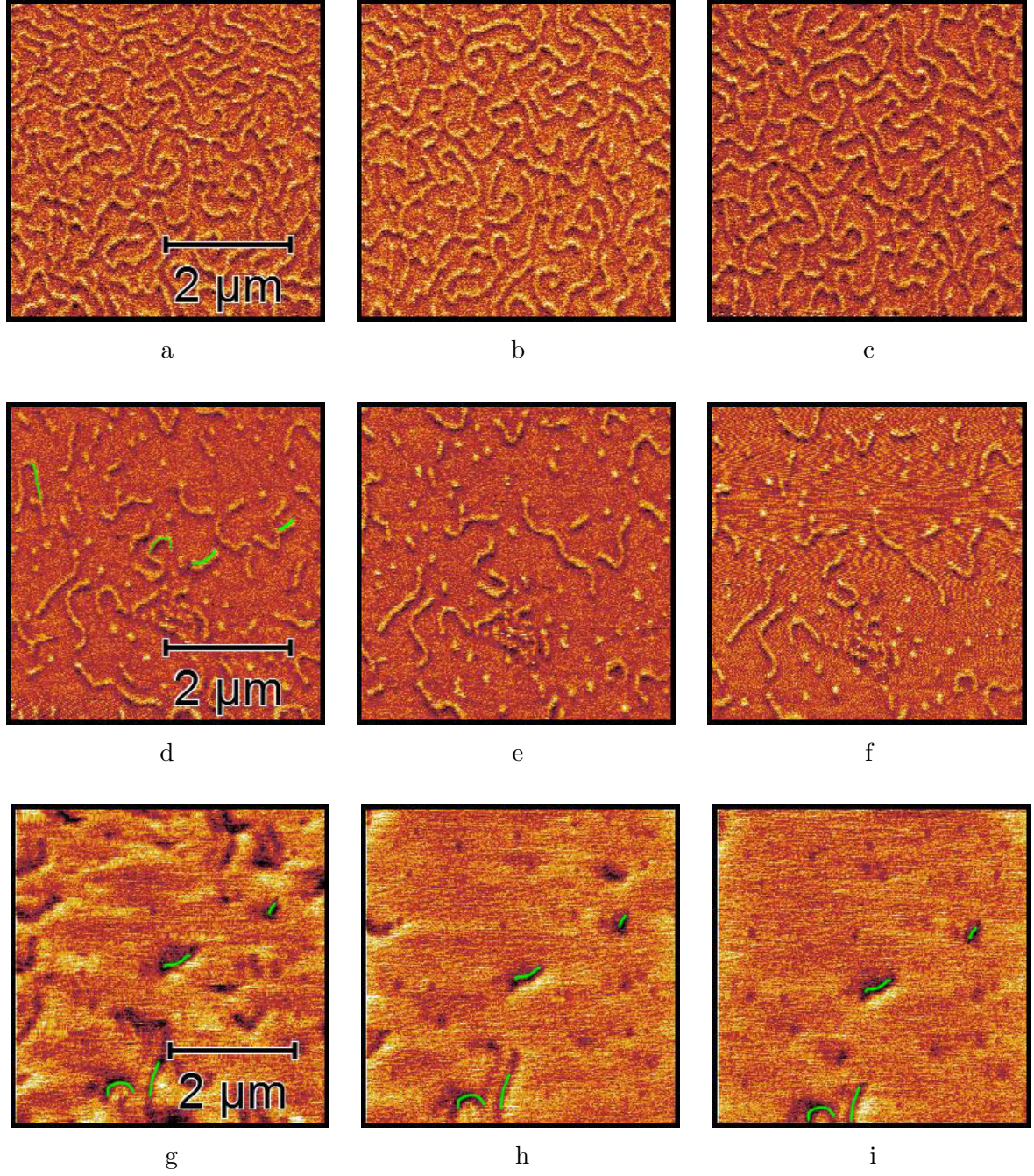
Figure 4.4: Each row of images represents three successive measurements on the same part of a sample, under the application of an OOP field of $\mu_0 H = 45\,\text{mT}$. Figures a-c are made with a $10\,\text{nm}$ Co-coating. Figures d-f are made with a $20\,\text{nm}$ coating. In figure d, the domains which are gone in figure e are marked in green. Figures g-i are made with $40\,\text{nm}$ Co-coating. The domains that remain throughout all three measurements are marked in green.

4.2.1 Quantifying the tips

So far, the 10 nm Co-tip was the most promising of the three tips that were tested: the signal-to-noise ratio is good and no domains are erased after performing multiple scans. However, it is not known what the sample's domain structure looks like before the first scan is made. It is still possible that some domains are erased when the first scan is being made. This is already visible between the first scan of the 10 and 20 nm tip in figures 4.4a and 4.4d. Just looking at 4.4d might give the impression that no interaction is present since no cut offs of the domains are visible but scanning that same sample with a 10 nm tip shows that a lot of domains have been erased already in figure 4.4d. To check whether the 10 nm tip yields reliable scans, the scans are compared with a SQUID-VSM measurement. This is done by determining the relative magnetization from a scan and comparing this to the relative magnetization according to a SQUID-VSM measurement. If the tip does not induce switching in the magnetization, M_{rel} determined from an MFM scan should be the same as M_{rel} determined from the SQUID-VSM measurement.

The relative magnetization is determined from the MFM-scans by 'counting' the up and down domains in the scans. This is done by fitting the histogram of the scan with the two term Gaussian function

$$f(\phi) = a_1 \exp[-(\frac{\phi - b1}{c_1})^2] + a_2 \exp[-(\frac{\phi - b_2}{c_2})^2]. \tag{4.1}$$

The products $a_1 c_1$ and $a_2 c_2$ are a measure for the amount of up and down domains which are used to determine the relative magnetization as

$$M_{rel} = \frac{M}{M_s} \propto \frac{a_1 c_1}{a_1 c_1 + a_2 c_2}, \tag{4.2}$$

with M_{rel} the relative magnetization, M the absolute magnetization and M_s the saturation magnetization. An example of an MFM-scan with the accompanying fit is shown in figures 4.5a and 4.5b. From this fit we find $M_{rel} = 0.19 \pm 0.06$.

M_{rel} is determined at different field strengths, starting from saturation at negative field and stepwise moving towards positive saturation. This is then compared with the SQUID-VSM measurement as is shown in figure 4.6: in blue, M_{rel} as determined by the SQUID-VSM is plotted and M_{rel} determined from the MFM scans in red. Good agreement between these two methods is found.

To check whether fitting the histogram is a reliable analysis for verifying the 10 nm tip its reliability, the same analysis is performed on scans made with the 20 nm tip. This is also shown in figure 4.6 as the yellow data points. Tips with a 20 nm layer of Co still yield values for M_{rel} that agree well with the SQUID-VSM measurement. At high field, the error is even lower than in the 10 nm data points. From this figure it is therefore concluded that this analysis cannot be used to verify a tip's reliability: it has been shown earlier
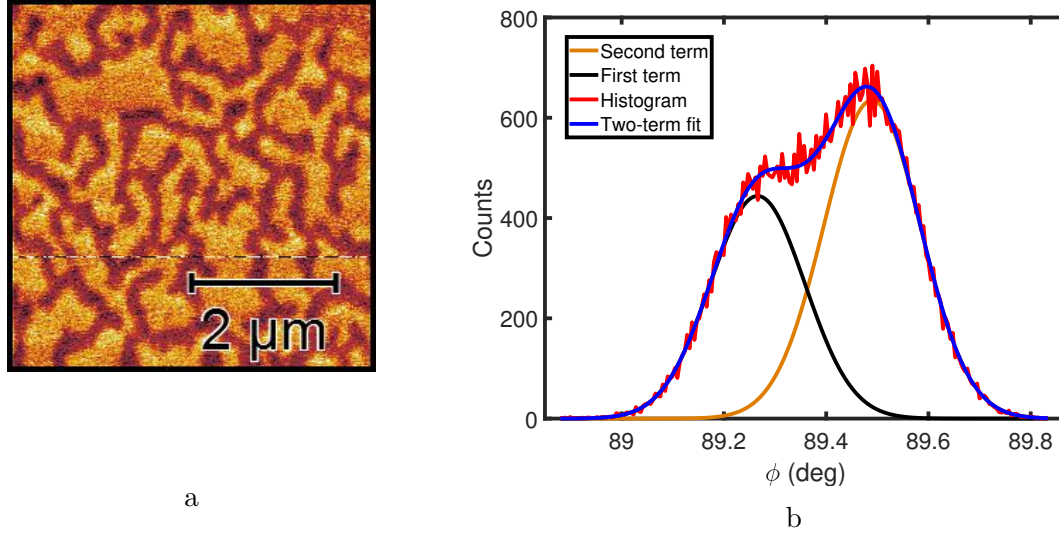
a

b

Figure 4.5: a: MFM-scan from which M_{rel} is determined. b: Histogram of the MFM with the double Gaussian fit (equation 4.1).

that domains are erased with the 20 nm Co-tip but this effect is not observed in figure 4.6. Also, a difference in M_{rel} was expected just by looking at the scans in figure 4.4: a lot less domains are present in the scans made with the 20 nm tip but this is not found by fitting the histogram. The reason for this analysis to fail is not understood but most probably lies in the fitting procedure. Although a low error is found in most of the data in figure 4.6, the extracted M_{rel} does not match what is expected from the scans.

Because it was not possible to quantify the 10 nm Co-tip's reliability by means of fitting the histogram, a visual inspection of the scans remains required. But since no switching of domains is observed in the scans made with these tips and the signal-to-noise ratio is good too, it is concluded that the 10 nm Co-tips can be used for this thesis. However, as is explained in the appendix, it turns out to be necessary to cap the Ta(2)/Co(10) layers with an additional Ta layer. Since this reduces the oxidation of Co, less Co is needed and the final structure that is used throughout this thesis is Ta(2)/Co(7.5)/Ta(4).

To summarize this chapter, we have found an easy method to fabricate usable MFM tips in our own system by sputtering Ta/Co/Ta on AFM tips. Several thicknesses of Co have been tried and it is found that a thickness of 7.5 nm results in a good signal-to-noise ratio. It is tried to confirm that no interaction is present when using the 7.5 nm-tip by comparing it with a SQUID-VSM measurement. Good agreement is found between the two but this is also found when comparing the SQUID-VSM measurement with a scan made with the 20 nm-tip, a tip which shows a lot of interaction. No definite conclusion could be drawn from this analysis but throughout the measurement with the 7.5 nm-tip, no interaction between tip and sample was observed. However, visual inspection remains necessary when

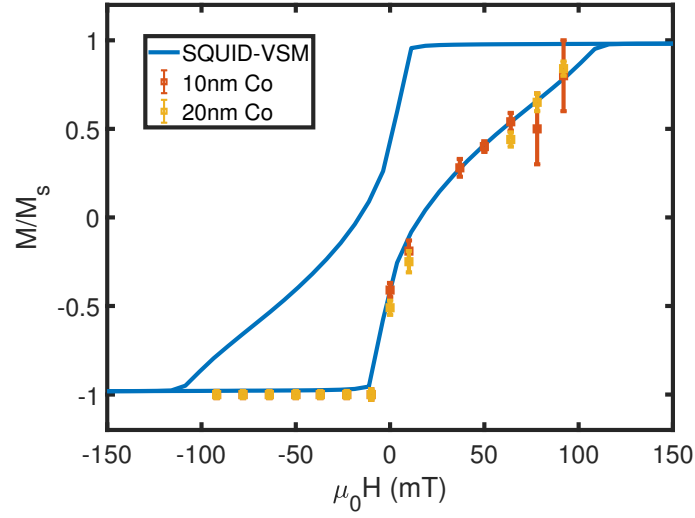Figure 4.6: M_{rel} determined with the SQUID-VSM, the 10 nm tip and the 20 nm tip.

using these tips. It is an important result that tips could be produced which do not show any perturbation of the magnetic domain state of the sample. Examples of scans that show interaction between tip and sample can be found in literature [39, 40, 41] and care should be taken when interpreting such results.

Chapter 5

Characterizing the multilayers

In this chapter, we characterize $[\mathrm{Ir}(1)/\mathrm{Co}(t_{\mathrm{Co}})/\mathrm{Pt}(1)]_{15\times}$ systems, where the Co thickness, t_{Co}, ranges from $0.5\,\mathrm{nm}$ to $1.1\,\mathrm{nm}$. The main goal of characterizing these systems is to determine how the interface interactions behave as a function of t_{Co} with respect to volume interactions. The interfacial interaction result from the Ir/Co and Co/Pt interfaces and are therefore expected to be inversely proportional to t_{Co}. Since a technique to directly determine one of the interface interactions, the DMI, is not available, D is related to the domain wall energy (σ), M_{s} and K.

This chapter discusses first how M_{s} and K are determined and how they change as a function of t_{Co}. Next, σ is determined with the help of two domain spacing models as discussed in sections 2.2.1 and 2.2.2. Finally, we determine D as a function of t_{Co} and discuss its behavior.

5.1   Saturation Magnetization

The saturation magnetization, M_{s}, of a magnetic material is defined as

$$M_{\mathrm{s}} = \frac{m_{\mathrm{s}}}{V_{\mathrm{mag}}}, \tag{5.1}$$

with m_{s} the magnetic moment at saturation and V_{mag} the magnetically active volume. It is important to make a distinction between magnetically active volume and the deposited magnetic volume. When different layers are sputtered, intermixing takes place. The intermixing of Co-atoms with non-magnetic materials can deplete their ferromagnetic properties, leading to a reduction in magnetization [42]. This effect takes place for a limited amount of Co layers and the region is referred to as the magnetic dead layer (MDL). Because the characterized samples consist of ultra-thin layers, the MDL will be relevant but can be corrected for. To see how it can be corrected for, equation 5.1 is rewritten as

$$\frac{m_{\mathrm{s}}}{\mathcal{A}} = M_{\mathrm{s}}(t_{\mathrm{dep}} - t_{\mathrm{dead}}), \tag{5.2}$$
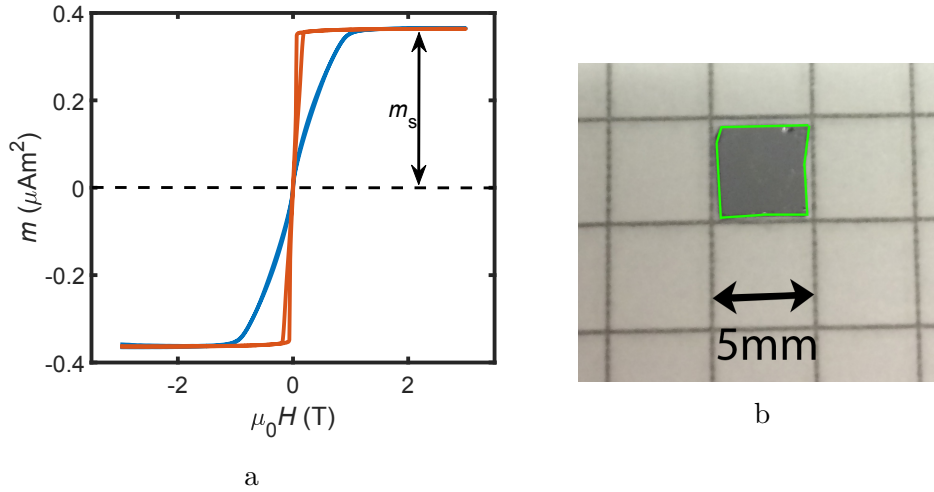
Figure 5.1: a: SQUID-VSM measurement of the IP (blue) and OOP (red) component of the magnetization, plotted as a function of applied field for a $[\text{Ir}(1)/\text{Co}(0.6)/\text{Pt}(1)]_{15\times}$ sample. For the IP measurement, the field is applied in the plane of the sample wheras it is applied perpendicular to the plane for the OOP measurement. b: Picture of the sample on graph paper. The squares on the graph paper are $5\,\mu\text{m} \times 5\,\mu\text{m}$. By counting the pixels in the area enclosed by the green lines, the sample's area can be determined.

with $\mathcal{A}$ the area of the sample, t_{dep} the thickness of the sputtered material and t_{dead} the thickness of the MDL. The parameters m_{s} and $\mathcal{A}$ can be measured and t_{dep} is known. By plotting $\frac{m_{\text{s}}}{\mathcal{A}}$ as a function of t_{dep}, t_{dead} can be determined from the intercept where $\frac{m_{\text{s}}}{\mathcal{A}} = 0$.

To determine m_{s}, an IP and OOP SQUID-VSM measurement is performed on the samples, a typical measurement is shown in figure 5.1a. The IP (blue) and OOP (red) components of the magnetization are plotted as a function of the applied magnetic field. The m_{s} is calculated by averaging $m_{\text{s,IP}}$ and $m_{\text{s,OOP}}$. Although $m_{\text{s,IP}}$ and $m_{\text{s,OOP}}$ in figure 5.1a are equal, these differ in other measurements due to a measurement artifact in the setup [43]. How $\mathcal{A}$ is determined is shown in figure 5.1b where the sample is shown on a sheet of graph paper. By counting the pixels in the green outline, the area of the sample can be determined because the size of a square on the graph paper is known to be $5\,\text{mm} \times 5\,\text{mm}$.

After determining m_{s} and $\mathcal{A}$ for all the samples, figure 5.2a is obtained. A plot of $\frac{m_{\text{s}}}{\mathcal{A}}$ $(= M_{\text{s}}(t_{\text{dep}} - t_{\text{dead}}))$ versus t_{dep} is shown with a linear fit to determine t_{dead} according to equation 5.2. The error in the data points both results from disagreement between $m_{\text{s,IP}}$ and $m_{\text{s,OOP}}$, as well as an error in $\mathcal{A}$, which is determined from averaging the area over three measurements. From this plot it is found that the MDL has a thickness of $t_{\text{dead}} = (0.24 \pm 0.06)\,\text{nm}$ by fitting the data which is shown as the red solid line.

A significant MDL is found which is ascribed to intermixing in the Ir/Co/Pt-layers. Other studies show no alloying of Pt deposited on Co [44, 45, 46] which suggests that Co inter-
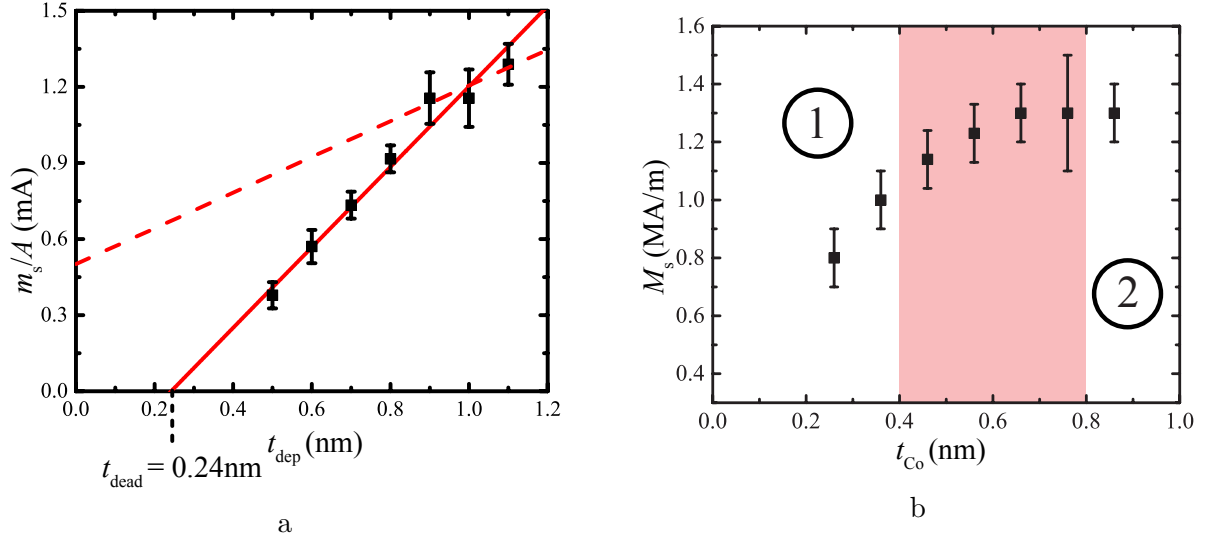
Figure 5.2: a: $\frac{m_s}{A}$ is plotted as a function of the deposited Co thickness, t_{dep}, from which t_{dead} is extracted using a linear fit according to equation 5.2. A linear fit through the last three data points is shown as the red dashed line. b: M_s is plotted as a function of the corrected layer thickness, t_{Co}. At large t_{Co}, M_s converges to $(1.3 \pm 0.1)\,\mathrm{MA\,m^{-1}}$. Two regions are indicated in the figure which are separated at $t_{Co} = (0.6 \pm 0.2)\,\mathrm{nm}$. In region 2, the bulk M_s is reached.

mixes with Ir. However, in [46], no MDL in an [Ir(1.6)/Co(x)/Pt(3)]-system was found following the same method as presented here with x ranging from 0.6 nm to 6 nm. In contrast to us, they did not use their full range of Co thicknesses for determining M_s. Only from $t_{Co} = 1.1$ nm did they consider their data points to be reliable. They argue that below this thickness, effects like island formation and a change in Curie temperature skew the data. This might be the case for our samples too, as will turn out in the subsection on the anisotropy. More data points for thicker t_{Co} would be needed to confirm whether this is happening or not. Another phenomenon that is known to take place in Ir/Co/Pt systems is proximity induced magnetization (PIM) [47, 48], which means that Co magnetizes the adjacent Ir and Pt. This raises the magnetic moment measured by the SQUID-VSM and thus lowers the determined MDL. It is not determined what fraction of the measured m_s should be ascribed to the magnetized Ir and Pt but the actual MDL will be larger than what is determined from equation 5.2. From here on, the magnetic active layer ($t_{dep} - t_{dead}$) will be referred to as t_{Co}.

With the dead layer known, M_s can be determined with equation 5.1, which is plotted in figure 5.2b. For increasing t_{Co} in region 1, an increase of M_s is found. The increase eventually stagnates and M_s approaches $(1.3 \pm 0.1)\,\mathrm{MA\,m^{-1}}$ in region 2 (determined from averaging the last three data points) which matches the generally accepted M_s of $1.4\,\mathrm{MA\,m^{-1}}$ for Co [20, 44]. There are two regions indicated in the figure, region 1 is for the range of t_{Co} where

M_s shows an increasing trend and region 2 where the increase in M_s has stagnated. The transition from region 1 to region 2 is determined to be at $t_\mathrm{Co} = (0.6 \pm 0.2)\,\mathrm{nm}$ (how this is determined is discussed in the next section). The deviation of M_s in region 1 to bulk M_s suggests that effects like island formation and a lowering of the Curie temperature also play a role in our samples which is overcome in region 2. If the MDL is determined by only fitting the last three data points, shown as the red dashed line, an MDL of $(-0.7 \pm 0.7)\,\mathrm{nm}$ is found. According to this fit the MDL is negative which is unphysical and ascribed to PIM in the sample but also to the little amount of data points in region 2. However, it's possible that a lower, or no MDL at all will be found if samples with a larger t_dep are used in this analysis, like Gabor et al. [46] did.

PIM and deviation of the data points in region 1 skews the analysis based on equation 5.2 presented in figure 5.2a and with that the t_dead that is determined from the fit. More data points at larger t_Co are needed to investigate the influence of region 1 on the MDL. For the further analysis, the extracted MDL of $0.24\,\mathrm{nm}$ is used. At the end of this chapter will be discussed what the effect of a lower MDL on the DMI is. A lower MDL will result in a lower M_s and thus a lower K, as discussed in section 2.3.1. This will lower D as can be seen in equation 2.1.

5.2 Determining the anisotropy

Now that M_s is known, K can be characterized. The method as discussed in subsection 2.3.1 is used, where K is determined as displayed in figure 2.15 by calculating the area between an IP and OOP SQUID-VSM. Kt_Co is plotted, as discussed in section 2.1.2, in figure 5.3. Here, the error in the data mostly results from the error in calculating the magnetic volume (so determining $\mathcal{A}$). Again two regions, '1' and '2', are indicated which correspond to the same ranges of t_Co in figure 5.2b. An increasing trend of Kt_Co is observed in region 1 after which it decreases in region 2. In region 1, the data is fitted with equation 2.9, describing a coherent region and in region 2 the data is fitted with equation 2.10, which describes an incoherent region. This is indicated with the red curves. The intercept of these fits is used to determine that at $t_\mathrm{Co} = (0.6 \pm 0.2)\,\mathrm{nm}$, the transition from region 1 to region 2 takes place. Extrapolating the fit in region 2 results in a thickness of $t_\mathrm{Co} = (1.4 \pm 0.2)\,\mathrm{nm}$ at which the anisotropy switches from OOP to IP.

Next, Kt_Co is plotted but with K_shape $(= \frac{1}{2}\mu_0 M_\mathrm{s}^2$, as discussed in section 2.1.2) taken into account, so

$$\tilde{K}t_\mathrm{Co} \equiv (K + \frac{1}{2}\mu_0 M_\mathrm{s}^2)t_\mathrm{Co} = K_\mathrm{v}t_\mathrm{Co} + K_\mathrm{s}, \tag{5.3}$$

with K_v the volume contributions (besides K_shape) and K_s the surface contributions to the anisotropy. This results in figure 5.4. Again, two regions are indicated with '1' and '2', which correspond to the same indicated in figure 5.3. In region 1, a linear increase of the anisotropy is present which flattens in region 2.
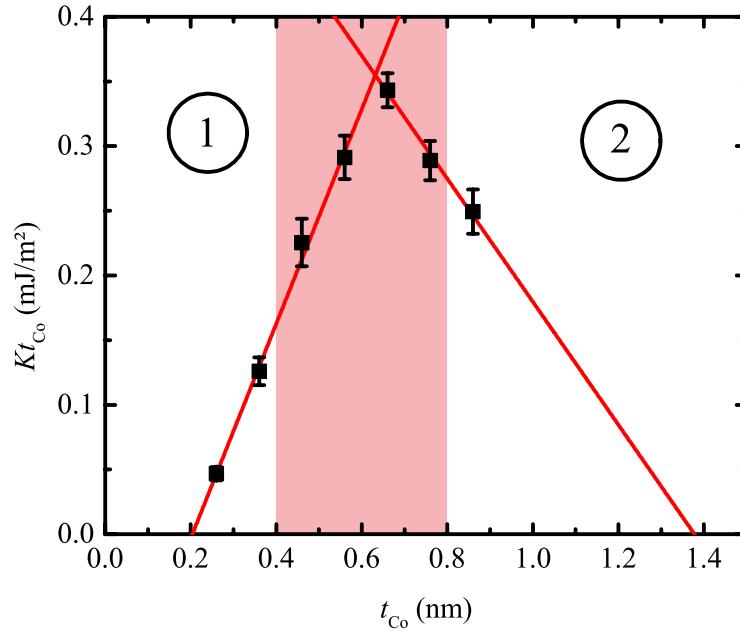
Figure 5.3: Kt_{Co} as a function of t_{Co}, measured for multilayers consisting of $[\text{Ir}(1)/\text{Co}(t_{dep})/\text{Pt}(1)]_{15\times}$. Two regions, 1 and 2, are indicated in which Kt_{Co} shows an increasing and decreasing trend respectively. At $t_{Co} = (0.6 \pm 0.2)\,\text{nm}$, the transition from region 1 to region 2 is indicated in red. This is extracted from the intercept of the linear fits in both regions. Extrapolating the fit in region 2 gives $t_{Co} = (1.4 \pm 0.2)\,\text{nm}$ at which Kt_{Co} becomes negative.

Figure 5.4: $\tilde{K}t_{Co}$ is plotted as a function of t_{Co}. Two regions, 1 and 2, can be identified between which the increase of $\tilde{K}$ differs. From fitting region 1 (dotted red line) and region 2 (solid red line), K_N and K_s are determined from the intercepts and K_{me}^{coh} and K_v from the slopes of the regions 1 an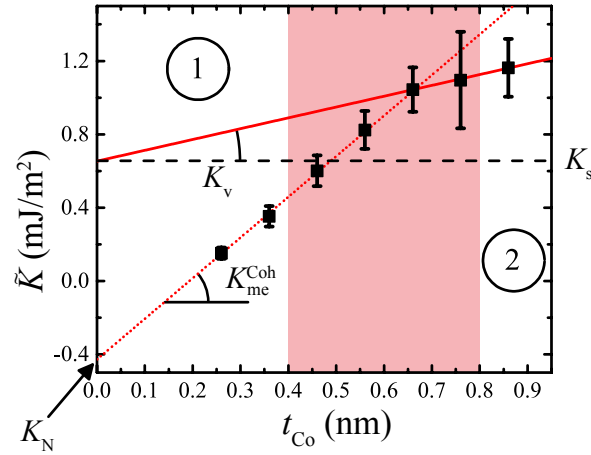d 2 respectively. A transition from region 1 to region 2 exists at $t_{Co} = (0.6 \pm 0.2)$ nm which is indicated in red.

The presence of two regions is not expected when solely looking at equation 5.3, which predicts a single K_v throughout the range of t_{Co}. Only the behavior as indicated by the solid red line, which is a fit of equation 5.3, through the data points in region 2, is predicted by equation 5.3, since this results in a positive K_s. However, different behavior is found in region 1, as indicated with the dotted red line which is a fit through the data points in region 1. To explain what causes the difference between region 1 and 2, one can look back at figure 5.3 and conclude that the increase in region 1 is a result of the sample being in the coherent region, as discussed in 2.1.2. For region 1, equation 5.3 would then take the form of

$$\tilde{K} = K_{me}^{coh}t_{Co} + K_N, \tag{5.4}$$

in line with equation 2.9. Fitting region 1 in figure 5.4, however, results in $K_N < 0$, meaning that the magnetocrystalline anisotropy induced by the interfaces in the Ir/Co/Pt stack promotes an IP anisotropy. For the Co/Pt interface, the consensus is that the K_N is high and positive (this was already shown by Den Broeder et al. in 1991 [49] and confirmed numerous times since then). A positive K_N is also found by, e.g., [49, 50] for a Co/Ir interface. It is therefore unlikely that K_N is negative in the characterized samples.

What is expected to be taking place in region 1 is that the quality of the interfaces increases as Co-thickness increases. This is schematically pictured in figure 5.5 where three Ir/Co/Pt multilayers (A, B and C) are shown with Co thickness increasing from A to C. In A, Co has been deposited but not enough to fully cover the area. This results in island
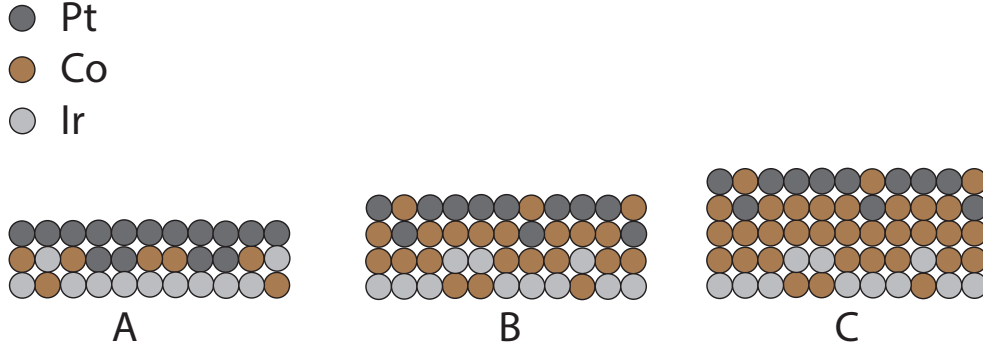
Figure 5.5: Three different (A, B and C) scenarios are depicted for growing Ir/Co/Pt multilayers. In A, the Co layer is too thin to form a full layers so islands of Co are present. In B, sufficient Co is deposited to fully cover the sample but intermixing with Ir and Pt is present. Increasing the Co thickness as shown in C still results in intermixing with Ir and Pt as shown in B but a larger magnetic volume is present. A corresponds to region 1, B to the transition from region 1 to region 2 and C to region 2.

formation and, together with intermixing, in rough interfaces, demoting K_N. In multilayer B, enough Co has been deposited to fully cover the Ir so the interfaces are fully developed. However, intermixing between Co, Ir and Pt still takes place. In C the Co is thick enough to have fully developed interfaces so depositing more Co will only result in a larger K_{shape}. Situation A corresponds to region 1, B to the transition from region 1 to region 2 and C to region 2. The effects discussed in figure 5.5 are expected to cause the difference between M_s in region 1 and 2 in figure 5.2b too. Island formation lowers the Curie temperature of Co and with that its magnetic moment [46].

Based on the analysis, the fit through region 2 is used in order to find the surface anisotropy K_s. Note that this is not K_N: although K_{me}^{coh} is not extracted from the slope in region 1 in figure 5.4, it is still possible there is a contribution of K_{me}^{incoh} to K_s. We find $K_s = (0.65 \pm 0.03)\,\mathrm{mJ\,m^{-2}}$.

It is hard to conclude how much the Ir/Co and Co/Pt interfaces contribute to K_s. Den Broeder et al [49] found that K_s resulting from a Ir/Co interface ($\approx 0.8\,\mathrm{mJ\,m^{-2}}$) is higher than from a Pt/Co interface ($\approx 0.5\,\mathrm{mJ\,m^{-2}}$), in line with Kim et al. who found $K_s = 1.36\,\mathrm{mJ\,m^{-2}}$ [47] for Ir/Co and for Pt/Co Cho et al. reports $0.54\,\mathrm{mJ\,m^{-2}}$ in [51] and Kim et al. $1.1\,\mathrm{mJ\,m^{-2}}$ in [52]. Determining to what extent each interface contributes to the total cannot be done from this data but it is likely that, based on literature, the Ir/Co interface contributes the most.

K_s is low compared to the reported values above which result from a single interface, whereas the investigated stack has two interfaces that contribute to the total K_s. However, for a Co/Pt interface, a large range of K_s is reported, which is caused by a strong

influence of the substrate and buffer layer [22]. Assuming this also applies to the Ir/Co interface could explain why the K_s found in these systems does not agree with the values reported above. Another effect that could explain the lower K_s results from growing 15 repeats on top of each other. As a material is deposited, the layer is not perfectly smooth but has some variations in height. These variations transfer to the layers grown on top due to which the top repeats will have less smooth Ir/Co/Pt interfaces than the lower repeats. This will also reduce K_s.

Determining K_v is done by calculating the slope of region 2 in figure 5.4, resulting in $K_v = (0.2 \pm 0.1) \, \mathrm{MJ \, m^{-3}}$. It is hard to compare K_v with literature: most papers do not consider a volume anisotropy besides K_{shape}. For large Co thicknesses ($\approx$50 nm) it is reported by [53] that K_v for fcc Co is $0.02 \, \mathrm{MJ \, m^{-3}}$ and for bcc Co $0.5 \, \mathrm{MJ \, m^{-3}}$, suggesting that a mixture is present in our samples. However, it is hard to draw definite conclusion about this without more information on the crystal structure.

5.3   Domain wall energy and DMI

The last parameter that is necessary to determine D with equation 2.1 is the domain wall energy, σ. Two models have been discussed in sections 2.2.1 and 2.2.2 which are used to calculate the domain wall energy from MFM scans: the model by Draaisma and De Jonge and the terminal domain width model. In this section, the steps that are taken to determine σ as well as the obtained σ are discussed. First the results obtained by the model of Draaisma and De Jonge are discussed and then the results obtained with the terminal domain width model.

After σ is calculated from both models, D is determined following equation 2.1. The only parameter that is not measured is A which is very hard to measure for magnetic thin films. This is why in this thesis A is assumed to be $10 \, \mathrm{pJ \, m^{-1}}$, in agreement with Woo et al. [10] who investigated a comparable magnetic system. However, it is known that A changes as a function of Co thickness [54]. How big the effect of varying A on D is will be discussed too.

For the $[\mathrm{Ir}(1)/\mathrm{Co}(t_{\mathrm{Co}})/\mathrm{Pt}(1)]_{15\times}$ systems, where the Co thickness, t_{Co}, ranges from 0.5 nm to 1.1 nm, the sample with $t_{\mathrm{dep}} = 0.5$ nm is not characterized in this section: it was found that the MFM-signal from that sample is too low to determine d or d_{min}. For $t_{\mathrm{dep}} = 1.0$ nm and 1.1 nm it was not possible to follow the measurement procedure which is described in this section: the available magnet was not strong enough to saturate the sample which leads to data that cannot be compared with the rest. These Co thicknesses are therefore not characterized either.

5.3.1 Draaisma and De Jonge

The model by Draaisma and De Jonge determines σ from d. How d is determined is shown in figure 5.6. An MFM scan (5.6a) of an $[\text{Ir}(1)/\text{Co}(0.7)/\text{Pt}(1)]_{15\times}$-system at $\mu_0 H = 24\,\text{mT}$ is binarized (5.6b). A 2D fourier transform is then calculated which is plotted in figure 5.6c. Here, also a black circle is shown which is used to check how well the periodicity (d) in figure 5.6d is determined. After switching to polar coordinates in figure c with $|k| = 0$ at $k_x = k_y = 0$, $|k| = \sqrt{k_x^2 + k_y^2}$ is averaged over θ which is plotted in figure d. This is fitted (orange curve) and the peak ($d = (420 \pm 20)\,\text{nm}$) is indicated with the black vertical line. The error in d results from the error in the fit.

A problematic aspect of our analysis is that the samples show hysteretic behavior which makes it hard to determine whether the system is in its energetic ground state. We attempt to circumvent this problem by saturating the sample at negative field first. Next, the field is increased to be positive and with the MFM is checked whether a domain structure is obtained which shows a constant d throughout the scanned area. Figure 5.6a is an example of such a scan.

An average d and σ are determined for various t_{Co} which are plotted in figures 5.7a and 5.7b respectively. d shows no trend but fluctuates around approximately 450 nm and σ increases as t_{Co} increases. A constant d for increasing t_{Co} is not expected according to the model by Draaisma and De Jonge (see section 2.2.1). Increasing t_{Co} means increasing the dipolar energy which was explained to result in a lower d. When the dipolar energy increases, this is also expected to lower σ. However, in figure 5.7b an increase in σ is shown. The increase in σ is attributed to the increase in K, which is known from figure 5.3 to be present for these Co thicknesses, resulting in an increasing σ.

5.3.2 Terminal domain width

Next, the terminal domain width model is used to determine σ. In order to use this analysis, the sample is saturated at negative field and stepwise brought to saturation at positive field. At each step, an MFM-scan is made like shown in figures 5.8a to 5.8c, which shows the results for an $[\text{Ir}(1)/\text{Co}(0.6)/\text{Pt}(1)]_{\times 15}$ sample. At each scan, the width of the dark domains is measured by hand at 15 locations and averaged. The error in the data points results from averaging the domain width at each scan over 15 measurements. The domain width as function of applied field is displayed in figure 5.8: as the field increases, the domain width decreases until it reaches its terminal width of $d_{\text{min}} \approx 97\,\text{nm}$. Increasing the field beyond this range saturates the sample. From the terminal domain width that is determined with this plot, σ is determined with the help of equation 2.13.

Only for the sample with $t_{\text{dep}} = 0.6\,\text{nm}$, it was possible to confirm from the scan that
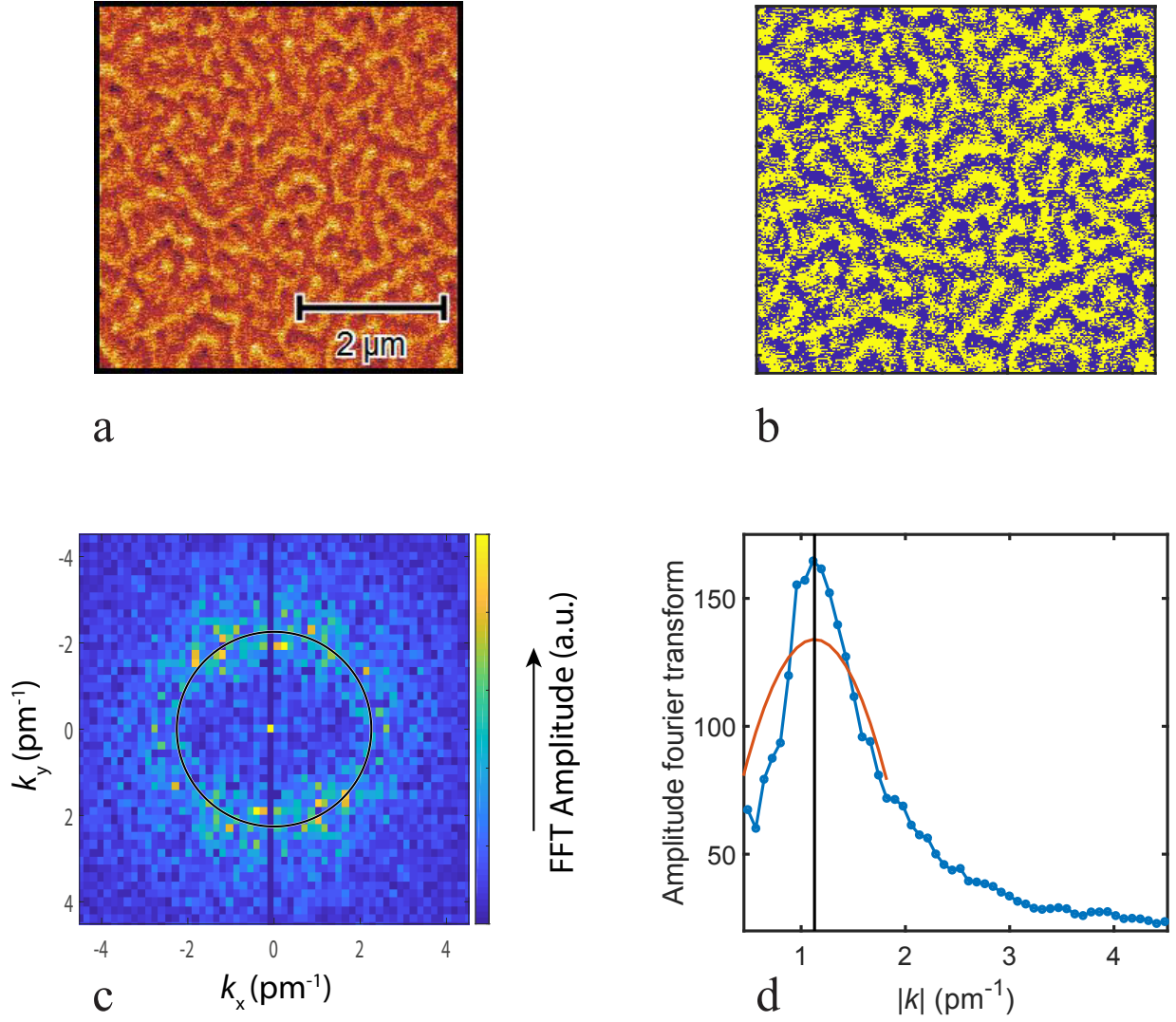
Figure 5.6: a. MFM scan for a $[Ir(1)/Co(0.7)/Pt(1)]_{15\times}$ sample under the application of an OOP field of $24\,mT$. b. Binarized MFM scan, yellow corresponds to $+m_s$ and blue to $-m_s$. c. 2D fourier transfrom of the binarized image in b. The circle results from the fit in d and is used to check the fit quality. d. Angular average of c from which the peak (indicated by the black vertical line) is determined by a quadratic fit (indicated with the red curve).

Figure 5.7: a: d as a function of t_{Co}. b: σ as a function of t_{Co} determined with the model by Draaisma and De Jonge based on the data from a.
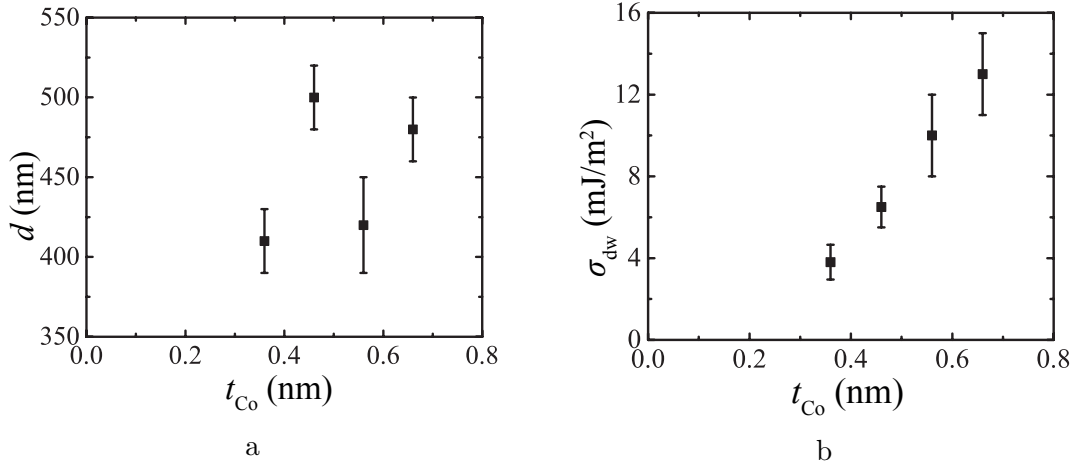
saturation was reached at the highest applied field. For the other Co thicknesses, domains were still present at this field strength. However, since a gradual approach to $d_{\min}$ is found in these samples too, this asymptote is assumed to be the terminal domain width.

With the method described above and equation 2.13, σ calculated from $d_{\min}$ is plotted in figure 5.9, together with σ calculated from the model by Draaisma and De Jonge. Again, an increase in σ is found whereas an increase in dipolar energy is introduced which is ascribed to the strong increase in K in this range of t_{Co}. For the first 2 points, the two methods show good correspondence but the data diverges at the last 2 points. The terminal domain width then results in lower σ than the model by Draaisma and De Jonge.

5.3.3 DMI as a function of Co thickness

From σ, it is possible to calculate $|D|$ with equation 2.1 since K is measured and A is assumed from literature. $|D|$, calculated with σ from both the models, is plotted in figure 5.10a, with the region below $|D| = 0\,\mathrm{mJ\,m^{-2}}$ shaded to indicate the unphysical region in this graph. For both models, $|D|$ decreases as t_{Co} increases. However, $|D_{\mathrm{Draaisma}}|$ is negative for the last two data points, which is unphysical. This probably results from a flawed measurement technique to determine σ. As mentioned before, it is not possible to check whether the system is in its energetic minimum and the samples probably were not when the data in figure 5.7b was obtained, concluding from the negative $|D_{\mathrm{Draaisma}}|$.

Although $|D_{\mathrm{Terminal}}|$ is positive for all data in the figure, the last data point where $|D| = (0.1 \pm 0.8)\,\mathrm{mJ\,m^{-2}}$ is very low and almost negative, making it hard to conclude whether the terminal domain width model does result in reliable data. $|D_{\mathrm{Terminal}}|$ found by this
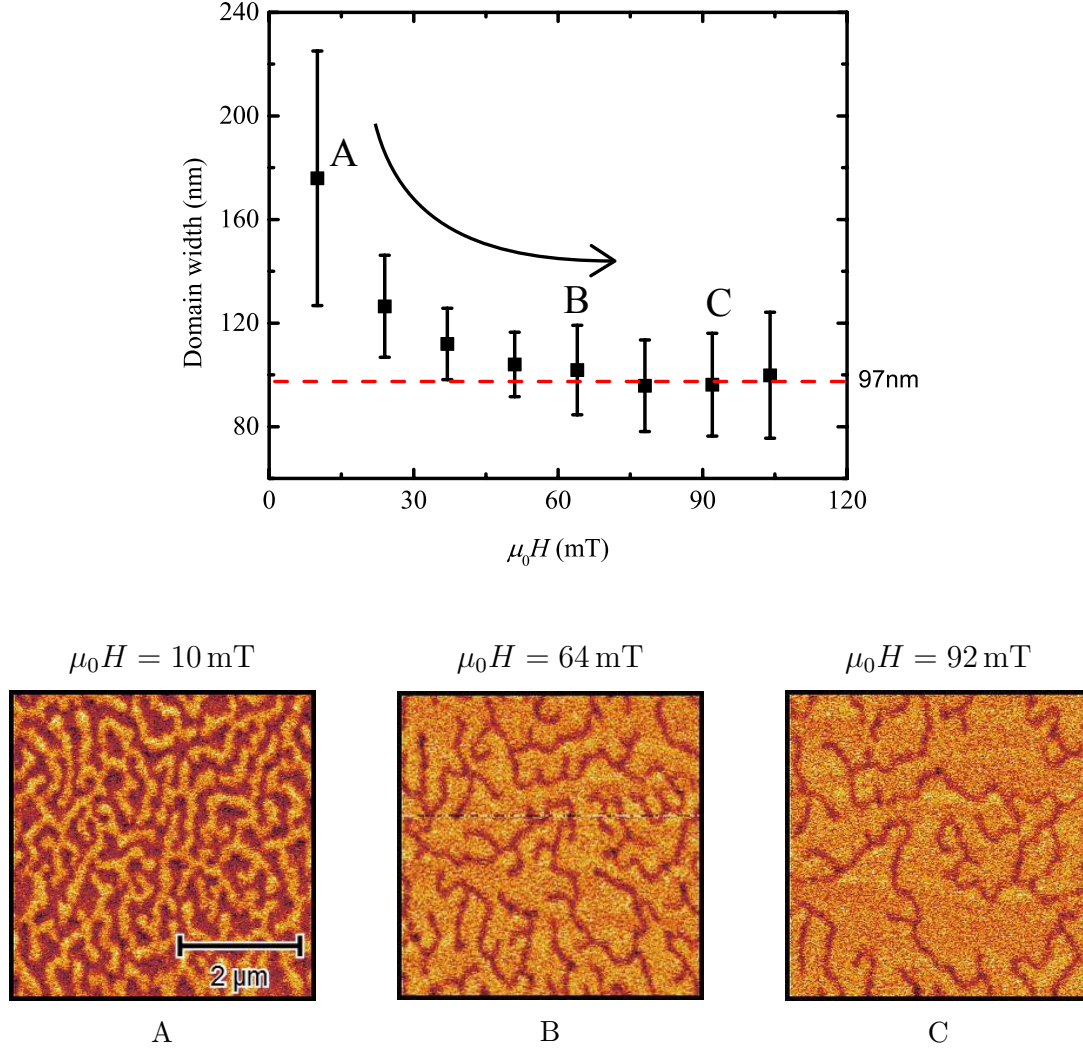
Figure 5.8: In the graph is plotted how the domain width decreases as a function of the magnetic field strength. The domain width asymptotically approaches $d_{\min} = 97\,\mathrm{nm}$ before saturation. Points A, B and C correspond to the scans shown above the graph from which the domain width is determined.

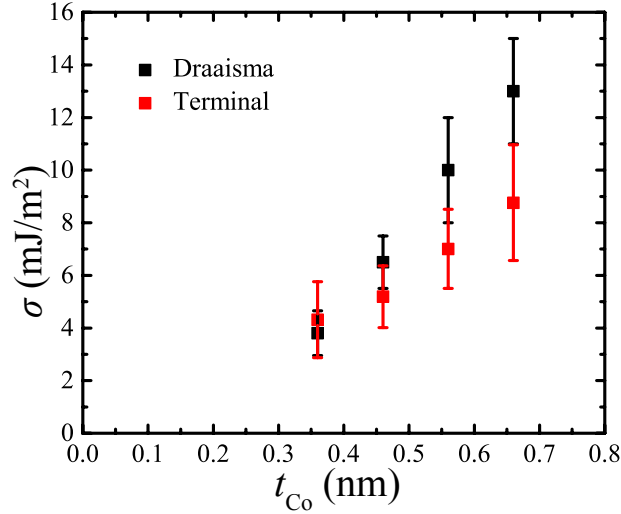Figure 5.9: σ calculated from the model by Draaisma and De Jonge and terminal domain width model as a function of t_{Co}.

model for the lowest Co thickness ($(1.0 \pm 0.3)\,\mathrm{mJ\,m^{-2}}$) is lower than what Moreau Luchaire et al. [26] found $|D| = (1.6 \pm 0.2)\,\mathrm{mJ\,m^{-2}}$ in $[\mathrm{Pt/Co(0.6)/Ir}]_{10x}$. Lucassen et al. [55] have found $|D| = (1.6 \pm 0.4)\,\mathrm{mJ\,m^{-2}}$ for a $[\mathrm{Pt/Co(0.9)/Ir}]_{15x}$ system whereas we found that $|D_{\mathrm{Terminal}}| = (0.1 \pm 0.8)\,\mathrm{mJ\,m^{-2}}$, which could be due to a different A that is assumed (Lucassen assumes an A of $16\,\mathrm{pJ\,m^{-1}}$). Using the same A as Lucassen, changes our $|D_{\mathrm{Terminal}}|$ from $(0.1 \pm 0.8)\,\mathrm{mJ\,m^{-2}}$ to $(0.9 \pm 0.8)\,\mathrm{mJ\,m^{-2}}$, which corresponds better to what they found. Also the stack characterized by Lucassen et al. is the inverse of what is characterized here (they characterized Pt/Co/Ir instead of our Ir/Co/Pt sample) which could result in different interface development and thus a different D. Another parameter that influences D is the MDL. In the section on M_s, an MDL of $0.24\,\mathrm{nm}$ is determined. Assuming an MDL of zero, as the fit through the last three data points suggested, results in a higher σ and a lower D. However, D that results from zero MDL lies within the error margin of D that is determined here.

It is hard to conclude whether an increasing or decreasing trend should be present in this region: a volume density ($|D_{\mathrm{Terminal}}|$) is expected to decrease as the volume (t_{Co}) increases but it is also known from K that the interfaces are still under development in this Co range. The increase in interface quality could be high enough to lift the downwards trend due to increasing t_{Co}.

To compensate for the increasing thickness, $|D_{\mathrm{Terminal}}|$ is multiplied by t_{Co} to obtain the surface DMI, D_s. This is plotted in figure 5.10b. A decrease in D_s is present which is, again, unexpected since the interfaces were concluded from the trend in K to increase in quality. A reason for the absence of an increasing trend could lie in the assumption that A is constant throughout all Co thicknesses whereas it has been shown by [54] that A
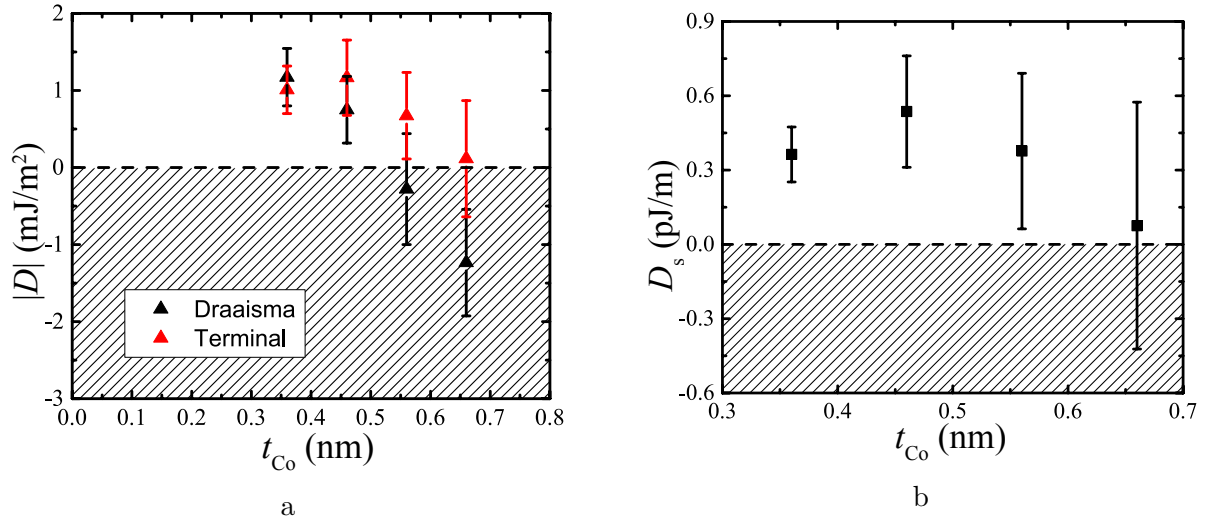
Figure 5.10: a: $|D_{\mathrm{Draaisma}}|$ and $|D_{\mathrm{Terminal}}|$ calculated from their respective models. The region below $|D| = 0\,\mathrm{mJ\,m^{-2}}$ is shaded to mark the region which is unphysical. b: D_{s} calculated for $|D_{\mathrm{Terminal}}|$. The unphysical region is again shaded.

increases with t_{Co}. As can be seen from equation 2.1, an increase in A with t_{Co} results in an increase in $|D_{\mathrm{Terminal}}|$ with t_{Co} (and for D_{s}).

From both analysis that have been discussed, the terminal domain width model is believed to give more reliable results than the model by Draaisma and De Jonge. This is because it is hard to find the energetic ground state of the system from which d can be determined since the system shows hysteresis. The method for determining the terminal domain width is believed to be less prone to that problem. This is also reflected in the results that have been found: a negative $|D|$ is found from the model by Draaisma and De Jonge.

A solution to overcome the problems with the model by Draaisma and De Jonge is to demagnetize the sample before determining d, as suggested by Moureau-Luchaire et al. [26]. It is believed that by applying an AC magnetic field which decreases in amplitude with every step, the energetic ground state of the sample can be reached.

An aspect of our analysis which could explain the decrease in D_{s} could result from an underlying assumption in equation 2.1: it is assumed that the domain wall is does not vary throughout the thickness of the layer. However, Legrand et al. [56] found from simulating a magnetic multilayer that the spin structure throughout the stack height does not have to be invariant, which is shown in figure 5.11. The cross-section of a $[\mathrm{X}(1)/\mathrm{Co}(0.8)/\mathrm{Z}(1)]_{20\times}$ magnetic multilayer (with X and Z dummy materials) is shown, which is comparable to our sample. Figures A-D correspond to $D = -1\,\mathrm{mJ\,m^{-2}}$, $0\,\mathrm{mJ\,m^{-2}}$, $1\,\mathrm{mJ\,m^{-2}}$ and $2\,\mathrm{mJ\,m^{-2}}$ respectively. It can be seen that in the vertical (z) direction, no constant magnetization is
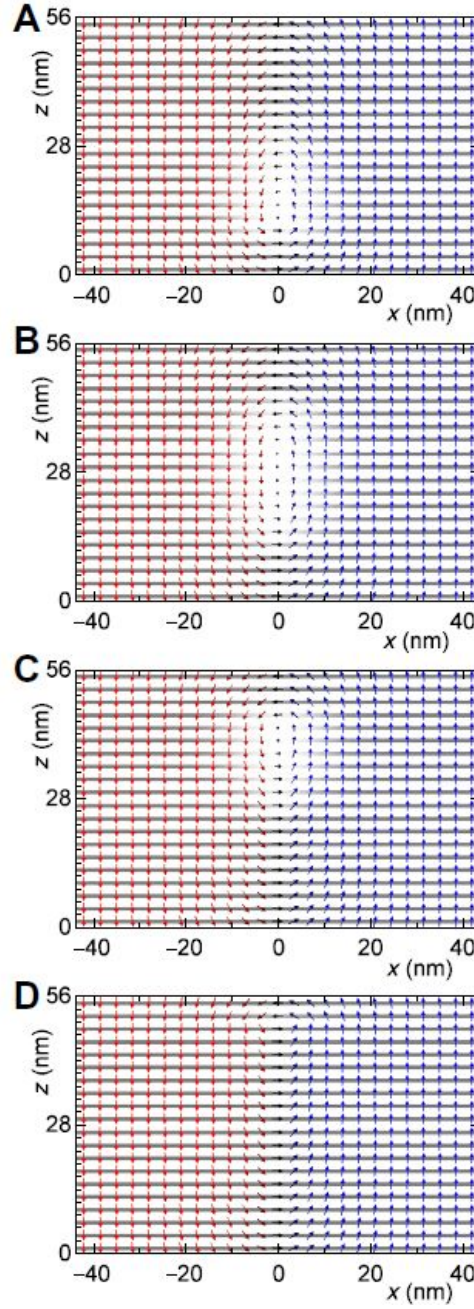
Figure 5.11: The cross-section of a $[X(1)/Co(0.8)/Z(1)]_{20\times}$ multilayer (with X and Z dummy materials) is plotted four times with the gray lines indicating the Co layers. A-D corresponds to $D = -1\,\mathrm{mJ\,m^{-2}}$, $0\,\mathrm{mJ\,m^{-2}}$, $1\,\mathrm{mJ\,m^{-2}}$ and $2\,\mathrm{mJ\,m^{-2}}$ respectively. The arrows indicate the magnetization with m_z indicated by red ($+m_s$) and blue ($-m_s$) and m_y by the grid color being black ($-m_s$) and white ($+m_s$). Picture adapted from [56].

present in any of the figures which is one of the main assumptions.

What might be problematic too is that, as Buettner describes it in [57], the domains spacing models make a crude approximation of the stray field interactions between domain walls. Buettner et al. have developed a model which takes these interactions into account more precisely.

To summarize this chapter: magnetic multilayer systems consisting of $\text{Ir}(1)/\text{Co}(x)/\text{Pt}(1)]_{15\text{x}}$ with x varying from 0.5 nm to 1.1 nm in steps of 0.1 nm have been characterized. For M_s and K, it is found that two regions can be identified in this range of Co thicknesses. Region 1, where the interfaces are still under development, transitions to region 2 at $t_\text{Co} = (0.6 \pm 0.2)\,\text{MA m}^{-1}$ where the interfaces have fully developed. Both parameters show an increasing trend in region 1 but in region 2, M_s stabilizes at $(1.3 \pm 0.1)\,\text{MA m}^{-1}$ (which is in agreement with $1.4\,\text{MA m}^{-1}$ found in literature [20]) whereas K shows a decreasing trend. From the characterization of M_s, a dead layer of 0.24 nm is also found. K_s is determined in region 2 to be $(0.65 \pm 0.03)\,\text{mJ m}^{-2}$ but it is hard to tell how much the Ir/Co and Co/Pt surfaces contribute. Literature in which K_s is determined for Ir/Co/Pt stacks could not be found although it is known that it heavily depends on the substrates and buffer layers that have been used.

Finally, the DMI is determined with two different models but only the terminal domain width model is believed to result in reliable values for D. For the model by Draaisma and De Jonge, the magnetic system has to be at an energetic minimum which is hard to achieve when hysteresis is present in the system. The terminal domain width is believed to be less prone to this problem. D_terminal is lower than what is found in literature for low t_Co but for higher t_Co, it decreases and turns out to be much lower than what is found by others. One of the reasons for the disagreement between what is found here and literature could lie in A which is assumed from literature to be $10\,\text{pJ m}^{-1}$. However, this should be measured for the systems in order to give more reliable values for D (following, for example, the method as described by [54]). An increase in D_s in the characterized t_Co range is not found (like in K and M_s) is found. This is notable since D_s also results from the interfaces and therefore is expected to increase in the t_Co range of region 1. Using a more complex model in combination with demagnetizing the sample could result in different behavior for D_s.

No negative σ is determined from either of the models which means that the condition for skyrmion formation has not been met. Moreover, σ shows an increasing trend in the investigated region, ascribed to the increase in K being stronger than the increase in dipolar energy. In the next chapter it is discussed whether it is possible to lower σ with the help of Ga^+-irradiation and create skyrmions in our sample.

Chapter 6

Tuning DMI with Ga$^+$-irradiation

The DMI as a function of t_{Co} is characterized in the previous chapter. It was found that no negative σ is obtained in these structure so the next step is altering the atomic structure with Ga$^+$-irradiation. With Ga$^+$-irradiation, micrometer scale patterns can be irradiated which allows for subtle tuning of K and D by varying the Ga$^+$-dose [32, 33].

Based on the Ga$^+$-dose range that is used by Franken [32], D is characterized as a function of dose in the range of $(0.1 - 0.9) \times 1.6\mu C\,cm^{-2}$, and K in the range of $(0.1 - 1.1) \times 1.6\mu C\,cm^{-2}$, both in $0.1 \times 1.6\mu C\,cm^{-2}$ incremental steps. For this range of Ga$^+$-doses, it is investigated how K and D are influenced in an [Ir(1)/Co(0.6)/Pt]$_{\times 15}$ stack. K is determined from applying the Stoner-Wolfarth model to AHE-measurements (as explained in section 3.2.2) and will be discussed first. Next, it is characterized how σ is affected, which is determined from the terminal domain width model, after which the effect on D is calculated from equation 2.1.

6.1   Anisotropy as a function of Ga$^+$-dose

As mentioned in chapter 2, K is determined by fitting the Stoner-Wohlfarth model to AHE-measurements. An example of such an analysis is shown in figure 6.1. The OOP magnetization ($\frac{M_z}{M_s}$) of an unirradiated [Ir(1)/Co(0.6)/Pt]$_{\times 15}$ stack is measured as a function of an external magnetic field, indicated with the circles. The angle between the external field and the sample's normal (α) is varied which is indicated in the figure. In the figure, only a selection of various α is shown but for the actual fitting procedure, α is varied from 0° to 90° with incremental steps of 5°. In the 0° measurement, the external magnetic field is applied along the easy axis of the sample which results in M_z being fully saturated throughout this sweep. For increasing α, the M_z measured at large field decreases: the magnetization is pulled away from the easy axis which reduces the OOP component that is measured.

The data is fitted with the Stoner-Wohlfarth model, indicated with the solid lines. For the
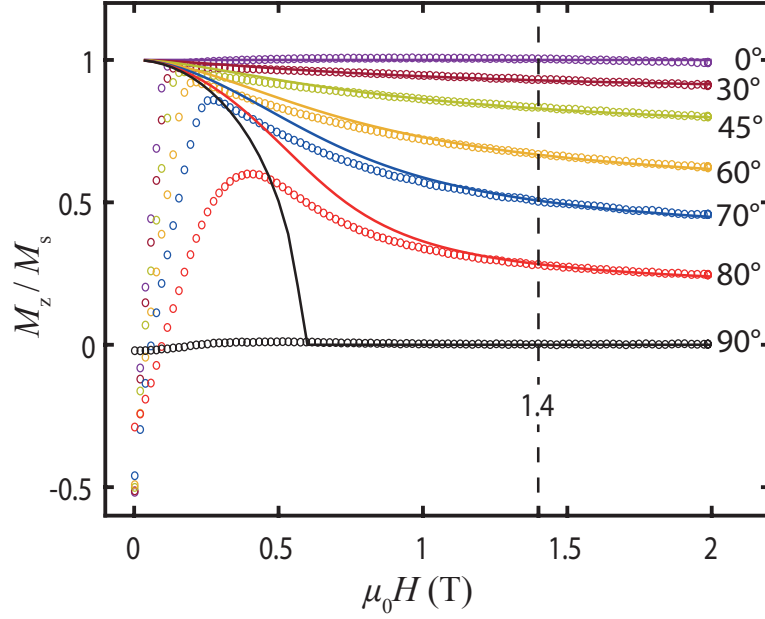

Figure 6.1: AHE measurements (indicated with the circles) of the OOP magnetization as function of an external magnetic field. The external magnetic field is under an angle with the sample's normal which is indicated in the figure. Only in the range of 1.4 T to 2 T, the magnetization shows coherent rotation. This region is therefore used to fit the data with the Stoner-Wohlfarth model (indicated with the solid lines).

region below 1.4 T, the Stoner-Wohlfarth model shows little correspondence to our data which is believed to result from the magnetization not rotating coherently, an assumption in the Stoner-Wohlfarth model. Coherent rotation means that the system is in a single domain as the direction of magnetization is changed. That this is not applicable to the samples used here can be seen in the MFM-measurements in figure 2.13: multiple domains are present as the magnetization reverses from negative to positive. This is schematically depicted in figure 6.2, which shows a cross-sectional view of a magnetic film in a multidomain state at zero field in A, and an allignment of all domains in B under the application of an external field. From figure 6.1 it is concluded that only at high fields (above 1.4 T), the system undergoes the required coherent rotation since the data matches the behavior predicted by the Stoner-Wohlfarth model which is why only the data in the range of 1.4 T to 2 T is used for the fit. With the fit, a K of $(0.33 \pm 0.03)\,\mathrm{MJ\,m^{-3}}$ is determined which agrees with K that is determined with the SQUID-VSM in chapter 5 ($K_{\mathrm{SQUID}} = (0.35 \pm 0.03)\,\mathrm{MJ\,m^{-3}}$), confirming that the right range in figure 6.1 is used for fitting. Note that for fitting the Stoner-Wohlfarth equation (2.15), the M_{s} with the MDL taken into account is used, so K determined here is also corrected for the MDL. The error in K results from M_{s} as determined in chapter 5.
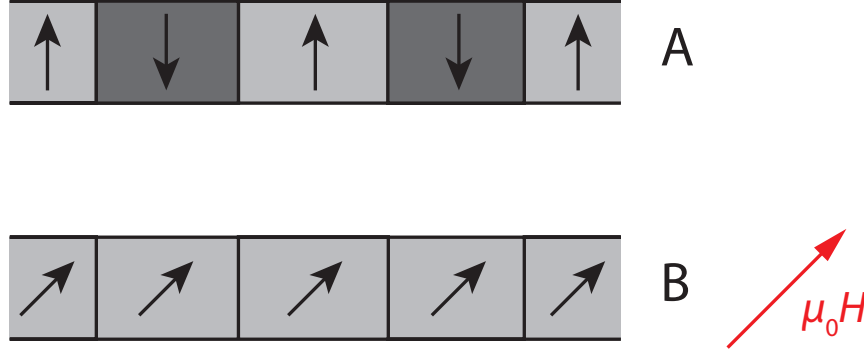
Figure 6.2: Cross-sectional view of a magnetic thin film. In situation A, no external field is applied and the magnetization is a in a multidomain state. In B, an external field is applied under an angle of 45°. The magnetization is in a coherent state in this situation.

As explained in section 3.2.2, Hall crosses are irradiated with doses ranging from 0 to $1.1 \times 1.6 \mu C\, cm^{-2}$, to characterize K as a function of Ga$^+$-dose which results in figure 6.3. A slight decrease in K is observed whereas a large decrease was expected since this was also found by others for these doses [32, 33]. At this dose however, and even above it, K remains positive and has only decreased slightly. Hyndman et al [33] found a transition from IP to OOP at a dose between 0.5 and $1 \times 1.6 \mu C\, cm^{-2}$ for a $Pt(2.8)/\left[Pt(0.6)/Co(0.3)\right]_{6\times}/Pt(6.5)$ system whereas our system's K only decreases slightly at this dose. By increasing the dose beyond this range it seems that the anisotropy eventually will drop significantly but, as is described in the next section, this is not an option for us.
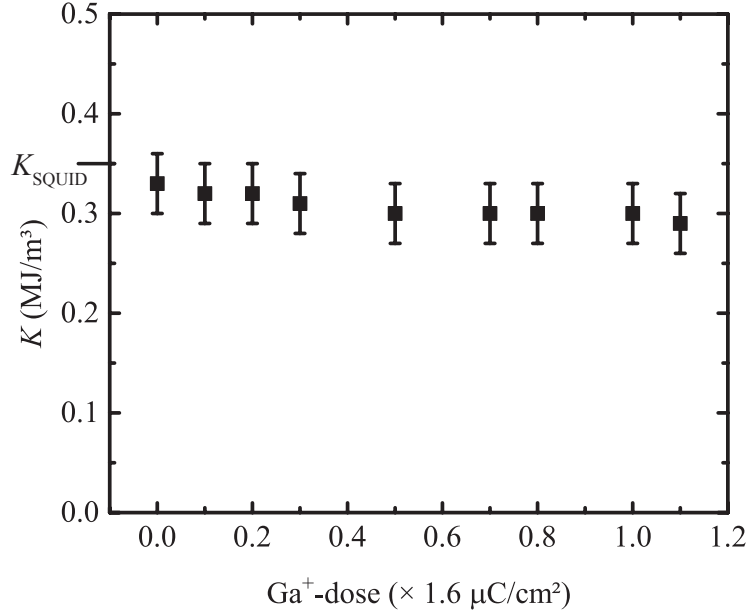
Figure 6.3: K determined from fitting the AHE measurements with the Stoner-Wohlfarth model as shown in figure 6.1, plotted as a function of Ga$^+$-dose for $[\mathrm{Ir}(1)/\mathrm{Co}(0.6)/\mathrm{Pt}(1)]_{15\times}$. K for a zero dose of Ga$^+$ extracted with the SQUID-VSM is indicated at $0.35\,\mathrm{MJ\,m}^{-3}$.

6.2   Domain wall energy as a function of Ga$^+$-dose

To characterize σ as a function of Ga$^+$-dose, 9 $10\,\mu\mathrm{m} \times 10\,\mu\mathrm{m}$ squares are irradiated on an $[\mathrm{Ir}(1)/\mathrm{Co}(0.6)/\mathrm{Pt}(1)]_{\times 15}$ sample with the dose in the range of $(0.1-0.9)\times 1.6\mu\mathrm{C\,cm}^{-2}$. The terminal domain width model is then applied to these areas as explained in section 5.3.2 (note that these areas are all irradiated on the same sample but that a different sample is used for characterizing K in the previous section). Magnetic contrast is observed with the MFM in this range except for the last dose strength. A scan of this area is shown in figure 6.4 where the irradiated area is inside the dashed lines. No magnetic contrast is visible anymore whereas outside the irradiated area it still is.

Scans as shown in figure 6.5 are obtained from irradiating and scanning the sample. In the vertical columns, scans of areas irradiated with doses of 0.1, 0.5 and $0.8 \times 1.6\mu\mathrm{C\,cm}^{-2}$ are shown. In the horizontal rows, scans are shown of the irradiated areas under the application of an external, OOP, magnetic field strength of $10\,\mathrm{mT}$, $37\,\mathrm{mT}$, $64\,\mathrm{mT}$ and $104\,\mathrm{mT}$.

Throughout these scans, no skyrmions are observed. In figures 6.5a to c, it can be seen that the domains get smaller as the dose increases. This is also observed in figures 6.5d to f and figures 6.5g to i. For the higher field strengths, however, it is measured that the width of the domains do not differ significantly anymore, just that the domain repetition width d differs. This leads to a terminal domain width, and thus a σ, that does not change as function of Ga$^+$-dose, which is plotted in figure 6.6. σ remains constant for all the Ga$^+$-
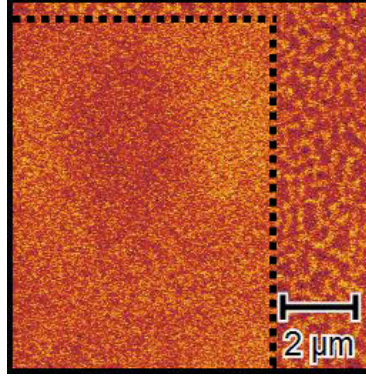
Figure 6.4: MFM image of an irradiated area (dose of $0.9 \times 1.6 \mu C \, cm^{-2}$) is shown inside the dashed lines where no magnetic contrast is visible. This is attributed to K being reduced in this area due to Ga$^+$-irradiation, making it an IP magnetized area.

doses around $1.8 \, mJ \, m^{-2}$. The error in σ mainly results from the error in the determined terminal domain width, which is done in the same way as described in section 5.3.2.

Both K and σ do not seem to change whereas figure 6.4 suggests that the anisotropy is changed suddenly to IP for doses $\geq 0.9 \times 1.6 \mu C \, cm^{-2}$, concluded from the absence of magnetic contrast. To explain what is happening, SRIM (Stopping and Range of Ions in Matter) Monte-Carlo simulations [58] are used to model the atomic structure of the multilayer during Ga$^+$-irradiation. In these simulations, an amorphous atomic lattice at zero Kelvin is assumed which is subsequently irradiated by a single Ga$^+$-ion. Each time an ion is accelerated towards the structure, the structure is considered to be undamaged, so how the system is altered due to previous Ga$^+$-ions is not taken into account. SRIM simulations are used to simulate the vacancies introduced by Ga$^+$ irradiation. A vacancy is introduced when an atom in the lattice is dislocated from its original site upon collision by a Ga$^+$-ion. It is possible for the dislocated atom to gain sufficient energy after collision with Ga$^+$ to create other vacancies, which is taken into account in the simulations. The vacancies created per Ga$^+$-ion are simulated since intermixing can only occur when atoms are dislocated from their original site, which is the origin of the anisotropy modification [31].

The simulation results in figure 6.7. Here, it is shown how many vacancies each incoming Ga$^+$-ion induces for every layer, determined from simulating the effect of 1000 ions. What can be seen is that most vacancies are created in the capping layer and the first four repeats in the multilayer. Repeats 5-9 gain less damage and the other layers are hardly affected. Intermixing will therefore mostly occur in the first four repeats. This explains why the reduction in K is low: determining K from the AHE is a bulk measurement and most of the repeats are hardly affected by Ga irradiation. For σ it is less intuitive to understand why it does not change. σ is determined with the MFM and the MFM measures the stray fields coming from the sample. These stray fields are a result of all 15 magnetic repeats in the sample. Apparently, the top 4 repeats do not change enough due to Ga$^+$-irradiation for the

$0.1 \times 1.6\mu C\,cm^{-2}$ $0.5 \times 1.6\mu C\,cm^{-2}$ $0.8 \times 1.6\mu C\,cm^{-2}$

$\mu_0 H = 10\,mT$

$\mu_0 H = 37\,mT$

$\mu_0 H = 64\,mT$

$\mu_0 H = 104\,mT$
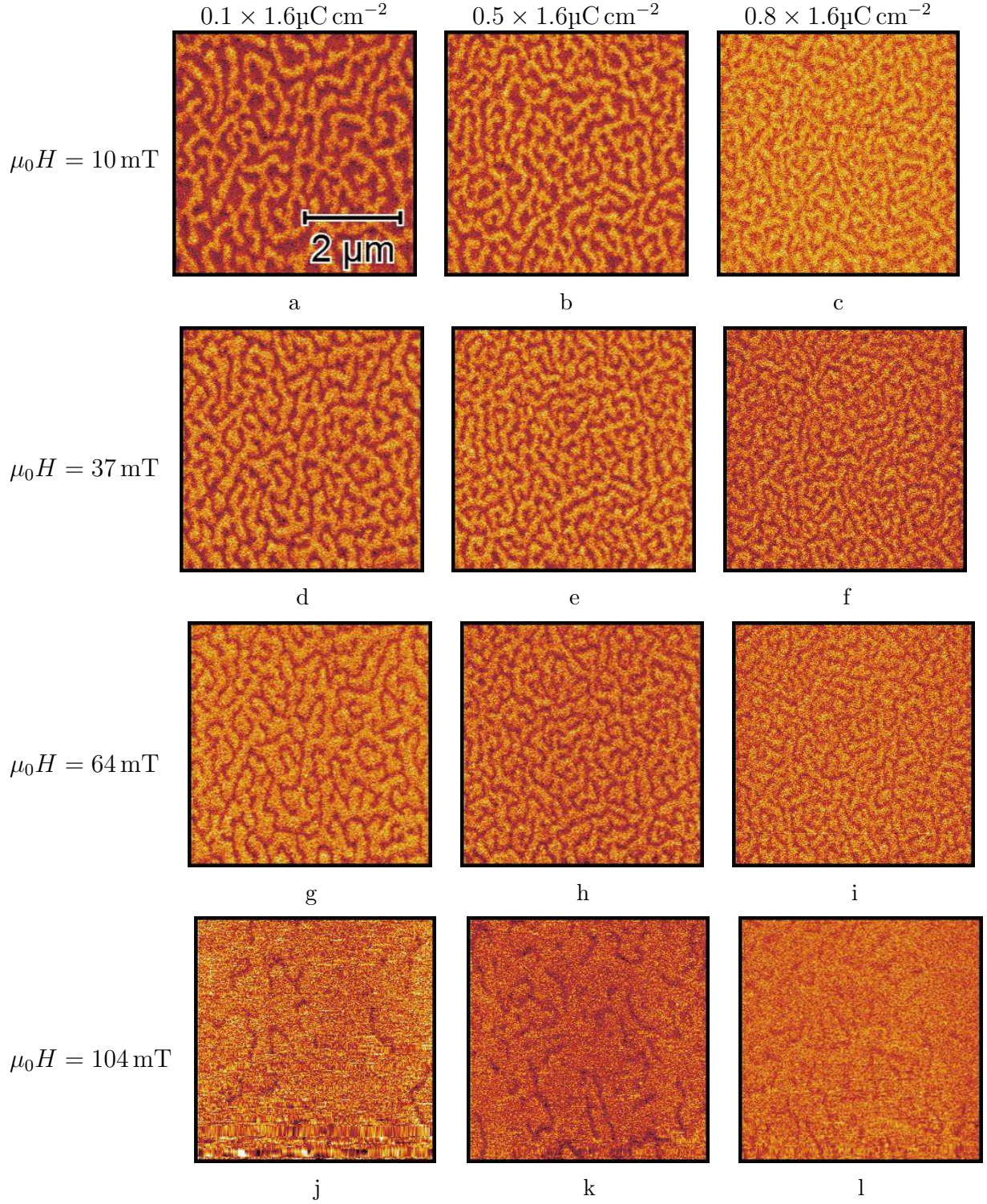
a   b   c

d   e   f

g   h   i

j   k   l

Figure 6.5: MFM scans of the irradiated areas in a $[Pt(1)/Co(0.6)/Ir(1)]_{15\times}$ sample. The vertical columns show scans irradiated with a dose of 0.1, 0.5 and $0.8\times\mu C\,cm^{-2}$ respectively. The horizontal rows show scans of the sample under the application of an external perpendicular field of $10\,mT$, $37\,mT$, $64\,mT$ and $104\,mT$.
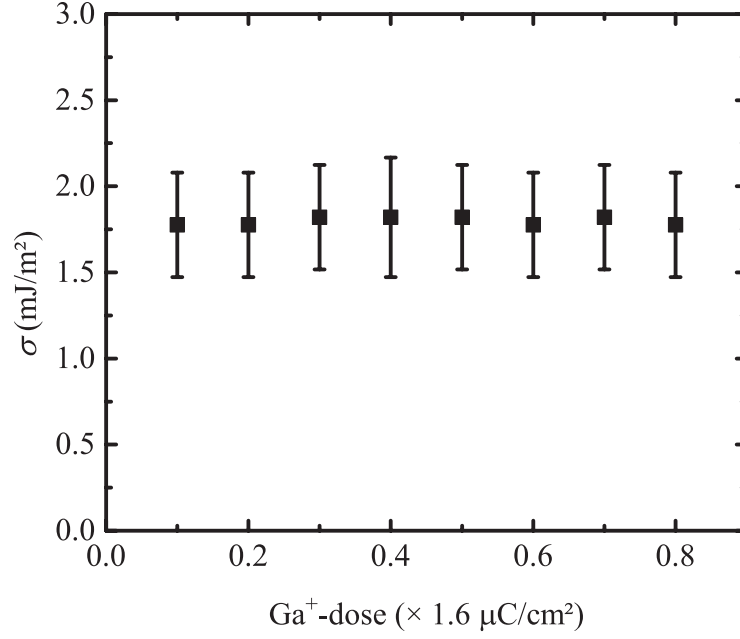
Figure 6.6: The domain wall energy plotted as a function of Ga$^+$-dose for [Ir(1)/Co(0.6)/Pt(1)]$_{15\times}$ determined from the terminal domain width model based on scans as shown in figure 6.5.

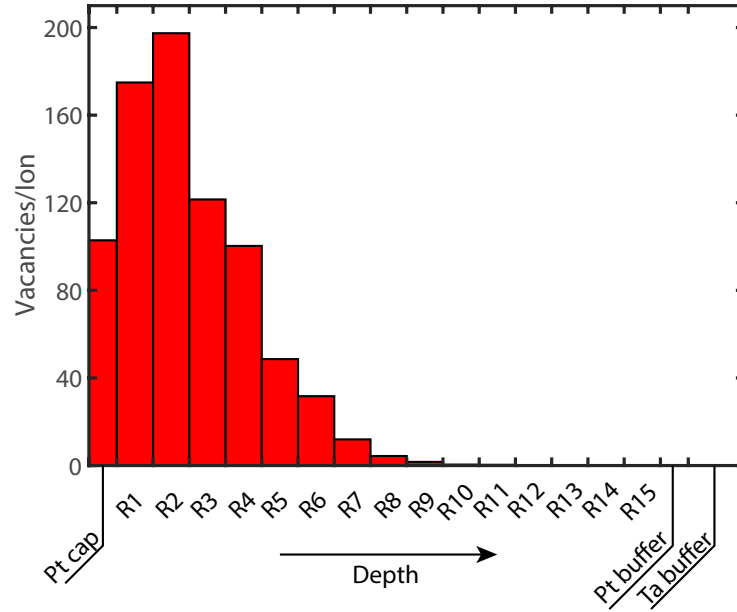Figure 6.7: Vacancies per Ga-ion induced in each of the layers of a [Ir(1)/Co(0.6)/Pt(1)]$_{15\times}$ sample, extracted from SRIM simulations. Pt cap, Pt buffer and Ta buffer indicate the capping and buffer layers. R indicates a repeat of Pt(1)/Co(0.6)/Ir(1) with Pt in the repeat the closest to the capping layer. R1 indicates repeat 1 which is counted starting from the top of the sample (so the closest to the cap).
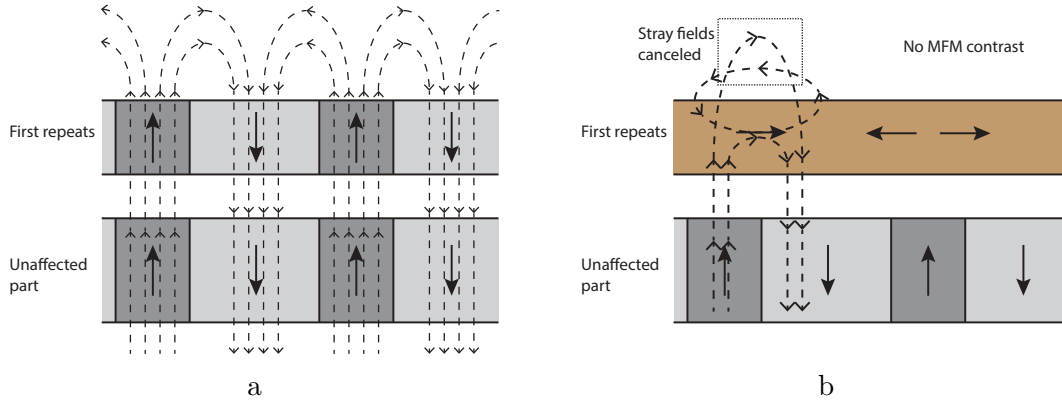
a   b

Figure 6.8: Both figures show the cross-section of the magnetic multilayer with both the top 4 and bottom 11 repeats combined to one. The unaffected part is thicker to indicate that more layers are unaffected than affected by Ga$^+$-irradiation. a: The anisotropy in the top repeats is lowered by Ga$^+$-irradiation but still remains OOP. Because of this, magnetic contrast is still visible in the MFM scans. b: The anisotropy in the top layers is lowered and is now IP. The stray fields coming from the unaffected part are canceled by the IP stray fields coming from the first repeats, leaving no MFM contrast above the sample.

MFM to measure a different $d_{\min}$ which then yields a different σ in this dose range. This is visualized in figure 6.8a. Here, the top layer is shown where the anisotropy is lowered due to Ga$^+$-irradiation. The domains in the top repeats still align with the domains in the lower, unaffected repeats so no change in domain width will be observed.

We suspect that by increasing the Ga$^+$-dose, K in the top layer decreases even further and an IP magnetization is introduced for doses $\geq 0.9 \times 1.6 \mathrm{\mu C\,cm}^{-2}$. It could therefore be possible that only the top 3 or 4 repeats are IP magnetized whereas the repeats below are not. The IP domains in the top repeats that form as a result of the lower repeats' stray fields are then located above the domain wall in the lower repeats. This could allow for the flux closure as shown in figure 6.8b. The stray fields above the sample, coming from the lower layers are canceled by the stray fields coming from the top (IP) layers resulting in an absence of stray fields above the sample. This would explain figure 6.4, where no magnetic contrast is observed because the MFM measures these stray fields. By irradiating with a dose of $0.9 \times 1.6 \mathrm{\mu C\,cm}^{-2}$, a transition of anisotropy in the top layers is introduced due to which magnetic contrast is gone. This remains speculation however, further investigation would be necessary to confirm this, e.g. by modelling this structure and the strength of the stray fields above the sample coming from the lower and upper repeats.

Finally, how D depends on Ga$^+$-irradiation dose is plotted in figure 6.9. As is expected from the little amount of change in K and σ, D remains relatively constant around $D =(1.7 \pm 0.2) \mathrm{mJ\,m}^{-2}$ over the full dose range. This D differs from what is found in chapter 5 ($D =(1.0 \pm 0.3) \mathrm{mJ\,m}^{-2}$) but agrees with what is found by Moureau-Luchaire et
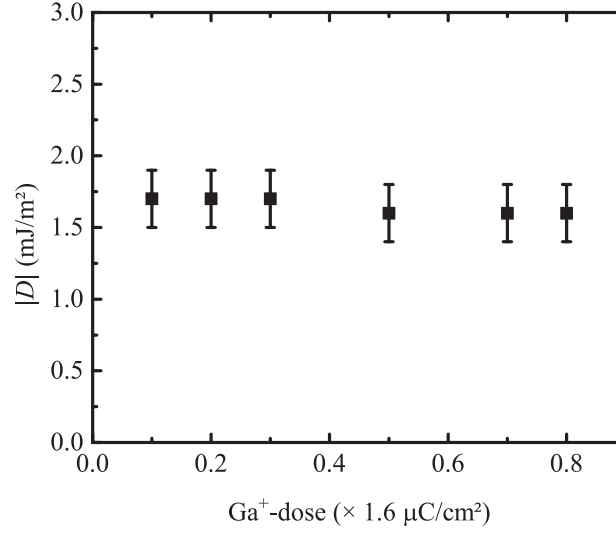
Figure 6.9: $|D|$ as a function of Ga$^+$-dose, determined with the terminal domain width model on a [Ir(1)/Co(0.6)/Pt(1)]$_{15\times}$ sample.

al. [26] ($D = (1.6 \pm 0.2)\,\mathrm{mJ\,m^{-2}}$). The disagreement between D found in the previous and this chapter could result from the fact that they are determined in different samples.

To summarize this chapter, we characterized how a [Ir(1)/Co(0.6)/Pt(1)]$_{\times 15}$ sample is affected by Ga$^+$-irradiation, specifically, the parameters K, σ and D.

How K and σ change is measured for a Ga$^+$ dose from $0.1 \times 1.6\mathrm{\mu C\,cm^{-2}}$ to $1.1 \times 1.6\mathrm{\mu C\,cm^{-2}}$ and $0.8 \times 1.6\mathrm{\mu C\,cm^{-2}}$ respectively. For both parameters, only a small reduction is observed which is unexpected. To explain the small effect, SRIM Monte Carlo simulations are used to model intermixing in the sample due to Ga$^+$-irradiation. It is found that intermixing mostly takes place in the top 4 repeats, leaving the others hardly, or not affected. This explains why the decrease in K and σ is so low.

Increasing the Ga$^+$-dose beyond $0.8 \times 1.6\mathrm{\mu C\,cm^{-2}}$ results in a loss of MFM signal which is attributed to IP domains in the upper 4 repeats cancelling the magnetic stray fields above the sample coming from the lower repeats. Since the effect of K and σ is small, it follows that D only decreases slightly as well. For future research, reducing the amount of repeats to 4 results in the full sample being affected by Ga$^+$-irradiation and thus a bigger effect on D.

Chapter 7

Conclusions and Outlook

In this thesis we investigated the behavior of parameters in [Ir/Co/Pt] multilayer systems which are important for stabilizing skyrmions at room temperature. We discussed the results of the investigation which includes: (1) the fabrication of our own MFM-tips, (2) the parameter's behavior as function of t_{Co} and (3) how the parameters change as a function of Ga^+-dose. The conclusions from these results are summarized here with an outlook for possibilities on further research. Next, a broader outlook is provided for long term research on the basis of obtained results during this project.

7.1 Concluding remarks and future research

Optimizing the magnetic force microscope Since commercially available MFM-tips perturbed the magnetic domain state of our sample it was necessary to produce tips ourselves. By sputtering a Ta/Co/Ta structure on commercially available AFM tips it is found that, for sufficiently thin Co, tips are obtained which only probe the magnetic domains and have a good signal-to-noise ratio. Quantitatively verifying that no domains are erased was not possible so inspection by eye remained necessary when we used our tips.

Characterizing the multilayers Next, t_{Co} is varied in our $[Ir(1)/Co(t_{Co})/Pt(1)]_{\times 15}$-samples and M_s, K and D are characterized. M_s and K are determined with the SQUID-VSM and for D, the MFM in combination with two domain spacing models is used.

For M_s and K we found that the characterized t_{Co} range can be divided in two regions: one in which the Co-interfaces are still under development and one in which they are fully developed. Both show an increasing trend in the first region as the interfaces develop after which, in the second region, M_s stabilizes and K shows a decreasing trend, attributed to the shape anisotropy. D is measured in the first region only and shows a decreasing trend. However, the expected increase in D_s is not found with either model. What is believed to influence the results is the models. For the model by Draaisma and De Jonge, negative $|D|$ are found which is unphysical and the terminal domain width model results in $|D|$ very

close to zero. For further research on determining D it is therefore recommended to apply a more elaborate model which takes domain wall interactions into account more precisely in combination with IP demagnetization of the samples.

Tuning multilayers with Ga$^+$-irradiation Lastly, an $[\mathrm{Ir}(1)/\mathrm{Co}(0.6)/\mathrm{Pt}(1)]_{\times 15}$ sample is irradiated with varying Ga$^+$-dose to induce intermixing at the interfaces in the multilayer. This is expected to alter K and D but we find only a slight decrease. Based on simulations we suspect that only the upper layers of the sample are affected by the irradiation, leaving the largest part unaffected. Although a small but gradual decrease is found in K, this is not observed in the MFM-scans. With the MFM it is observed that above a certain dose strength the magnetization suddenly turns IP, which is in disagreement with K for that dose since K remains positive. The loss of magnetic contrast is speculated to result from magnetic flux cancellation above the sample's surface, made possible by the upper Co-layers turning IP.

Since only the upper repeats seem affected by the Ga$^+$-irradiation, lowering the amount of layers is expected to result in intermixing throughout the whole sample. The effect on K and D is expected to be bigger in this situation.

7.2 Skyrmion nucleation sites in magnetic multilayer strips

During the characterization process, a notable MFM-scan was obtained after wrongly irradiating a lattice of spots with a stepsize of $\approx 1\,\mu\mathrm{m}$ between the spots instead of a full square. This scan is displayed in figure 7.1 and obtained after saturating the sample at large negative field and reducing it to $\mu_0 H = -37\,\mathrm{mT}$. What is believed to happen is that the anisotropy is lowered at the irradiated areas due to which domains can form there at field strengths whereas no domains are formed on the unirradiated areas. A possible application of locally lowering the anisotropy is to create skyrmion nucleation sites, as proposed by Buettner et al. [7] and Everschorr-Sitte et al. [59]. How this works is pictured in figure 7.2. A magnetic strip is modeled with a lowered anisotropy site of 150 nm in diameter, as shown in 7.2a. Applying a spin-orbit torque pulse allows for the nucleation of a skyrmion at this site of lowered anisotropy [7].

In 7.2b-g is displayed how the magnetization in the magnetic strip (blue: $m_{\mathrm{z}} > 0$, red: $m_{\mathrm{z}} < 0$) evolves as a function of time as spin-orbit torque pulses are applied. In figure 7.2h, the applied spin-orbit torque pulses are displayed as a function of time, with the letters indicating at which t the figures b-g are made. A high spin-orbit torque pulse is necessary to create a skyrmion (also the write pulse) and a lower spin-orbit torque pulse is used to move the skyrmions (also called the shift pulse). The logical state that is achieved is displayed in figure 7.2g with the presence of a skyrmion representing '1' and the absence
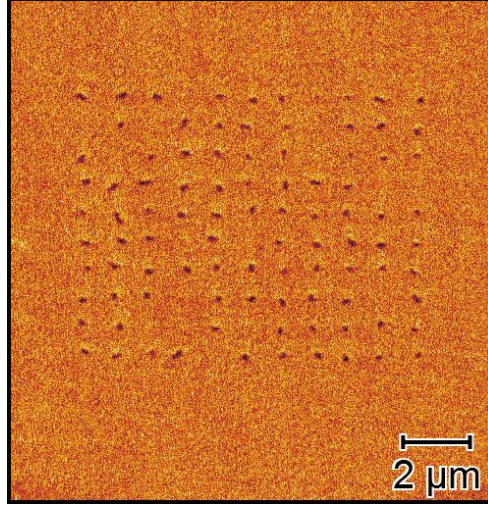
Figure 7.1: MFM-scan of an irradiated [Ir/Co(0.6)/Pt]$_{15x}$ sample at a field strength of $\mu_0 H = -37\,$mT after bringing the sample from saturation at large negative field. Instead of irradiating a square area, a square lattice of spots is irradiated with a stepsize of $\approx 1\,$µm. Domains can nucleate at these spots whereas no domains have formed in the unirradiated area yet.

a '0'.

Introducing such a site with a lowered anisotropy is possible with the help of Ga$^+$-irradiation as is shown in figure 7.1. For future research it could therefore be interesting to produce a magnetic multilayer strip and irradiate a site with Ga$^+$ to see if skyrmions are nucleated by applying current pulses.
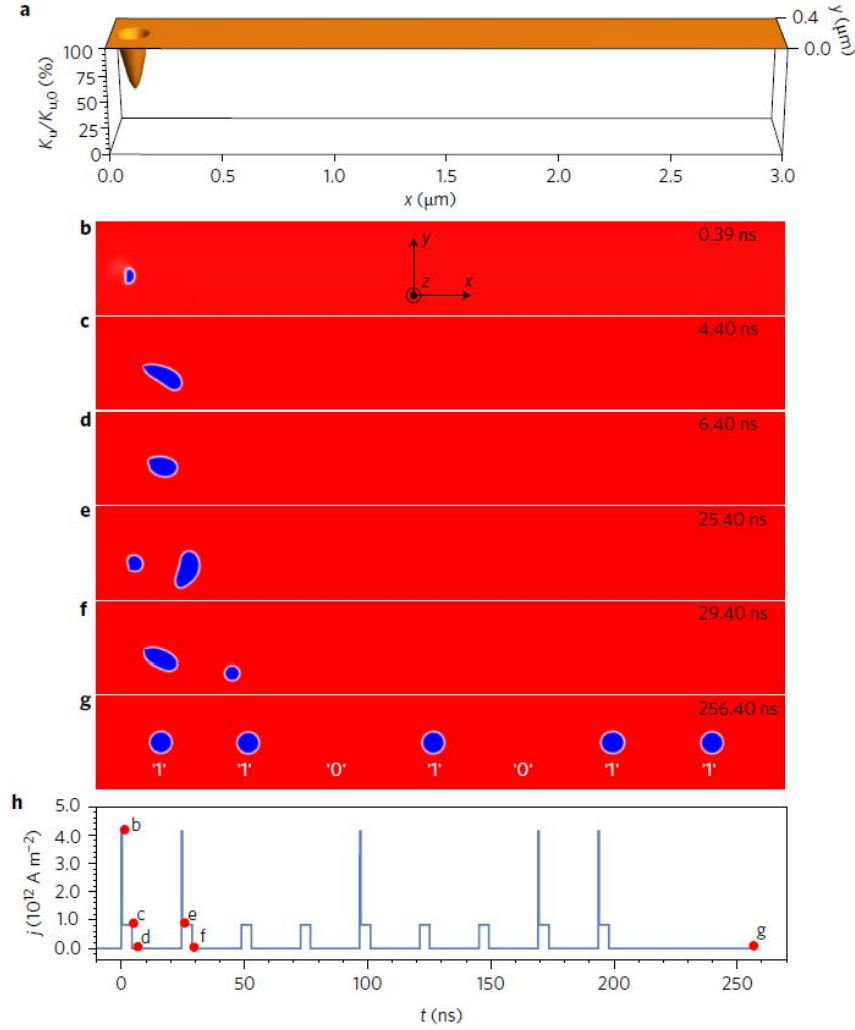
Figure 7.2: a: Anisotropy distribution in a $0.4\,\mu m \times 3\,\mu m$ magnetic strip. The area with lowered area has diameter of $150\,nm$. b-g: Formation of magnetic domains (blue: $m_z > 0$, red: $m_z < 0$) after application of current pulses along the positive x-direction. h: Current density through the strip in the positive x-direction as a function of time. The short, write pulses are $0.4\,ns$ long and the long, transport pulses $4\,ns$. In between the pulses, a relaxation time of $20\,ns$ is present. The time at which snapshots b-g are taken is also indicated. In g, the logical state of the systems is indicated with the presence of a skyrmion representing a '1' and the absence a '0'. Picture adapted from [7].

Bibliography

[1] T. Watson, "The floppy disk (1971-2010)," *Canadian Business*, vol. 83, p. 17, Summer 2010. Copyright - Copyright Rogers Publishing Limited Summer 2010; Document feature - Photographs; Last updated - 2017-11-17; CODEN - CABUDO. 1

[2] N. Macphail, "The evolution of the disc drive." `http://www.computerconservationsociety.org/resurrection/res55.htm`. Accessed: 2018-10-22. 2

[3] S. Ikeda, K. Miura, H. Yamamoto, K. Mizunuma, H. D. Gan, M. Endo, S. Kanai, J. Hayakawa, F. Matsukura, and H. Ohno, "A perpendicular-anisotropy CoFeB–MgO magnetic tunnel junction," *Nature Materials*, vol. 9, pp. 721–724, jul 2010. 3

[4] S. S. P. Parkin, M. Hayashi, and L. Thomas, "Magnetic domain-wall racetrack memory," *Science*, vol. 320, no. 5873, pp. 190–194, 2008. 3

[5] S.-H. Yang, K.-S. Ryu, and S. Parkin, "Domain-wall velocities of up to 750 m s-1 driven by exchange-coupling torque in synthetic antiferromagnets," *Nature Nanotechnology*, vol. 10, pp. 221–226, feb 2015. 3

[6] O. Boulle, J. Vogel, H. Yang, S. Pizzini, D. de Souza Chaves, A. Locatelli, T. O. Menteş, A. Sala, L. D. Buda-Prejbeanu, O. Klein, M. Belmeguenai, Y. Roussigné, A. Stashkevich, S. M. Chérif, L. Aballe, M. Foerster, M. Chshiev, S. Auffret, I. M. Miron, and G. Gaudin, "Room-temperature chiral magnetic skyrmions in ultrathin magnetic nanostructures," *Nature Nanotechnology*, vol. 11, pp. 449–454, jan 2016. 4

[7] F. Büttner, I. Lemesh, M. Schneider, B. Pfau, C. M. Günther, P. Hessing, J. Geilhufe, L. Caretta, D. Engel, B. Krüger, J. Viefhaus, S. Eisebitt, and G. S. D. Beach, "Field-free deterministic ultrafast creation of magnetic skyrmions by spin–orbit torques," *Nature Nanotechnology*, vol. 12, pp. 1040–1044, oct 2017. 4, 5, 19, 76, 78

[8] I. Kézsmárki, S. Bordács, P. Milde, E. Neuber, L. M. Eng, J. S. White, H. M. Rønnow, C. D. Dewhurst, M. Mochizuki, K. Yanai, H. Nakamura, D. Ehlers, V. Tsurkan, and A. Loidl, "Néel-type skyrmion lattice with confined orientation in the polar magnetic semiconductor GaV4s8," *Nature Materials*, vol. 14, pp. 1116–1122, sep 2015. 4, 8

[9] W. Legrand, D. Maccariello, N. Reyren, K. Garcia, C. Moutafis, C. Moreau-Luchaire, S. Collin, K. Bouzehouane, V. Cros, and A. Fert, "Room-temperature current-induced generation and motion of sub-100 nm skyrmions," *Nano Letters*, vol. 17, no. 4, pp. 2703–2712, 2017. PMID: 28358984. 4

[10] S. Woo, K. Litzius, B. Krüger, M.-Y. Im, L. Caretta, K. Richter, M. Mann, A. Krone, R. M. Reeve, M. Weigand, P. Agrawal, I. Lemesh, M.-A. Mawass, P. Fischer, M. Kläui, and G. S. D. Beach, "Observation of room-temperature magnetic skyrmions and their current-driven dynamics in ultrathin metallic ferromagnets," *Nature Materials*, vol. 15, pp. 501–506, feb 2016. 4, 56

[11] C. Song, C. Jin, J. Wang, H. Xia, J. Wang, and Q. Liu, "Skyrmion-based multi-channel racetrack," *Applied Physics Letters*, vol. 111, no. 19, p. 192413, 2017. 4

[12] S. Muhlbauer, B. Binz, F. Jonietz, C. Pfleiderer, A. Rosch, A. Neubauer, R. Georgii, and P. Boni, "Skyrmion lattice in a chiral magnet," *Science*, vol. 323, pp. 915–919, feb 2009. 4

[13] X. Z. Yu, Y. Onose, N. Kanazawa, J. H. Park, J. H. Han, Y. Matsui, N. Nagaosa, and Y. Tokura, "Real-space observation of a two-dimensional skyrmion crystal," *Nature*, vol. 465, pp. 901–904, jun 2010. 4, 14, 15

[14] W. Jiang, P. Upadhyaya, W. Zhang, G. Yu, M. B. Jungfleisch, F. Y. Fradin, J. E. Pearson, Y. Tserkovnyak, K. L. Wang, O. Heinonen, S. G. E. te Velthuis, and A. Hoffmann, "Blowing magnetic skyrmion bubbles," *Science*, vol. 349, pp. 283–286, jun 2015. 4

[15] A. Fert, N. Reyren, and V. Cros, "Magnetic skyrmions: advances in physics and potential applications," *Nature Reviews Materials*, vol. 2, p. 17031, jun 2017. 5

[16] A. Balk, K.-W. Kim, D. Pierce, M. Stiles, J. Unguris, and S. Stavis, "Simultaneous control of the dzyaloshinskii-moriya interaction and magnetic anisotropy in nanomagnetic trilayers," *Physical Review Letters*, vol. 119, aug 2017. 5, 31

[17] M. D. DeJong and K. L. Livesey, "Analytic theory for the switch from bloch to néel domain wall in nanowires with perpendicular anisotropy," *Phys. Rev. B*, vol. 92, p. 214420, Dec 2015. 8

[18] M. Heide, G. Bihlmayer, and S. Blügel, "Dzyaloshinskii-moriya interaction accounting for the orientation of magnetic domains in ultrathin films: Fe/w(110)," *Phys. Rev. B*, vol. 78, p. 140403, Oct 2008. 7

[19] H. Ibach and H. Lüth, *Solid-State Physics*. Springer Berlin Heidelberg, 2009. 9

[20] J. M. D. Coey, "Ferromagnetism and exchange," in *Magnetism and Magnetic Materials*, pp. 128–194, Cambridge University Press. 9, 10, 51, 64

[21] L. Néel, "Anisotropie magnétique superficielle et surstructures d'orientation," *Journal de Physique et le Radium*, vol. 15, no. 4, pp. 225–239, 1954. 10

[22] M. T. Johnson, P. J. H. Bloemen, F. J. A. den Broeder, and J. J. de Vries, "Magnetic anisotropy in metallic multilayers," *Reports on Progress in Physics*, vol. 59, pp. 1409–1458, nov 1996. 10, 27, 56

[23] T. H. Johansen, A. V. Pan, and Y. M. Galperin, "Exact asymptotic behavior of magnetic stripe domain arrays," *Phys. Rev. B*, vol. 87, p. 060402, Feb 2013. 10, 17, 19, 20, 26

[24] J. D. Jackson, *Classical Electrodynamics, 2nd Edition*. Wiley, 1975. 10

[25] A. Fert and P. M. Levy, "Role of anisotropic exchange interactions in determining the properties of spin-glasses," *Physical Review Letters*, vol. 44, pp. 1538–1541, jun 1980. 12, 13

[26] C. Moreau-Luchaire, C. Moutafis, N. Reyren, J. Sampaio, C. A. F. Vaz, N. V. Horne, K. Bouzehouane, K. Garcia, C. Deranlot, P. Warnicke, P. Wohlhüter, J.-M. George, M. Weigand, J. Raabe, V. Cros, and A. Fert, "Additive interfacial chiral interaction in multilayers for stabilization of small individual skyrmions at room temperature," *Nature Nanotechnology*, vol. 11, pp. 444–448, jan 2016. 12, 61, 62, 73

[27] A. Fert, V. Cros, and J. Sampaio, "Skyrmions on the track," *Nature Nanotechnology*, vol. 8, pp. 152–156, mar 2013. 13

[28] G. Chen, T. Ma, A. T. N'Diaye, H. Kwon, C. Won, Y. Wu, and A. K. Schmid, "Tailoring the chirality of magnetic domain walls by interface engineering," *Nature Communications*, vol. 4, oct 2013. 14

[29] H. J. G. Draaisma and W. J. M. de Jonge, "Magnetization curves of pd/co multilayers with perpendicular anisotropy," *Journal of Applied Physics*, vol. 62, pp. 3318–3322, oct 1987. 17, 26

[30] Schippers, "Measuring a peak shift in propagating spin-wave spectroscopy," 2018. 28

[31] C. A. Volkert and A. M. Minor, "Focused ion beam microscopy and micromachining," *MRS Bulletin*, vol. 32, pp. 389–399, may 2007. 28, 30, 69

[32] J. Franken, *Domain walls shift gears*. PhD thesis, Eindhoven University of Technology, 2014. 29, 31, 65, 67

[33] R. Hyndman, P. Warin, J. Gierak, J. Ferré, J. N. Chapman, J. P. Jamet, V. Mathet, and C. Chappert, "Modification of co/pt multilayers by gallium irradiation—part 1: The effect on structural and magnetic properties," *Journal of Applied Physics*, vol. 90, pp. 3843–3849, oct 2001. 29, 65, 67

[34] N. A. Sinitsyn, "Semiclassical theories of the anomalous hall effect," *Journal of Physics: Condensed Matter*, vol. 20, p. 023201, dec 2007. 32

[35] O. Hellwig, A. Berger, J. B. Kortright, and E. E. Fullerton, "Domain structure and magnetization reversal of antiferromagnetically coupled perpendicular anisotropy films," *Journal of Magnetism and Magnetic Materials*, vol. 319, pp. 13–55, dec 2007. 35

[36] B. de Loos, "Magnetic Force Microscopy: application to magnetic nanostructures," Master's thesis, Eindhoven University of Technology, the Netherlands, 2006. 36, 38, 39, 85

[37] R. Howland and L. Benatar, *A Practical Guide: To Scanning Probe Microscopy.* Park scientific instruments, 1996. 37

[38] Ó. Iglesias-Freire, M. Jaafar, E. Berganza, and A. Asenjo, "Customized MFM probes with high lateral resolution," *Beilstein Journal of Nanotechnology*, vol. 7, pp. 1068–1074, jul 2016. 43, 87

[39] T. Lin, H. Liu, S. Poellath, Y. Zhang, B. Ji, N. Lei, J. J. Yun, L. Xi, D. Z. Yang, T. Xing, Z. L. Wang, L. Sun, Y. Z. Wu, L. F. Yin, W. B. Wang, J. Shen, J. Zweck, C. H. Back, Y. G. Zhang, and W. S. Zhao, "Observation of room-temperature magnetic skyrmions in pt/co/w structures with a large spin-orbit coupling," *Phys. Rev. B*, vol. 98, p. 174425, Nov 2018. 48

[40] S. Zhang, J. Zhang, Q. Zhang, C. Barton, V. Neu, Y. Zhao, Z. Hou, Y. Wen, C. Gong, O. Kazakova, W. Wang, Y. Peng, D. A. Garanin, E. M. Chudnovsky, and X. Zhang, "Direct writing of room temperature and zero field skyrmion lattices by a scanning local magnetic field," *Applied Physics Letters*, vol. 112, p. 132405, mar 2018. 48

[41] R. Masapogu, A. Yagil, A. Soumyanarayanan, A. K.C. Tan, A. Almoalem, O. Auslaender, and C. Panagopoulos, "Evolution of chiral magnetic textures and their topological hall signature in ir/fe/co/pt multilayer films," 08 2017. 48

[42] J. Curiale, M. Granada, H. E. Troiani, R. D. Sánchez, A. G. Leyva, P. Levy, and K. Samwer, "Magnetic dead layer in ferromagnetic manganite nanoparticles," *Applied Physics Letters*, vol. 95, p. 043106, jul 2009. 49

[43] *Accuracy of the Reported Moment: Sample Shape Effects.* 50

[44] S. Bandiera, R. R. Sousa, B. B. Rodmacq, and B. Dieny, "Asymmetric interfacial perpendicular magnetic anisotropy in pt/co/pt trilayers," *IEEE Magnetics Letters*, vol. 2, pp. 3000504–3000504, 2011. 50, 51

[45] Rutten, "Asymmetric propagation of surface spin waves in co/pt multilayers," 2017. 50

[46] M. S. Gabor, T. P. Jr, R. B. Mos, M. Nasui, C. Tiusan, and T. Petrisor, "Interlayer exchange coupling in perpendicularly magnetized pt/co/ir/co/pt structures," *Journal of Physics D: Applied Physics*, vol. 50, no. 46, p. 465004, 2017. 50, 51, 52, 55

[47] N.-H. Kim, J. Jung, J. Cho, D.-S. Han, Y. Yin, J.-S. Kim, H. J. M. Swagten, and C.-Y. You, "Interfacial dzyaloshinskii-moriya interaction, surface anisotropy energy, and spin pumping at spin orbit coupled ir/co interface," *Applied Physics Letters*, vol. 108, p. 142406, apr 2016. 51, 55

[48] K.-S. Ryu, S.-H. Yang, L. Thomas, and S. S. P. Parkin, "Chiral spin torque arising from proximity-induced magnetization," *Nature Communications*, vol. 5, may 2014. 51

[49] F. den Broeder, W. Hoving, and P. Bloemen, "Magnetic anisotropy of multilayers," *Journal of Magnetism and Magnetic Materials*, vol. 93, pp. 562 – 570, 1991. 54, 55

[50] Y. Huai, H. Gan, Z. Wang, P. Xu, X. Hao, B. K. Yen, R. Malmhall, N. Pakala, C. Wang, J. Zhang, Y. Zhou, D. Jung, K. Satoh, R. Wang, L. Xue, and M. Pakala, "High performance perpendicular magnetic tunnel junction with co/ir interfacial anisotropy for embedded and standalone STT-MRAM applications," *Applied Physics Letters*, vol. 112, p. 092402, feb 2018. 54

[51] J. Cho, N.-H. Kim, S. Lee, J.-S. Kim, R. Lavrijsen, A. Solignac, Y. Yin, D.-S. Han, N. J. J. van Hoof, H. J. M. Swagten, B. Koopmans, and C.-Y. You, "Thickness dependence of the interfacial dzyaloshinskii–moriya interaction in inversion symmetry broken systems," *Nature Communications*, vol. 6, jul 2015. 55

[52] N.-H. Kim, D.-S. Han, J. Jung, J. Cho, J.-S. Kim, H. J. M. Swagten, and C.-Y. You, "Improvement of the interfacial dzyaloshinskii-moriya interaction by introducing a ta buffer layer," *Applied Physics Letters*, vol. 107, p. 142408, oct 2015. 55

[53] G. Winkler, A. Kobs, A. Chuvilin, D. Lott, A. Schreyer, and H. P. Oepen, "On the variation of magnetic anisotropy in co/pt(111) on silicon oxide," *Journal of Applied Physics*, vol. 117, p. 105306, mar 2015. 56

[54] C. Eyrich, A. Zamani, W. Huttema, M. Arora, D. Harrison, F. Rashidi, D. Broun, B. Heinrich, O. Mryasov, M. Ahlberg, O. Karis, P. E. Jönsson, M. From, X. Zhu, and E. Girt, "Effects of substitution on the exchange stiffness and magnetization of co films," *Physical Review B*, vol. 90, dec 2014. 56, 61, 64

[55] J. Lucassen, F. Kloodt-Twesten, R. Frömter, H. P. Oepen, R. A. Duine, H. J. M. Swagten, B. Koopmans, and R. Lavrijsen, "Scanning electron microscopy with polarization analysis for multilayered chiral spin textures," *Applied Physics Letters*, vol. 111, p. 132403, sep 2017. 61

[56] W. Legrand, J.-Y. Chauleau, D. Maccariello, N. Reyren, S. Collin, K. Bouzehouane, N. Jaouen, V. Cros, and A. Fert, "Hybrid chiral domain walls and skyrmions in magnetic multilayers," *Science Advances*, vol. 4, p. eaat0415, jul 2018. 62, 63

[57] F. Büttner, I. Lemesh, and G. S. D. Beach, "Theory of isolated magnetic skyrmions: From fundamentals to room temperature applications," *Scientific Reports*, vol. 8, mar 2018. 64

[58] J. Biersack and L. Haggmark, "A monte carlo computer program for the transport of energetic ions in amorphous targets," *Nuclear Instruments and Methods*, vol. 174, pp. 257–269, aug 1980. 69

[59] K. Everschor-Sitte, M. Sitte, T. Valet, A. Abanov, and J. Sinova, "Skyrmion production on demand by homogeneous DC currents," *New Journal of Physics*, vol. 19, p. 092001, sep 2017. 76

Appendix A

Observed effects during MFM-tip production

During producing of the MFM-tips some interesting phenomena are observed. The first of these explains why there are no data points in figure 4.6 in the range of 10 mT to 35 mT for the 10 nm tip and 10 mT to 60 mT for the 20 nm tip. Just like in the magnetic samples, the magnetization of the tip can switch too and this is not necessarily an abrupt switch. The magnetization of the tip that is in a single or multi domain state is pictured in figures A.1a and A.1b respectively together with an MFM-scan that is made with a tip that is believed to be in a multi domain state in figure A.1c. The applied magnetic field is antiparallel to tip's magnetization which causes this multidomain state. Increasing the field further eventually results in a fully magnetized tip.

In figure 4.6, data points are not present in a certain field range because the tip was in a multi domain state here. The field at which this happens is not unambiguous and is believed to depend on the shape of the tip. At these Co thicknesses the dipolar energy, or the shape anisotropy, is the largest contributor to the total magnetization of the tips. The electron microscope image in figure 4.3a shows a pyramid shaped tip with two sides that are coated during the sputter process. Different switching fields are believed to be a result of these two sides that are different for each tip.

Another effect that was observed when using the tips is that the scan quality reduces while it is being used. An example of such a scan is shown in figure A.2. The signal-to-noise ratio slowly becomes worse as the scan progresses and eventually the tip is not usable anymore. The scans made after this show no magnetic contrast.

Loss of the signal is attributed to a capillary layer on the surface of the sample [36]. This layer of water is believed to cause deterioration of the signal by oxidizing the Co-layer on the tip. It seemed that this effect was worse under humid conditions, which could result in more water on the sample's surface. The tips could be used longer if a capping layer of Ta(4) was applied which is attributed to the capping layer protecting the Co. It is not
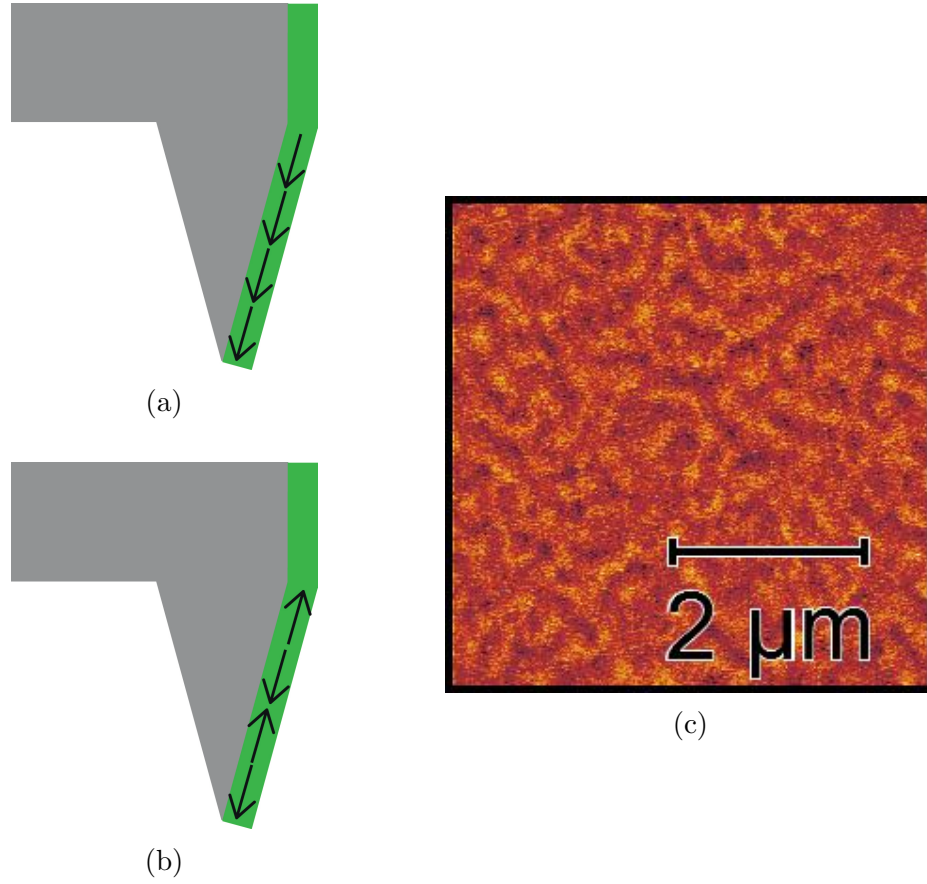
Figure A.1: Figure a and b show schematics of the Co-coated (green) tips being either in the single (a) or in a multi (b) domain state. Figure c shows the result of scanning the sample with a tip that is in a multi domain state.
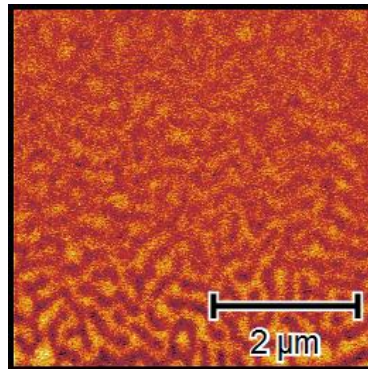

Figure A.2: MFM-scan made with a tip that slowly loses its signal as it progresses from down to up. A capping layer is used to prevent this from happening.

known how long the tips with capping could last before being oxidized since they would break much sooner due to wear.

Depositing a capping layer of Ta not only resulted in longer usability of the tip, it also results in less Co that is needed to gain the right signal-to-noise ration. When no capping layer is applied, the top ≈ 2 nm of Co will oxidize [38] which will then serve as a capping layer. Depositing a capping layer of Ta(4) resulted in only 7.5 nm of Co being necessary to produce workable tips. The final MFM tips were obtained by coating AFM tips with Ta(2)/Co(7.5)/Ta(4).